Doctoral Dissertation

STUDY OF DEFECT INSPECTION SYSTEM FOR CONCRETE TUNNEL LINING BASED ON IMAGE PROCESSING TECHNIQUES

(画像処理技術 に基づくトンネル覆工コンクリートの 外観検査システムの研究)

NGUYEN KIM CUONG

Division of Environmental Science and engineering

Graduate School of Science and Engineering

Yamaguchi University

Yamaguchi, Japan

ABSTRACT

The number of deteriorated concrete infrastructures has increased dramatically in many countries due to rapid aging. Therefore, the maintenance and management of existing concrete structures have become a major social concern worldwide. Concrete defects are important indicators reflecting the safety of infrastructure. To keep concrete components at good condition under all circumstances, the inspection plays an important role in the maintenance of infrastructure. Defect detection on concrete tunnel lining surface is one of the basic tasks of the inspection. One of the most frequently adopted inspection techniques is visual inspection, which is carried out by inspectors. It has a number of limitations, such as the high labour costs associated with carrying out tasks, and inaccuracy due to subjectivity, slow inspection speed and disruption to traffic.

A large number of researches have been considered to develop automated inspection systems to improve on manual visual inspection. In the field of civil engineering, a number of inspection systems have been developed to utilise inexpensive technologies based on digital videos and cameras. Examples of these systems include crack detection method such as Yamaguchi and Hashimoto 2006, Miyamoto et al 2007, and systems to allow the fast acquisition of video data Ukai et al 2000, Yu et al 2007. However, none of these systems offer complete solutions and a significant amount of work is still required to create an automatic inspection system that can be adopted by the industry. The advantage of image processing techniques offers the possibility of creating an automatic inspection system. This thesis describes a system, which is based on state-of-the-art image processing techniques, to aid the visual inspection of tunnel lining. The system uses multi standard digital cameras mounted on a steel framework which is capable of sliding from side to top of the inspecting vehicle to shoot the full surface of the tunnel lining. The device is cheap compared to other technologies, such as MIMM-R or infrared cameras.

This research proposes an image acquisition system with a simple and effective structure that obtains sufficient image data for objective and precise quantification.

Furthermore, image stitching software was developed to create a full view of the tunnel wall surface image automatically.

The first contribution of the inspection system in this research is to create the extended panoramic images in both longitudinal and circumferential directions to assist inspectors who have a wider field of view or an enhanced visualisation of large area the tunnel lining. To achieve this, a mosaicing technique consisted of image matching and stitching methods is proposed. In that, image matching method is detail presented in similarity and curvature metrics to find correct matching points. Moreover, a global and local correction method is presented that adjusts image matching error in the automatic image stitching according to the tunnel longitudinal direction. Moreover, in the curvature metric, median filter is used for refinement to smooth image motion quantity (*IMQ*) in the consecutive image stitching process.

Accordingly, an image stitching software is developed based on the proposed algorithm to create a layout panorama of the tunnel lining surface for assisting defect inspection. Moreover, experimental results for an actual tunnel demonstrate that the curvature measurement can match consecutive images accurately.

The second contribution of the inspection system is to present a prototype software based on image processing technique and an interactive genetic algorithm (iGA) with touch screen helps inspector easily detect the cracks (defects) from various concrete surface images.

The algorithm for accurate crack detection has composed of three major process parts. The first part was image input part which included image input and grayscale image transformation. The second part was crack enhancement part which included the following pre-processing steps: median filter, subtraction, binarization. The final part was noise removal part, comprising two steps: labeling and linear degree determination. Moreover, the optimized parameters are adjusted by iGA. Namely, the size of median filter is expressed by 6 bits, the binarization is expressed by 8 bits and the linear degree is expressed by 6 bits. Three parameters are combined to create a represented chromosome for solution candidates in a population.

Furthermore, to improve the capacity of the thin crack detection in the various complex environmental conditions, an image processing technique based on mathematic morphology is also proposed, which consists of morphological filter, binarization,

dilation-erosion transformation, labelling and linear degree. The optimum parameters of IPT are also adjusted by genetic algorithm.

The crack detection results of the proposed method are compared to the ones of other methods to demonstrate that the proposed method has possibility of extracting crack with reasonable accuracy and working time.

TABLE OF CONTENT

LIST OF TABLES

LIST OF FIGURES

LIST OF SYMBOLS AND ABBREVIATIONS

SYMBOLS	MEANING
(k,l)	The coordinates of search point
S_1	the estimated change in position
x	the speed (m/s) of the inspection car
y	frame rate (fs).
z	imaging resolution
m_i	the i^{th} *IMQ* before the correction
M_i	the i^{th} *IMQ* after the correction of Step 1
ε	the *IMQ* threshold value corresponding to an inspection car speed of 5 km/h (T_1= 100 pixel)
α	parameter of the speed variance
V1-V6	Six cameras of the image acquisition device
R1-R6	Scanning six regions of the image acquisition device
σ_i	score deviation value
S_i	Score for a measurement of similarity as well as curvature
S_{avg}, S_{max}, and S_{min}	Average, maximum, and minimum scores of the metrics

ABBREVIATIONS

CNP	*Curvature of cost curve at the nearest pixels as well as the pixel being processed*
GA	Genetic algorithm
iGA	Interactive genetic algorithm
IMQ	*Image motion quantity*
*IMQ*x	*Image motion quantity via the longitudinal direction (X-Axis)*
*IMQ*y	*Image motion quantity via the circumferential direction (Y-Axis)*
IML	*Image matching location*
IPT	*Image processing technique*
MSM	*Maximum value of the Similarity Measurement*
NCC	*Normal-cross correlation*
POI	*Point of interest*
SAD	*Sum absolute difference*
SSD	*Sum standard difference*
ZNCC	*Zero-mean Normal-cross correlation*
WTA	*Winner-take-all*

CUR(SAD), *CUR(SSD*), *CUR(NCC*), and *CUR(ZNCC)* Curvature metric using matching cost function *SAD*, *SSD*, *NCC*, and *ZNCC*, respectively

CHAPTER 1

INTRODUCTION

1.1 BACKGROUND

The main aim of this research is to provide an effective inspection system of the tunnel lining based on the simple image-acquisition equipment and image processing technique. The results presented in this thesis assist inspectors in two areas of the inspecting works: (1) A layout panorama production enlarges field of view of the full tunnel lining surface. (2) A semi-automatic crack detection method for inspecting regions which are not able to detect crack automatically. This method is relied on image processing techniques (IPTs) and interactive genetic algorithm based. (3) A fully automatic crack detection method for the inspecting regions where crack pixels are easily detected by IPTs and genetic algorithm. This introductory chapter provides a background to the problems related to the current field and motivation for this study. A brief overview and the contributions of the proposed system are presented. The structure of the rest of the thesis is outlined at the end of the chapter.

Civil infrastructure has large-size components which limited field of view of human eye is not able to contact at close distance. Therefore, image processing techniques has become a powerful tool for infrastructure inspection and evaluation with wide applications. For example, the light illumination of the tunnel will result in distractive image background which will influence the tunnel lining crack assessment. The limitations of infrastructure environment are considered in image process and analysis technologies.

Following road statistic annual report 2017, in Japan there are 10,102 tunnels. Whereas the over 50-year existing tunnels have about 2000 tunnels in 2015 with

proportion 20%, and ten years later, in 2025, this proportion is 34% with respect to 3,000 the over 50-year tunnels. Most underground infrastructure was constructed more than half a century ago and is now deteriorating Stajano et al[1].

However, periodic work of inspection in the local government is every 5 years for one time. If abnormalities or defects in these structures (cracks, leakage, spalling, cavity, etc) are not addressed as soon as possible for maintenance, repair, and rehabilitation, they easily deteriorate and are prone to damage or influence to safety human and prosperities. For example, Asakura et al[2] On June 27, 1999, an electric power failure occurred inside the Fukuoka Tunnel along the Sanyo Shinkansen line and the Hikari train came to a stop. The investigation indicated that a pantograph of the 12th car was broken.

Moreover, On November 28, 1999, a freight train in the Rebunhama Tunnel of the Muroran Main line spotted something unusual on the tracks and applied the emergency brake. It was too late to avoid the object, however, and the train hit it and derailed. From the investigation, it was found that five pieces of concrete blocks, as large as several tens of centimeters, lay on the track and that those blocks had fallen from the tunnel arch. Therefore, effective maintenance strategies are urgently required in order to an age underground infrastructure properly to assure public safety while at the same time meeting usage demands Chaiyasarn et al[3].

Furthermore, conventional inspection approaches are often subjective and time-consuming and expensive because these methods require many inspectors, labor and traffic limitation. Especially, human visual inspection has to stand on the trolley and rolling devices in order to inspection work which are unsafe for the inspectors Burgess & Niple 2005[4]; Elliott and Heymsfield[5]. In addition, some of non-destructive methods applied to detail inspection such as impact acoustics, infrared thermograph, test hammers, CT, and X-ray still remain a number of limitations. For example, these methods need expert knowledge to analysis obtained data.

Fig.1.1 Image acquicsition system using MIMM-R[6].

The photographic images provide the rich information from the tunnel lining surface such as textures, colours and 3D clues. Furthermore, development of image sensors with low-cost but has high capability of storage devices. Application computer vision helps inspectors can inspect off-line civil infrastructure surface condition directly and guarantee of the accuracy, objective and inexpensive cost. Crack inspection is fundamental task of the tunnel lining surface. Inspectors need to know different characteristic features of cracks such as locations, quantity, orientation, widths, lengths, and depths.

To improve the efficiency of the tunnel inspection system, in the past decade, many researchers have developed various sensors and image processing technology. Development of travelling measurement system scans continuously the tunnel lining surface using an exclusive vehicle for the purpose is to increase the high accuracy. For example of practical application, as shown in **Fig.1.1**, MIMM-R[6] (mobile imaging system and mobile mapping system) dedicated to tunnel measurement that a measurement inspection company developed. MIMM-R is capable of detecting the cracks of 0.3 mm in width from the photographed images while running at 70 Km/h. besides, MIMM-R can measure the deformations of the tunnel such as: water leakage, deterioration of material and create defect map and saving labors in sketching work. MIMM-R can measure the deformations of the tunnel such as: water leakage, deterioration of material and create defect map and saving labors in sketching work.

In addition, MIMM-R can analyze cross-section of the tunnel. It is also possible to grasp the insufficient thickness of rear cavity parts by a laser. And also conduct detailed investigation of the tunnel at the same time of the inspection. Therefore, it is high to

improve the efficiency of the tunnel inspection. However, the inspection system of MIMM-R requires an exclusive vehicle, and the inspection cost is high (the measurement cost per meter of distance is 600 to 1,500 thousand yen).

For this reason, road tunnel networks which a local government manages are difficult to carry out a detailed investigation or diagnosis using the high-cost measuring inspection system as MIMM-R, due to the limitation of maintenance budget in the present condition. Further, the ministry of land, infrastructure, transport and tourism's "Routine Tunnel Periodic Inspection Procedure" in Japan reports that cracks judged to be dangerous in maintaining and managing tunnels are "widths greater than 3.0 mm". In other words, MIMM-R can detect the minimum crack width in term of high performance which inspecting-cost is high for local governments with small maintenance budget.

It is necessary to develop a simple inspection device stead of MIMM-R and inspecting price reduction so that the local government enable the introduction of the travelling continuous image scanning system combined image processing technique.

1.2 RESEARCH OBJECTIVES

The objective of this research is to provide a defect inspection system including an image acquisition device, the layout panorama for a larger field of view, and crack map based on the combination of image processing technique and evolution algorithm. In that, the panorama has resulted from the image matching and stitching techniques. Firstly, to estimate the initial matching points, the easiest ways are to use similarity metrics of the intensity of pixels in the overlapped regions. To improve high accuracy of the image matching point, curvature measure and refinement technique are applied.

The input image data are collected from the video acquisition device consist of six common video cameras and three illuminators arranged on the frame work. The simple structure of this device is easily mounted on a conventional vehicle which can scan continuously to capture images of the entire tunnel lining surface. Moreover, this research also provides a semi-automatic crack detection algorithm to help user who can extracted

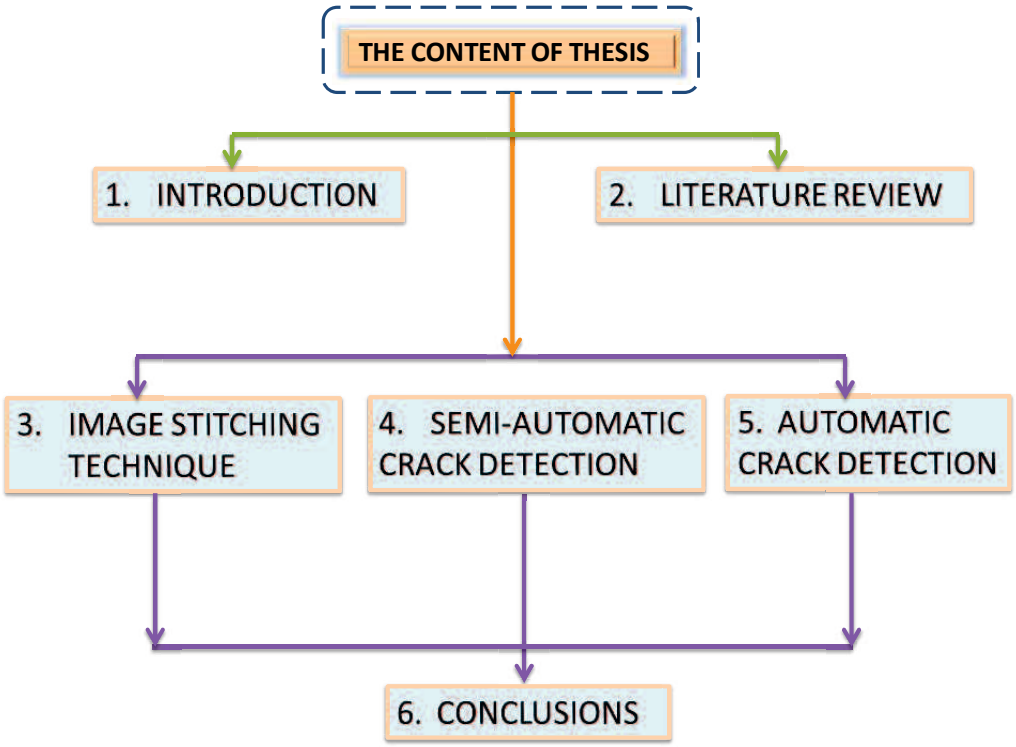

Fig.1.2 Scheme of this research.

cracks easily on the noise images without knowledge of image processing technique. To achieve this, the images of tunnel lining and bridge surfaces are taken with different multi resolution in complex environmental conditions. Further, an automatic crack detection method based on mathematic morphology and genetic algorithm is developed to find a optimized parameter set for crack detection of a large number of the concrete infrastructure elements.

1.3 ORGANIZATION OF DISSERTATION

This dissertation is organized into six chapters shown in **Fig.1.2**. Chapter 1 introduces the research background and problem statement. Then it explains the research objective. Chapter 2 introduces a literature review of existing methods and current practical application in the field. Chapter 3 shows an image matching method based on the curvature of cost curve for producing tunnel lining panorama. Chapter 4 presents a semi-automatic crack detection method using image processing technique combined

interactive genetic algorithm (iGA). Chapter 5 shows an automatic crack detection method for concrete infrastructures based on image processing technique and genetic algorithm. Chapter 6 concludes the contributions in the study, limited problem, and solved approach in the future research.

CHAPTER 2

LITERATURE REVIEW

2.1 INTRODUCTION

One of the greatest challenges engineers face is the inspection, assessment, maintenance and safe operation of the existing civil infrastructure. This includes large-scale constructs such as tunnels, bridges, roads and pipelines. In the case of tunnels (water supply, metro, railway, road, etc.), they have increased in both total length and number, and will continue to do so. Furthermore, some tunnels still in service were completed over 50 years ago, with the existing construction and materials technology.

Damage mechanism of tunnel lining typically appear due to ageing, external impacted factors such as earth pressure, the deterioration of the lining materials, environmental conditions, increased loading, disaster, damages caused by human, inadequate or poor maintenance, and deferred repairs, ect. Unfortunately, in the past, there were several accidents related to the structural condition of tunnels, such as the Big Dig ceiling collapse in 2006 in Boston. In 1999, incidents of the spalling of concrete linings occurred in the Fukuoka Tunnel and in the Kita- Kyushu Tunnel along the Sanyo Shinkansen (Bullet Train) line and in the Rebunhama Tunnel along the Muroran Main line.

These accidents urged an instant need of automatic, cost-effective and exhaustive inspection of the tunnel that prevents such catastrophes. An automatic inspection system for the tunnel comprises of defect detection and condition assessment to grasp whether or not deterioration (deformation) has an influence on the structural safety and durability and then to have appropriate countermeasures to remedy the function of the tunnels based on the evaluation results Asakura et al[2].

Therefore the defect identification is a crucial task for implementing successful inspection of the tunnel lining. The defects commonly occurred in the existing concrete lining are cracking (traverse, longitudinal, horizontal, diagonal, random) water leakage, spalling, staining, cavity, honey-comb. Steel structures: corrosion, cracks, buckles and kinks, leakage, protective layer fail. The walls of most tunnels are made of concrete, though these walls may contain finishes such as ceramic tiles or metal panels. In most cases, the typical defects found in a tunnel are cracks, spalling and efflorescence/leakage. In most cases, the typical defects found in a tunnel are cracks, spalling and efflorescence/leakage Park.S et al[7].

The purpose of inspection is to grasp whether or not deformation has an influence on structural safety and durability and then to take proper countermeasures to secure the function of the tunnels based on the evaluation results. Thus, the inspection of a tunnel and the resultant diagnosis are the most basic parts of the maintenance and the management of a tunnel.

2.2 TUNNEL INSPECTION METHODS

According to Asakura et al[2] 'Inspection' means an examination of the soundness of a tunnel based on a comparison of the investigation, observation and measurement results according to the judgment standards. Meanwhile, a 'diagnosis' means an evaluation of the investigation, observation and measurement results on the basis of past experience and knowledge and a comprehensive proposal of the evaluation of the structural functions and countermeasures taking into account the inspection results. Inspections are divided into two stages including primary inspection and second inspection.

In the primary inspection, the purpose is to check if a structure that has been functional for years is still safe or not. Furthermore, it is desirable to do this without creating any negative effect on the structure or component, and this is why the non-destructive testing (NDT) methods are far more commonly used than destructive methods. NDT methods in structures can be divided in visual, strength- based, sonic and

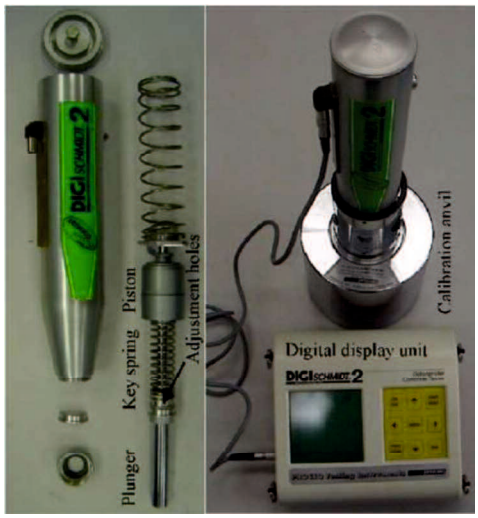

Fig.2.1 Components of Schmidt hammers[8].

Fig.2.2 Inspection using an impact hammer[8].

ultrasonic, magnetic, electrical, thermography, ground penetrating radar (GPR), and vision.

2.2.1 Strength based method

This method estimates the hard surface compressive strength of the materials by measuring rebound or penetration tests. Example of the Schmidt Hammer is when the hammer is pressed orthogonally against a surface, the piston is automatically released onto the plunger and the rebound height of the piston is considered to be an index of surface hardness, as shown in **Fig.2.1**.

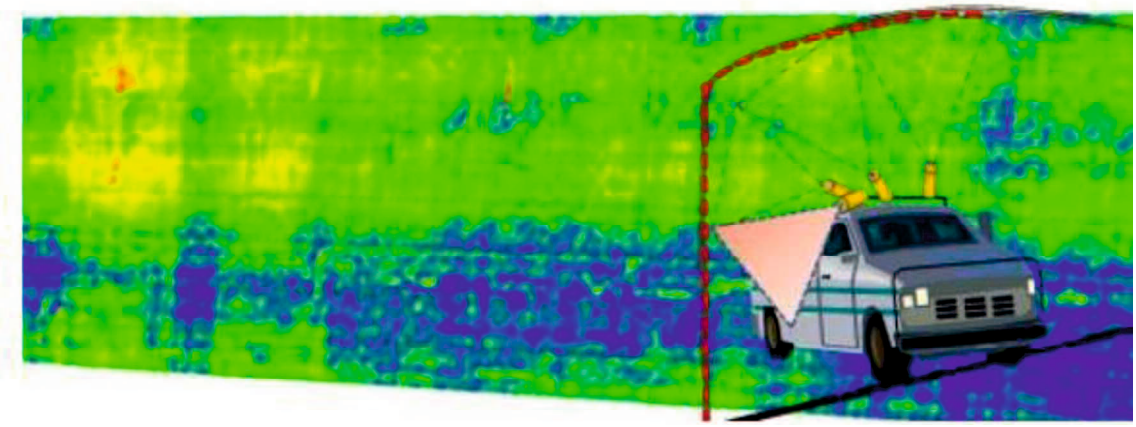

Fig.2.3 Inspection result using the infrared cameras[9].

2.2.2 Sonic and ultrasonic methods

In sonic methods, also known as impact-echo tests, hammer blows create impulses, and the time of travel of these sonic pulses is measured with pickups placed on the wall, as can be seen in **Fig.2.2**. Ultrasonic devices are normally used by measuring the velocity in the material of a pulse generated by a piezoelectric transducer. The pulse velocity depends on the composition and maturity of the structural material and its elastic properties. The relationship to strength depends on several other properties and is best determined experimentally Blitz et al[8].

2.2.3 Magnetic method

This method is used to measure dept of concrete cover from magnetic field distortion caused by a reinforcing bar. This method requires knowledge of the bar diameter with accuracy ± 5mm in 100mm.

2.2.4 Infrared Thermography

An infrared camera detects radiation in the infrared range of the electromagnetic spectrum and produce images of that radiation. The amount of radiation emitted by an object increases with temperature; therefore, thermography allows one to see variations

in temperature. This method is commonly applied to determine locate areas of near-surface delamination/ cracking in concrete decks, facades and similar structural elements. It requires expertise to interpret thermal images. Dust and air are able to interfere with readings. For example, **Fig.2.3** shows a thermal images using infrared camera.

2.2.5 Ground Penetrating Radar (GPR)

This is a geophysical method that uses radar pulses to image the subsurface. Electromagnetic radiation detects the reflected signals from the subsurface. Application of this method is to measure concrete wall thickness, detect voids between concrete and test grouting, to identify water leakage and movement behind linings and pavement. It is capable of detecting cables and pipes. Drawback is poor performance in high-conductivity materials such as clayey soils, high cost, low measurement speed, and requires experts to interpret the results.

2.2.6 Visual inspection methods

Visual inspection is a common method of quality control, data acquisition, and data analysis. Visual Inspection, used in maintenance of facilities, mean inspection of equipment and structures using either or all of raw human senses such as vision, hearing, touch and smell and/or any non-specialized inspection equipment. Collection of image or recording video data. These inspection methodologies do not require specialized equipment, training.

Visual inspection is a common technique used by inspectors. Structural components are examined based on the experience of the inspectors, who will assess the conditions of the structures based on their visual appearance. Inspection must be carried out within an arm's length of an inspector, although this is very difficult in many inaccessible areas, such as ventilation shafts, which are usually narrow. After visual inspection completed, inspectors report the inspection results that contain sketches of the defect areas. The visual inspections face some problems such as cost, time, and accuracy. Therefore, it can't be performed more regularly. The inspection cost is high because of many required inspectors, and the inspecting work is implemented by human eyes so that it

takes much time. Moreover, accuracy of the visual inspection results is subjective because of based on the judgement of each own experience inspector.

Development of low-cost digital video cameras yields a high inspiration for computer vision based IPT application to detect defects of the civil infrastructure. Therefore, in recent years, many researchers have developed automatic or semi-automatic crack inspection. Acording to Chaiyasaro[3)], these defect inspection systems can be categorized into the following: detection, visualisation and interpretation. This chapter introduce a detailed review of the inspection system based on both image processing technique acquisition equipment, and evolution algorithm. Drawback and advantage of image based inspection systems are discussed.

2.3 CRACK DETECTION BASED ON IMAGE PROCESSING TECHNIQUES

In recent years, the automation of visual inspection using various sensors and information processing technology is a very active area of research. Depending on concrete structure types, locations of the cracks, there are conformed methods. For instance, foundation inspection often used ultrasonic method, machine vision. Pipeline inspection system, underground structure often used ultrasonic method, machine vision image processing. Concrete structure of bridges, tunnels, buildings usually used visual inspection, image processing technique (IPT).

Table.2.1 General image processing technique[10)]

Image acquisition Device	Image processing technique				Optimization Tools
	Pre-processing	Segmentation	Feature-based methods	Model-based methods	Genetic algorithm (GA)
Digital Camera	Median filtering	Threshold	Haar-wavelets	Percolation-model	Swarm Optimization Algorithm (PSO)
VideoCamera/ vehicle inspection/railway	Morphologic operations	Edge detection	Hough transform	Graph-based search	Artificial Neural networks (ANN)
Robotic/sensor	Histogram equalization	Region growing	Laplacian of Gaussian	Image stitching	Fuzzy logic
Fly cam/ Aerial Vehicles	Background subtraction	Clustering	Background subtraction	Image registration	Hybrid algorithms
Line sensor camera	Garbor filtering	Wavelet transform	Multi-temporal methods	Line-tracing algorithm	Super vector machine

Koch et al[10)] reviewed computer vision based defect detection and condition assessment of concrete and asphalt civil infrastructure with general image processing techniques for automatic crack detection shown in the following **Table.2.1**. There are four approaches of the IPT that is presented in detail as follow:

2.3.1 Threshold techniques-based methods

Cracks are detected based on an assumption that pixels belonging to crack regions are darker than those in the neighbouring regions. Therefore, this method relies on thresholds, which can be applied either globally or locally, to extract the regions of the cracks. Many filtering techniques such as median and morphology filters are applied to smooth the original images to reduce noise and after that using background subtraction to enhance sharpness of the cracks.

Miyamoto et al[11)] calculated the difference in intensity between each pixel and the average intensity of each row in an image. A pixel that differs considerably from the average is said to be a crack pixel. Fujita et al[12)] used a line filter based on the Hessian matrix to emphasize line structures associated with cracks before they apply

thresholding to separate cracks from background. The major drawback of threshold-based approaches is the question on how to choose a suitable threshold for extracting crack features. The described algorithms select a threshold based on prior knowledge. However, such methods can hardly be generalized and may be inapplicable to the imaging conditions found in real tunnel images. Moreover, they are prone to inaccuracy caused by shadows as the intensities of shadow pixels tend to have a similar brightness compared to crack pixels.

2.3.2 The edge-detection based technique

Abdel-Qader et al[13] analysed the efficacy of different edge detection techniques in identifying cracks in concrete pavements of bridges. They compared various edge detection algorithms and found the Haar Wavelet method to be the most reliable among traditional edge detector such as sobel, canny, and fast fourier transform (FFT) for the purpose of crack detection.

2.3.3 Model-based technique

Ukai[14] developed a crack detection system for the tunnel wall. Under this method, the model of a crack is characterized by eight quantities, such as area and Feret's occupancy rate. Subsequently, a filter is used to remove noise. Yamaguchi et al[15] used scalable local percolation-based image processing techniques and they proved to be efficient and accurate even for large surface images. The algorithm starts by initializing a seed region and then the neighboring regions are labeled as crack regions based on the percolation process. Paar et al[16] proposed a crack detection algorithm based on the line tracing algorithm. In this algorithm, a crack is assumed to be a series of short straight lines connected together. The algorithm starts from a seed point and then searches for a line within the neighbouring regions. Once a line has been detected, a connection is made to the previous line, and the algorithm continues.

2.3.4 Pattern recognition based technique

In this theme of detection algorithms, pattern recognition is applied to obtain semantic information from image or video data. Zhu and Brilakis[17] proposed an

algorithm for detecting concrete columns based on texture using artificial neural networks. Liu et al[18] applied a Support Vector Machine classifier to classify if crack features appear in an image patch, which is pre-processed to extract potential crack features based on intensity. Abdelqader et al[19] applied a Principal Component Principles (PCA) algorithm, which can be used to reduce the dimensions of feature vectors based on eigenvalues, to extract cracks from concrete bridge decks. The images are first pre-processed by line filters in three directions: vertical, horizontal and oblique;then further processed by the PCA algorithm and classified based on the nearest neighbour algorithm.

Methods based on pattern recognition considerably rely on training data in order to set up robust classifiers. Training and validation data are usually performed by manual labeling (supervised learning), which is a labor-intensive and error-prone procedure.

All abovementioned approaches are developed by empirical or trial and error on the basis of previous knowledge. Moreover, their applications are almost limited to specific types of images and the purpose. These techniques are hence unsuitable for detecting complex types of the cracks on various background images which have varied characteristics such as tone, shape of targets, shading, artifact, noise, ect. Therefore, this research is interested in solving the optimization problem of the image processing parameters.

Automatic crack detection for concrete tunnel lining also tempts many researchers. For illustration, Zhang et al[20] proposed the crack detection system divided into six phases shown in **Fig.2.4**, as following presentation. The original tunnel images are collected by CMOS line scan cameras shown in **Fig.2.5**.

These color images are transferred into gray-scale images for further processing. Firstly the collected images of the nine line scan cameras are stitched together to eliminate overlapping regions. To eliminate the unnecessary local small valleys, an average image-smoothing filter is applied to the original gray-scale images for image processing. In Stage 4, a black top-hat transformation is applied to detect the local dim regions, which contain potential long and dark cracks. Subsequently, objects with low gray levels and large pixel numbers will be segmented by a thresholding operation and morphological area opening. Lastly, the numerical features will be extracted as the input of a classifier, and objects preserved in the final output image will be regarded as

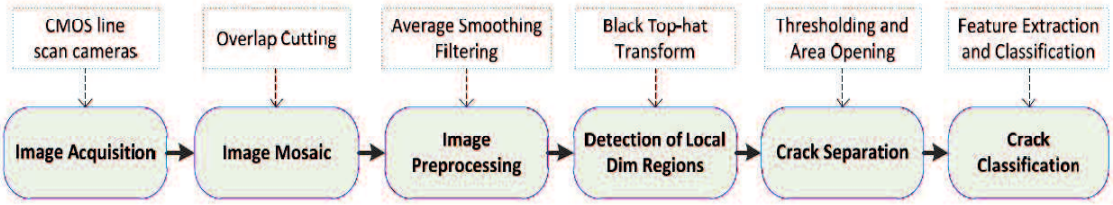

Fig.2.4 Automatic crack detection for the tunnel wall procedure[20].

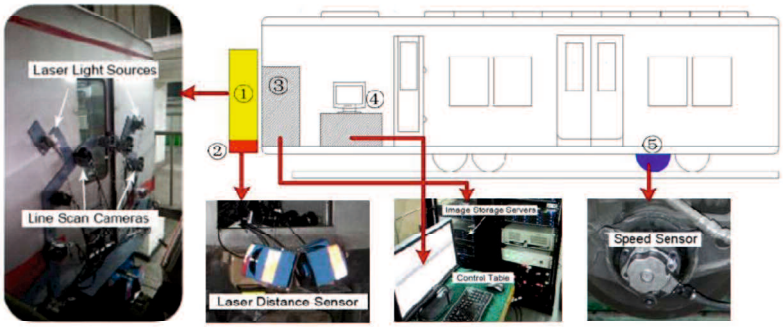

① image sensing terminal; ② laser distance sensors; ③ image storage and processing servers; ④ central control system; ⑤ speed sensor.[20]

Fig.2.5 Image acquisition system for subway tunnel monitoring.

cracks. Subsequently machine learning techniques are applied to classify and compare the accuracy of different classifiers. The results of this study reported that have over 90% of cracks which are correctly classified. Further, setting parameters of IPT are performed by using empirical method.

Shen et al[21] proposed a subway tunnel crack detection method based on wireless multimedia sensor network, as shown in **Figs.2.6** and **2.7.** This system proposed a new subway tunnel crack detection method and designs a subway tunnel crack detection system based on a wireless multimedia sensor network. This system includes four components: a vehicular wireless multimedia sensor node, a station sink node, a cable transmission access module, and a central server. **Fig.2.6** shows how the system operates.

Step1. A vehicular wireless multimedia sensor captures an image, stores image, and disposes and compresses the image in accordance with default parameters when the

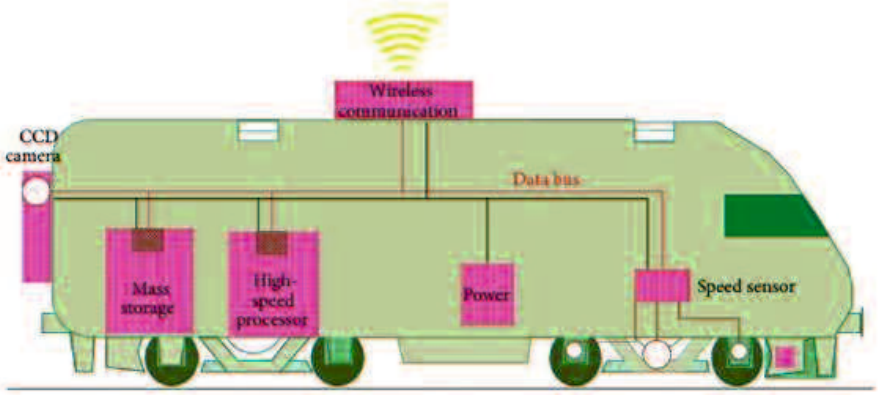

Fig.2.6 Diagram of development of VWMS on a train [21].

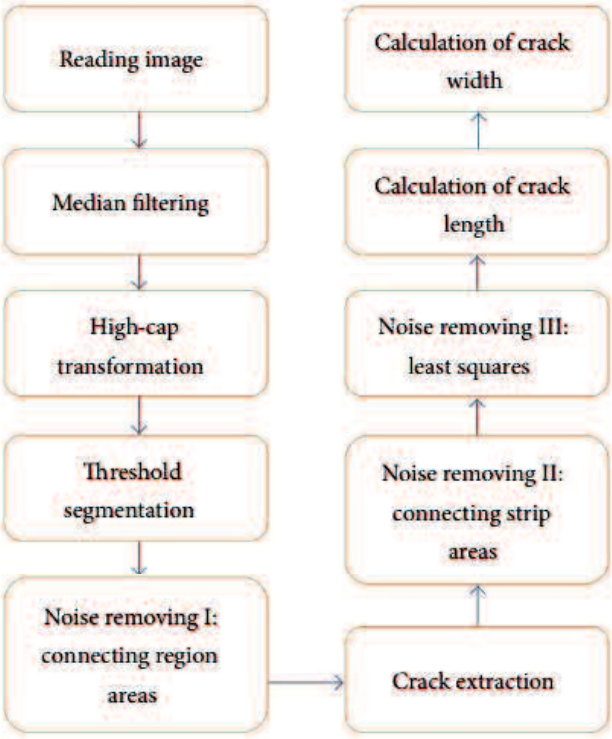

Fig.2.7 Crack detection procedure of this system[21].

train runs through a tunnel. During this phase, data does not need to be transmitted. Step2. When the train arrives at a station, the vehicular wireless multimedia sensor transmits all of the compressed images from the previous tunnel to a station sink node via a wireless network. Step3. After receiving the data, the sink node transmits the received image data to a central server though a cable transmission access module.

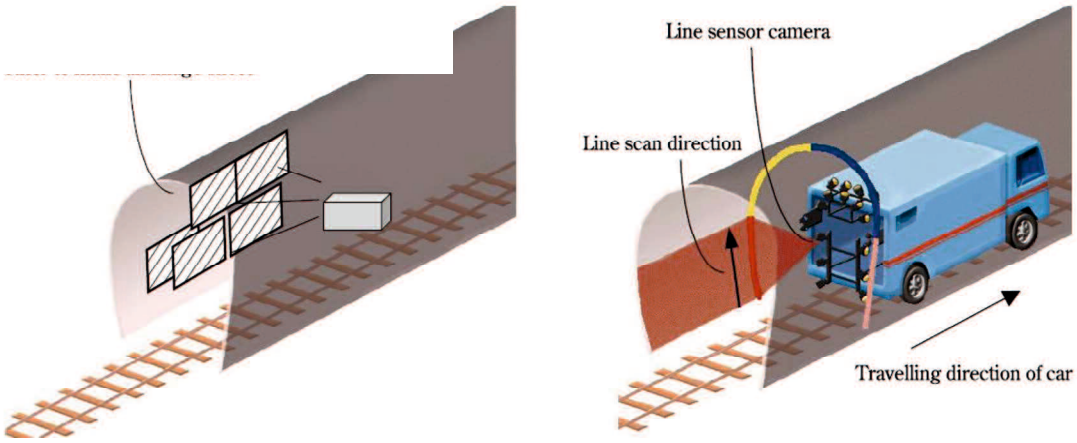

Fig.2.8 Image of tunnel wall obtained by two dimensional CCD Camera[22].

Step4. The central server processes the received data by using a new subway tunnel crack detection method and analyzes the results. If there is a serious crack detected, the central server can find the original image on the basis of various requirements.

Step5. An administrator can check the detection results directly on the central server and can also remotely access data in real time from the central server via an internal company network.

This system obtains significantly meaningful results with two noise-removal steps for crack detection, but it needs a very complex equipment and even more expensive.

Ukai and Nagamine [22] developed an inspection system of railway facilities using continuous scan image, as shown in **Fig.2.8**.

(1) Because the higher resolution pictures can be seen on the display without going to the field, using this system can save the labor and time and can do inspection and diagnosis anytime we want.

(2) Accumulating the inspection data enables us to grasp the time series condition of the facilities and to plan and perform efficient maintenance and reformation.

(3) With the image processing make easy, a comprehensive analysis of various data including design data and maintenance history becomes available.

(4) Inspection becomes quick, efficient, and precise using the automatic diagnosis program to which the image processing method is applied.

(5) By exchanging information with each terminal which is located in each maintenance section, maintenance becomes quick and efficient.

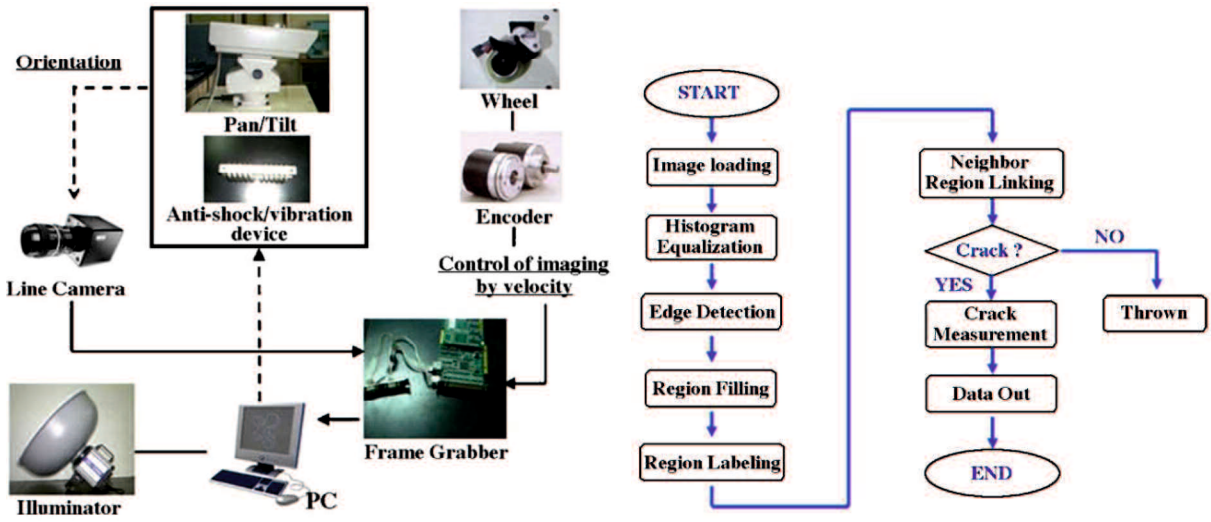

Fig.2.9 Mobile tunnel inspection system[23].

This image scanning system is used on railways, so it is not applied to road tunnels yet. Besides, image-collection speed is about 20 Km/h relatively slow to be able to affect conventional traffic flow.

Yu et al[23] proposed an automatic inspection system using a mobile robot for detecting concrete cracks in a tunnel shown in **Fig.2.9**. This system consisted of a small robot equipped with CCD camera and kept a constant distance of the tunnel wall.

An industrial camera is mounted on an anti-vibration equipment to stabilize the quality of images. The movement of this imaging system is through the independent actuation of the wheels. Obtained images from the imaging system have detected the cracks automatically under the computer vision assistance.

This imaging system only used a CCD camera so that the speed of image collection for the entire tunnel or large-size structures is slow. According Egnal et al[24] to CCD camera typically attains noise in the obtained images such as fixed pattern noise. Dark energy, and dead pixels that no longer function.

M. Gavilán, et al[25] proposed a mobile inspection system for high-resolution assessment of tunnels shown in **Fig.2.10**. The laser-cameras unit used for bimodal (road-rail) all-terrain truck is based on cameras and laser sensors that allow scanning a tunnel's lining at speed up 30 km/h. It can hold up to six laser cameras. Each pair of laser-camera units inspects a 2 m wide section with accuracy of 1mm. Using the six

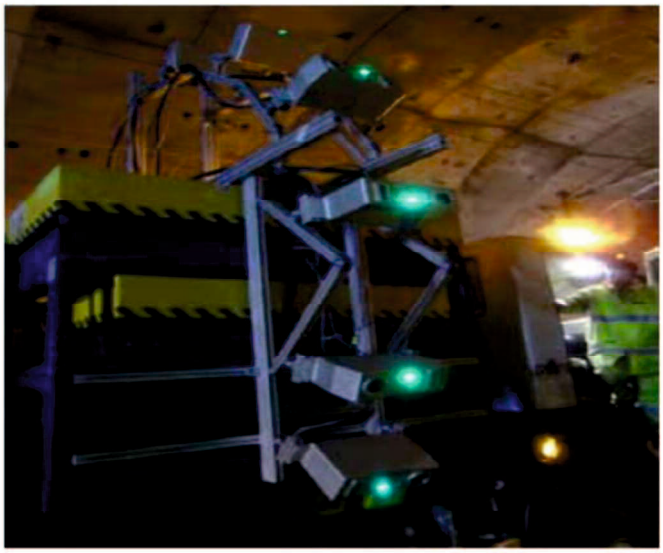

Fig.2.10 The tunnelling system sensor structure[25].

cameras, tunnels with a 9m diameter can be inspected at the system's maximum resolution. Advantage of this system achieves high accuracy of crack detection and areas with missing or chipping lining, dampness and running water, and can structure evaluation using 3D reconstruction. However, this system requires high-level expertise to analysis and process images leading to high inspecting cost.

2.4 LAYOUT PANORAMA CONSTRUCTION FOR TUNNEL LINING INSPECTION

2.4.1 Review of using different image acquisition technique

Panoramic imaging from multiple images is either a camera rotated about its optical centre, or using multiple cameras capturing different areas around them.

(1) Image acquisition system by single camera

Panoramic imaging from multiple images is either a hand-held camera rotated about its optical centre or moving the camera centre via parallel direction with the object surface.

(2) Image acquisition system by stereo cameras

In the described system, the robot will detect, recognize and document (visually and geometrically) the selected defects on the tunnel lining in a single pass.

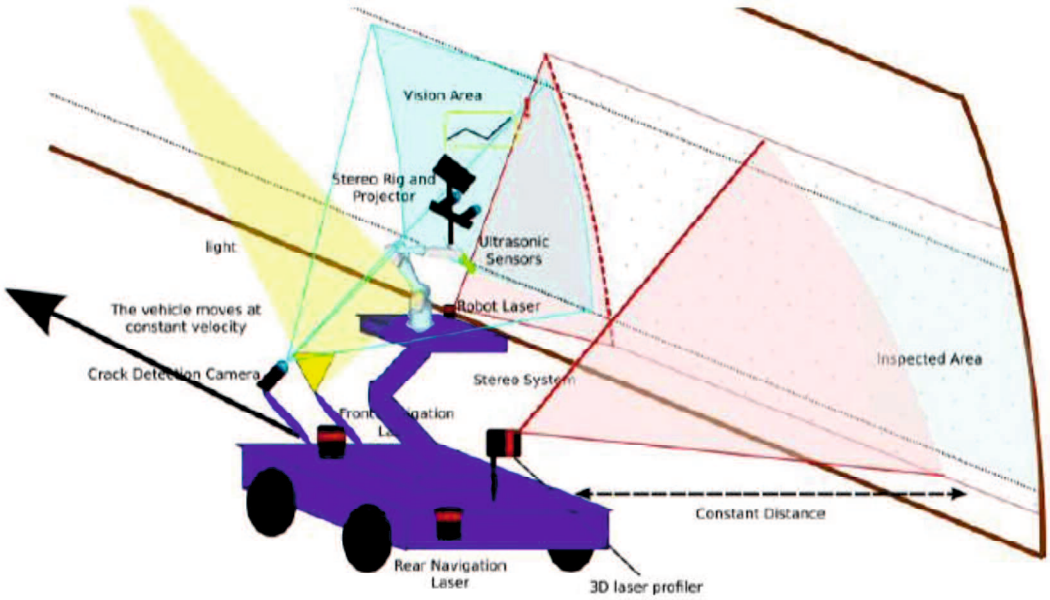

Fig.2.11 Overall graphical representation of the robotic platform for tunnel lining inspection[26].

The computer vision system is a core component of the procedure, as it implements the following major functions; the initial real-time detection of defects, while the robot navigates in the tunnel; the stereo-camera imaging for real-time 3D robot guidance and off-line accurate 3D reconstruction of surfaces that include structural defects; the 3D scanning of traverse tunnel sections, in order to detect lining deformations shown in **Fig. 2.11**. This pipeline is realized through single and stereo machine vision cameras, a customized 3D laser scanner and a processing unit that runs the algorithms and stores the collected data.

(3) Image acquisition system by multipe cameras

Fig.2.12 shows a imaging device for railway tunnel 3D surface inspection based on a multi-camera, structured-light vision system (MSVS) and a vibration compensation component. DongZhan et al proposed a global calibration for the MSVS to acquire the high quality of image data[27]. Howerver, the image equipment is more complex and so high expensive.

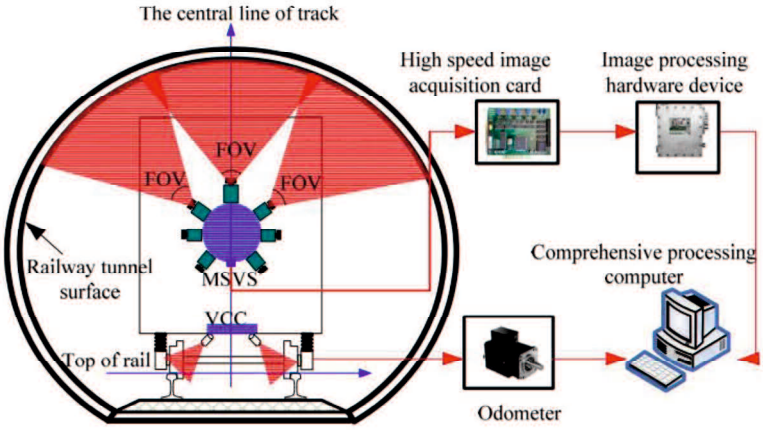

Fig.2.12 The vision measurement principle. MSVS, multi-cameras and structured-light vision system[27].

2.4.2 Layout panorama construction for tunnel lining inspection

The main purpose of the panoramic image construction is to aid inspector an enhanced visualization from a single-wider image. As the images or videos become large, it is vital to arrange and align data to be able to visualize the data clearly.

Therefore stitching method is simple way to combine a number of consecutive images to form a large image depending on registration and blending techniques. Jahanshahi et al[28] create stitched images of structural systems from a specialized camera that can tilt and pan. The method detects missing parts such as bolts when comparing images taken at different times. The method applies a machine-vision algorithm to perform image registration to rectify images so that they are in the same coordinate frame. In general, image stitching provides a good way of increasing the field of view that cannot be achieved by a single image. Consequently, a wide-angle or stitched image may improve defect detection results, in particular in case of hairline cracks since the stitched image provides a higher resolution of defects, e.g. cracks.

The methods reviewed above, however, can only handle a small number of images. This is because a mosaic is created based on a homography model in which a camera centre must be fixed at a single point. This method does not allow the translation of a camera. Chaiyasarn et al used a hand-held camera and a supported tripod[3] to move

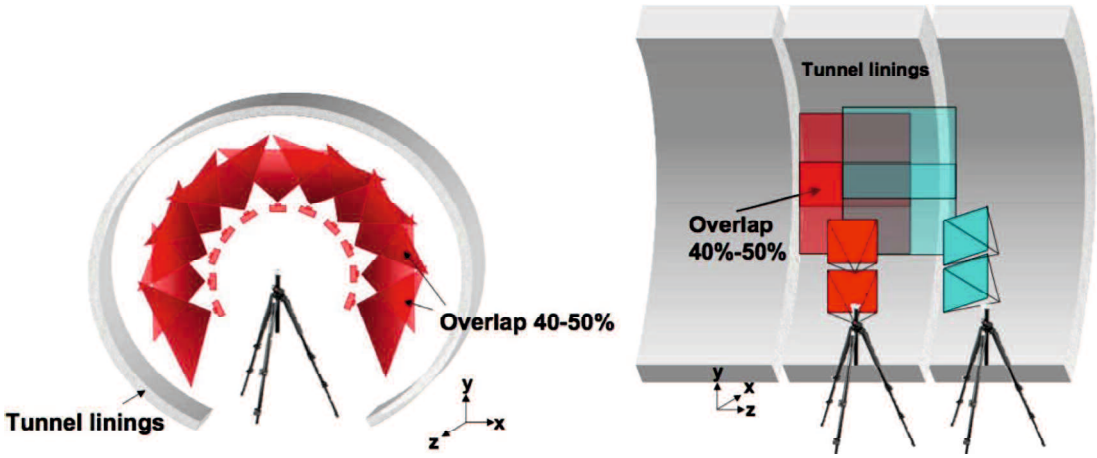

Fig.2.13 Image acquisition procedure[3)].

camera center with the purpose that takes consecutive images of the ring of tunnel lining as **Fig.2.13**. This imaging approaches yield in the high resolution image and flexible movement of the digital camera when photographing at the required special location. However, this equipment takes much time for collecting the entire tunnel lining with the long length. Moreover, each pass step has to measure distance from the camera centre to tunnel surface. This system movement has both translation and rotation so that geometric transformation among collected data is very complex.

Table.2.2 shows a summary of the related researches for tunnel panorama generation. The table reports advantage of each method of each researcher. From that, the author provide a finding of each studied field. This is reason that a defect inspecting system using six video cameras for tunnel lining based on image processing techniques is proposed.

2.5 PROPOSED DEFECT INSPECTION FOR TUNNEL LINING

Providing a defect inspection system based on image processing techniques with video cameras achieves reasonable effectiveness for tunnel lining inspection including three criterion as follow:

Table.2.2 Summary of the related researches for tunnel panorama generation.

Authors/ Years	Title of paper	Methods	Dominated effectiveness	Findings
Ukai 2000	Development of **image processing technique** for detection of **tunnel wall deformation** using continuously scanned image	**SURF** feature detector for image stitching. **Dilation** and **Erosion** transform for crack detection.	Cracks/Defects detection and vertical and horizontal joint elimination. Using **multi-video cameras**.	Image-collection speed is about **20 Km/h.** Using exclusive vehicle for rail way.
Chaiyasarn 2011	Damage Detection and Monitoring for **Tunnel Inspection** based on Computer Vision	**SIFT** feature detector, Ransac, **SfM** bundle (3D Point cloud+camera calibration), surface estimation, **SVM** for classifier	**3D scene reconstruction** for the **shape inspection** of the tunnel lining.	**A hand-held camera**. At each image shooting step at a location, multi-images need to be acquired for a large scene.
M. Gavilán, et al., 2013	Mobile **Inspection System** For High-Resolution **Assessment Of Tunnels**	Proposed a mobile inspection system for high-resolution. Using **tunnelling software** to extract the profile of the tunnel.	**3D reconstruction using laser multi cameras** with high-resolution. The inspection result obtains high accuracy	High cost inspection and required expertise level
Zhi-Heng Zu (2016)	Panoramic Image Stitching for Arbitrarily Shaped **Tunnel Lining Inspection**	Feature detection and matching, **3d reconstruction** using **SfM**.	**3D reconstruction** of the arbitrarily **shaped tunnel lining inspection**. The acquired quality images.	**A hand-held camera**, the time of the obtained image so long. **Complex geometric transformation.**

There are cost, accuracy, and time. If the inspection system have too high accuracy for hair–size crack and fast inspection time then leading to high inspection cost, for example: laser scanner, robotic tunneling, MIMM-R…ect. If the inspection system has low accuracy for defect detection and low inspection time then leading to low inspection cost. For example: manual vision inspection.

The authors proposed a defect inspection system inspection for tunnel lining shown in **Fig.2.14**. The system consists of two parts. The first part is video/image acquisition device, which is developed by Sumitomo Mitsu Company, mounted on an inspection vehicle to acquire tunnel lining surface images. Next, panoramic image is created by image stitching for enhanced visualization. The second part is crack extraction to create a crack map. In this research, the two parts are implemented and made experiments independently.

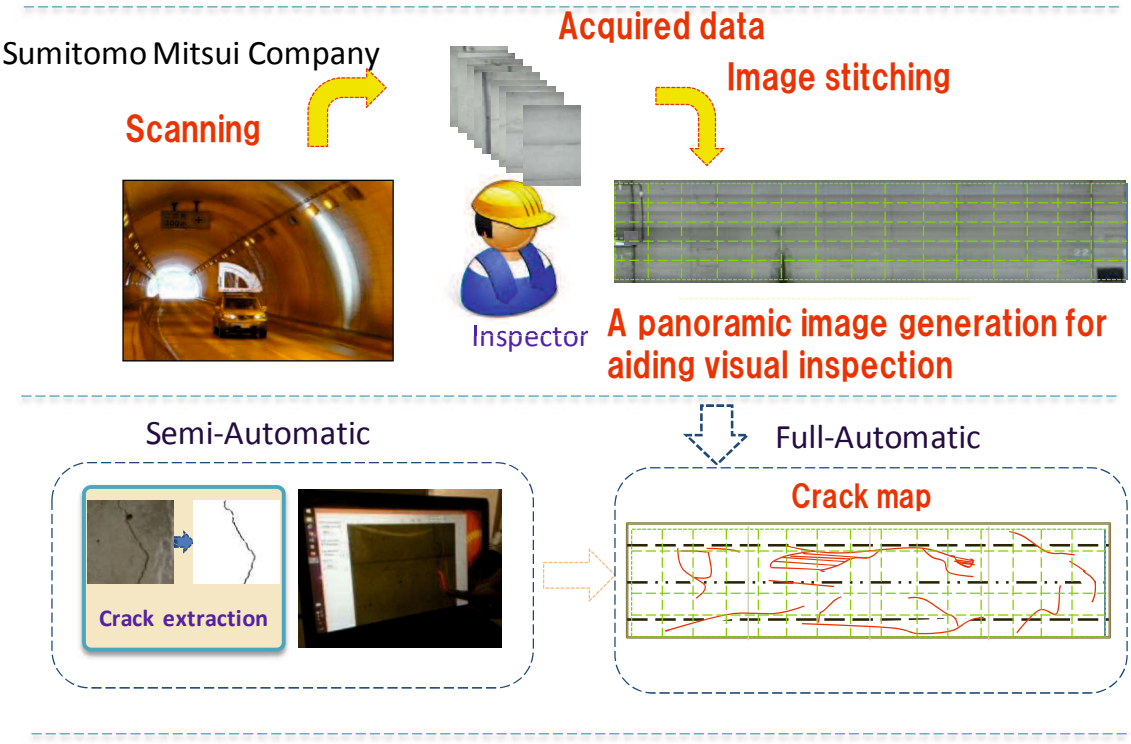

Fig.2.14 Proposed defect inspection system for tunnel lining.

Therefore, an image acquisition system was developed by Sumitomo Mitsui Company with a simple and effective structure that obtains sufficient image data for objective and precise quantification. The imaging system includes six video cameras and three illuminators mounted on the steel framework optimally in order to ensure the quality of the obtained images. In addition, this device can slide from the side to the top of the car so that the full tunnel lining surface can be captured by several passes through the tunnel.

Furthermore, image stitching software was developed to create a full view of the tunnel wall surface image automatically. Because the collected data have major parts contained the blank wall images of the tunnel, feature-extraction based image registration is not used. Furthermore, a huge of images of the full tunnel should consider a simple image-matching method and then using a correction technique based on the parameters of the imaging speed is better than any complex registration techniques.

In this study, a global and local correction method is presented that adjusts mis-registration error of the initial matching points using similarity metrics in the automatic

image stitching according to the tunnel longitudinal direction. Moreover, author proposed a curvature metric of the nearest-neighbor pixels as well as the pixel being processed to improve the accuracy of the image-matching location.

Consequently, an image stitching prototype software which makes use of available matching information among consecutive image pairs is developed to stitch images. As a result, this software creates layout panoramas in both longitudinal and circumferential directions for 1558 images in each camera.

This production provides a wider and detailed field of view of the tunnel lining to assist inspectors who can inspect defects easily with visualizing it off-line. Moreover, from original image data, we proposed two semi-automatic and automatic approaches to detect cracks based on the image processing techniques and optimized parameter-adjustment algorithm. Genetic algorithm and interactive genetic algorithm are applied to find optimum parameters of IPT for various complex images.

CHAPTER 3

AN IMAGE MATCHING METHOD BASED ON THE CURVATURE OF COST CURVE FOR PRODUCING TUNNEL LINING PANORAMA

Human inspection of defects of concrete tunnel lining is usually slow, laborious, and disruptive to traffic. This necessitates automated alternatives using sensors and computer-aided processing. The conventional image-matching methods only use the cost value of the pixel being processed based on similarity metric to estimate an image-matching location. To improve the image-matching efficiency, this paper proposes an image-matching method that relies on the curvatures of the cost curve at candidate matching points. This is followed by applying a median filter to mitigate the matching errors. Moreover, experimental results for an actual tunnel demonstrate that the curvature measurement can select the matching points accurately. The authors have developed an image-stitching software to create a high-resolution panorama of the tunnel lining surface for assisting in defect inspection.

3.1 INTRODUCTION

Many transport infrastructure structures, including buildings, bridges, and tunnels, have been in use for over 50 years in Japan. If abnormalities in these structures (cracks, leakage, spalling, cavity, etc.) are not detected and properly treated, the structures may deteriorate or eventually be damaged.

This study focuses on defect inspection of tunnel lining. One of the most important tasks for preliminary tunnel inspection[29)] is creating a layout map. To identify changes on the tunnel lining surface, visual analysis techniques are often used in practice[2)]. There are three main approaches to visualize abnormalities of the tunnel lining: manual

drawing, image mosaicing approaches by hand camera, and tunnel scanning by multi-cameras.

The first approach is to draw a layout map of abnormality positions via visual inspection on the site. This approach is simple to perform at the expense of positioning accuracy and speed of inspection. The second approach[3), 29)] commonly uses a hand-held camera to capture images with an auxiliary positioning equipment and an illuminator. This approach yields higher inspecting speed, improved accuracy, and low cost. However, the main drawbacks are the long image acquisition time for large-size tunnels and disruption to traffic. At each image shooting step at a location, multi-images need to be acquired for a large scene. To capture the images of the full tunnel length, this step must be repeated at multiple locations. This image acquisition method results in complex geometric distortions because of many different camera positions. Hence a large number of raw original images have to be rectified before warping and stitching. This makes the approach less practical for inspecting large-size tunnels.

The third approach utilizes high-speed multi-cameras mounted on an inspection vehicle, and an illumination device to acquire images continuously. This allows constructing high-resolution 2D and 3D profiles of the tunnel lining. By far, this approach yields the fastest inspecting speed and the highest accuracy compared to the other approaches. However, the inspection cost is high as the approach requires high-precision laser scanners and special equipment[30)]. As the inspection device shifts parallel to the imaging plane, the obtained images are simple geometric transformation (e.g., translation) from the reference image. Both the image mosaicing and the tunnel scanning approaches can create a layout panorama.

To reduce inspection cost, Ukai and Nagamine[22)] used a tunnel scanner with line sensor cameras, which does not require a special vehicle, to continuously scan images for detecting tunnel wall deformations. This image acquisition system can be mounted on a railcar running at 20km/h and achieving a record resolution of 0.5-1 mm/pixel. This image scanning system is used on railways, but it has not been applied to road tunnels. Besides, the image matching algorithm is not presented in detail.

In recent years, many researchers have considered automated crack detection on the tunnel lining surface based on auto inspection [20), 23)]. However, they did not expound on tunnel panorama generation to assist visual inspection.

This study utilizes the tunnel scanning approach to provide the layout panorama for defect inspection on the tunnel lining surface. The goals are to achieve reasonable accuracy, active image-acquisition time, and manageable inspection cost. For image matching, the authors use color pixel-intensity-based feature and the curvature measure to find the appropriate matching points. This is different from standard image matching techniques that make use of key-point (feature)-based image matching methods such as SIFT, SURF[31], which may fail when the tunnel lining images contain noises or do not have many discriminated features.

Previously, the authors[32), 33)] proposed a Mobile Tunnel Inspection System (MOTIS) consisting of an image acquisition equipment and an image-stitching software for creating panoramic images. This software matches pixel brightness within the overlapped region. The initial optimal matching point is the position with maximum similarity value. The method is simple but effective in acquiring high-quality image data for inspection. More specifically, in the paper[32)], the authors used a full search method (*FS* method) and a correction technique based on the parameters of image acquisition device and inspection speech. The average matching error rate of six cameras was 33% before the correction technique was applied. After correction, the average error rate was reduced to 2.7%. In the subsequent paper[33)], the authors adopted a local search method (*LS* method) to check pixels around the estimated image-matching location, which was calculated using the parameters of the image acquisition device and inspection speech. As a result, the average error rate of image-matching locations was reduced to 3.45% before correction; and the error was eliminated after correction.

In this paper, the authors propose a search-strip method to extract candidate matching points from a search space based on the similarity metrics. Next, the precise matching point is selected from a curvature metric (*CUR*). This metric measures the sharpness of the peaks of the curve established from the matching point candidates. The matching accuracy is further improved by measuring the cost of Curvature function at the Nearest-neighbor Pixels and the pixel being processed (*CNP*). The experimental results demonstrate that *CNP* gives higher accuracy than *CUR*.

The remainder of the paper is organized as follows: Section 2 reviews the existing methods including the video acquisition system and image-stitching procedure. Section

3 proposes a new image-matching procedure, which consists of a similarity metric and its refinement. Section 4 reports the experimental results validating our proposed method against previous methods. Section 5 assesses the performance of the proposed search algorithm by evaluating the accuracy of image motion quantity (*IMQ*). The calculated *IMQ* is compared with the target *IMQ* based on the parameters of the imaging system and the manual image matching. The efficiency (time and accuracy) of this algorithm is compared with our previous published papers[32), 33)]. The section concludes with a description of an image-stitching software that makes use of the available image-matching information to produce tunnel panoramic images. This is followed by a discussion in Section 6. Finally, Section 7 concludes the paper.

3.2 EXISTING METHOD

In our previous papers[32), 33)], the authors reported a video acquisition system and a procedure of the image stitching for the entire tunnel lining as follows:

3.2.1 Image acquisition device

The video images of the entire tunnel lining surface are continuously scanned by a video acquisition system assembled on a car**. Figure 3.1 (a)** shows the system consisted of six digital video cameras (from V1 to V6) , three illuminators attached to the steel framework that its structure has shape appropriated with a half of cross-section of the tunnel, and a car. Further, this device can slide from the side to the top of the car so that the full tunnel lining surface can be captured by several passes through the tunnel. Each time has the rotation angle of 30^{o} as shown in **Fig.3.1 (b)**.

Figure 3.1 (b) presents the designed six regions to take images of the full cross-section of the tunnel lining in forward and backward directions. **Figure 3.1 (c)** shows how to obtain an image in each moved step of the system in the longitudinal direction of the tunnel. For example, in the tunnel scanning process, the image acquisition system takes six frames at six positions.

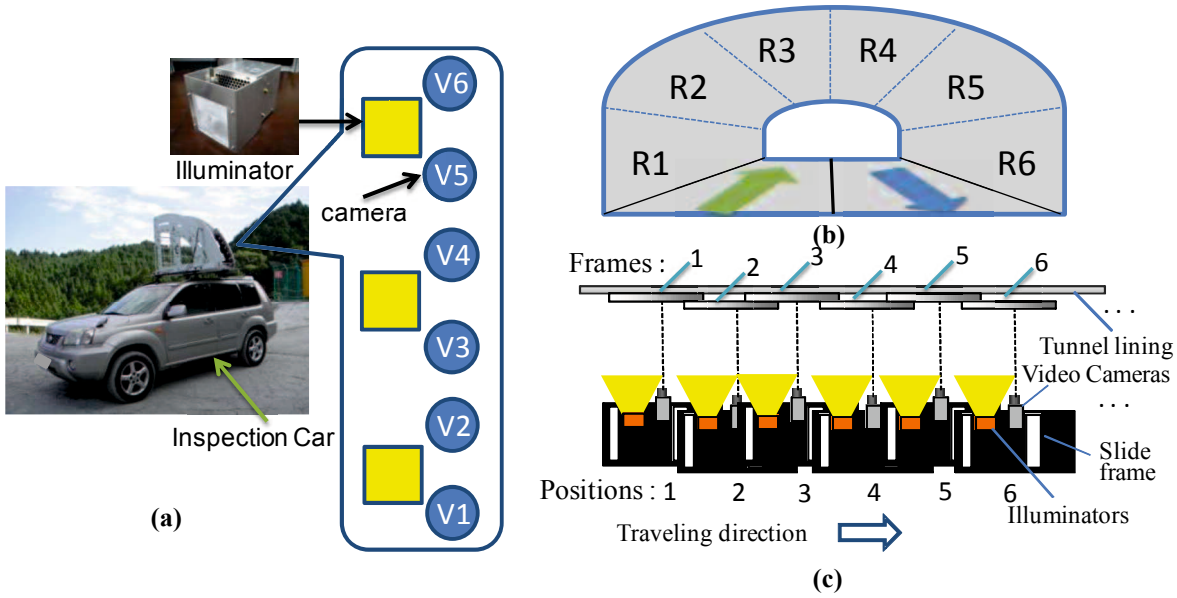

Fig.3.1 **(a)** Structure of image acquisition system; **(b)** Setting imaging regions for each pass; The full cross-section of the tunnel consists of six regions (R1-R6) with forward three times and backward three times; **(c)** Continuous video recording method.

Quality of the image data depends on many factors such as distance between the tunnel lining and inspection car, the illumination, and specification of video camera. This system is simple and does not require an exclusive vehicle. The video data are converted into the consecutive images with the specific overlapped region depending on the scanning speed of the video acquisition system. Due to the characteristic feature of the imaging system, the consequence image motion is only the translation, thus the rotation is not concern. Therefore, the direct method, which makes use of available information in the image-matching location, is applied to stitch images.

3.2.2 Procedure of tunnel lining image mosaic construction

Figure 3.2 shows an image stitching procedure for the entire tunnel lining including three steps. Captured image data are retrieved from six video cameras which each camera contains a number of images depending on the length of the tunnel. In Step 1, the dataset is connected to form a panoramic image in the longitudinal direction of tunnel for each camera. In Step 2, these panoramic images obtained in the step 1 are stitched in the circumferential direction of tunnel for each region corresponding to each pass. Subsequently, in Step 3, the connected images of the six regions (R1-R6) in step 2 are stitched together to make a layout panorama which consists of a full view of the entire tunnel lining surface.

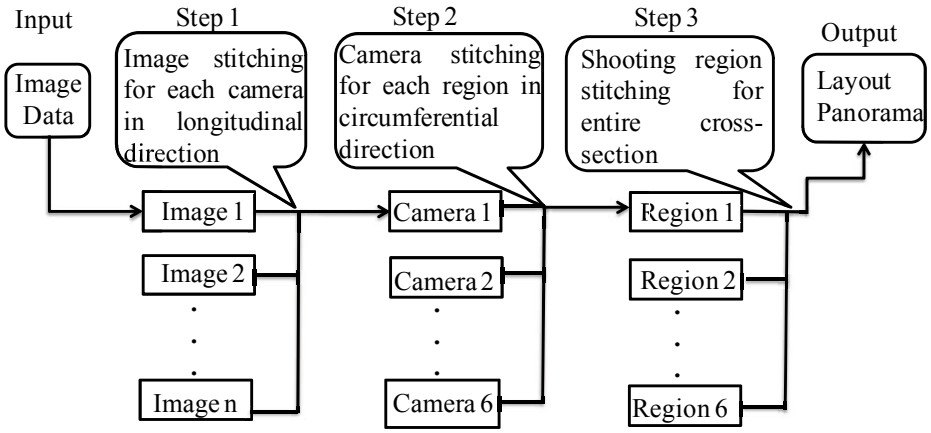

Fig.3.2 The panoramic image stitching procedure for the entire tunnel.

In this chapter, the automatic image-stitching method is used in Step 1. Semi-automatic methods are applied to Steps 2 and 3 because Steps 2 and 3 stitch images via the circumferential direction, and their accuracy depends on the accuracy of Step 1.

Therefore, the accuracy of Step 1 plays the most important role. Step 1 is presented in detail in the following section.

3.3 PROPOSED METHOD

The key to image stitching is to find the correct matching point for a pair of consecutive images. To this end, the authors propose a new image-matching algorithm, as follows: First, an initial image-matching location (IML) is estimated using Sum Absolute Difference (*SAD*) and normalized cross-correlation (*NCC*) measurements. Next, the images are matched using the Curvature of the cost curve at the Nearest-neighbor Pixels as well as the pixel being processed (*CNP*). Finally, the matching errors are corrected using the median filter.

3.3.1 Image matching procedure

Figure 3.3 illustrates the automatic matching process of two consecutive images in the tunnel longitudinal direction (X-axis). Here, image 1 is the referenced image, and image 2 is the registered image of the image matching process. A search area is set in advance. Each movement step of the search point is with respect to the location which

enables image 2 to be shifted onto image 1 to find the appropriate image-matching

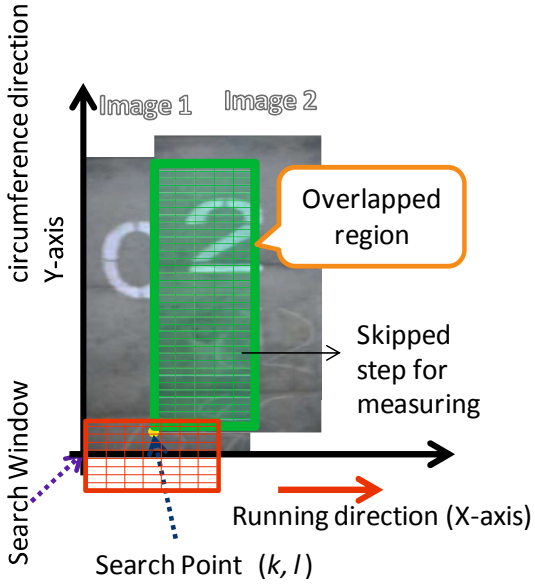

Fig.3.3 Searching process of image-matching location.

location by measuring the similarity and sharpness in the brightness of all pixel pairs in the overlapped region of the two images.

Furthermore, to accelerate the search and measurement process, the search point and similarity measurement are skipped in the search area and overlapped region with predefined values, respectively. The search process for the matching point is summarized in **Pseudo algorithm 1**. The search algorithm is detailed as follows:

(1) Similarity metric

In this study, matching cost functions to measure most intuitive similarity of the pixel intensity values within the overlapped region are used. Those are the most popular functions such as the sum of square difference (*SSD*), and the sum of absolute difference (*SAD*). More complex measure about angle correlation such as the normalized cross correlation (*NCC*) and Zero mean normalized cross correlation (*ZNCC*) get score in the interval [-1, 1] denoting matching cost functions (*C*) are used to measure intuitive similarity of the color pixel-wise pair in terms of brightness in the overlapped region, as in Eqs. (3.1) to (3.4):

Pseudosection algorithm 1. Matching point search.

1: **Input**: two consecutive images of each camera

2: **Output**: image motion quantity (IMQ)

3: **Setting initial parameters**:

- *a.* Predefined search area k∈[0, 810], l∈[-50, 50]. Skipped step for searching process (*xx1, yy1*), skipped step for measuring process (*xx2, yy2*);

4: Count=0; (counting number of images in a camera)

5: **While** Count ≤ total of images **do**

6: **For** k=0 to 810 with + xx1 skip **do**

7: **For** l=-50 to 50 with +yy1 skip **do**

8: **For** i, j=1 to size of image (columns and rows) with +xx2, yy2 skip **do**

9: **If** (0 ≤i-l≤ columns and 0 ≤j-k≤ rows) **then:**

- *a.* Moving the search point;
- *b.* Measure Cost (*SAD* / *NCC*);

10: **End if**

11: **End for**

12: Saving (k,*l*1) coordinates and cost of each candidate matching point;

13: **End for**

14: **For** t=1 to s-1; t+1 **do** (s is the total number of strip of the search area)

15: Measure *MSM*, *CUR* and *CNP;*

16: **End for**

17: Saving the location which has maximum *MSM*, *CUR* and *CNP* score;

18: **End For** (stop searching in the area)

19: **Count=Count+1;**

20: **End While**

$$SSD = \frac{\sum_{i=m}^{M}\sum_{j=n}^{N}\sum_{\{R,G,B\}}[(I_1 - I_2)]^2_{(i,j)}}{(N-n+1)\times(M-m+1)} \tag{3.1}$$

$$SAD = \frac{\sum_{i=m}^{M}\sum_{j=n}^{N}\sum_{\{R,G,B\}} |(I_1 - I_2)|_{(i,j)}}{(N-n+1)\times(M-m+1)} \tag{3.2}$$

$$NCC = \frac{\sum_{i=m}^{M}\sum_{j=n}^{N}\sum_{\{R,G,B\}} I_{1(i,j)} \times I_{2(i,j)}}{\sqrt{\sum_{i=m}^{M}\sum_{j=n}^{N} I_1^{\,2}{}_{(i,j)} \times \sum_{i=m}^{M}\sum_{j=n}^{N} I_2^{\,2}{}_{(i,j)}}} \tag{3.3}$$

$$ZNCC = \frac{\sum_{i=m}^{M}\sum_{j=n}^{N}(\mathrm{I}_{1(i,j)} - \overline{I_1}).(\mathrm{I}_{2(\mathrm{i,j})} - \overline{I_2})}{\sqrt{\sum_{i=m}^{M}\sum_{j=n}^{N}(I_{1(\mathrm{i,j})} - \overline{I_1})^2 . \sum_{i=m}^{M}\sum_{j=n}^{N}(I_{2(\mathrm{i},j)} - \overline{I_2})^2}} \tag{3.4}$$

In these equations, I_1 and I_2 are the intensity of pixels at coordinates (i, j) of images 1 and 2 in the overlapped region, respectively; *SAD* is the sum of difference between the pixel values of images 1 and 2 for each color channel (R, G, and B).

However, the standard *SAD* function has poor performance because image data are attributable to radiometric distortion and noise[34]. For that the authors propose a modified *SAD* function as follows: The numerator of Eq. (3.2) is divided by the area of the overlapping region (the total number of pixels) to normalize the overlapping region in each measurement. Furthermore, (*m*, *n*) and (*M*, *N*) are as the lower left and upper right coordinates (pixel) of the overlapped region of the image pairs, respectively. In this function, the higher similarity of the overlapped region of two images yields the smaller score of *SAD*.

Conversely, *NCC*, and *ZNCC* are determined from the correlation between the pixel intensity values in the overlapped region. The larger value of them yields the higher similarity. These measure is robust than distance metrics because they are invariant to linear brightness and contrast variations. However, they have more complex calculations of division, multiplication and square root. Therefore, their computation time is more than *SAD*, *SSD*. Advantage over *NCC*, *ZNCC* is immune to intensity distortion. But it is computationally more expensive than *NCC*.

These similarity metrics have several advantages[35]. These functions are relatively simple to use in finding the appropriate matching point. Moreover, they provide dense

matching for every image pairs, thus they can stitch directly for all input dataset with reasonable accuracy without pre-processing and post-processing to get the features. However, the traditional similarity metrics are affected by artifacts such as non-uniformed brightness, periodic structures, featureless, and noises. These factors result in the image-matching error. Therefore, in some cases, the global minimum cost value of the similarity metric doesn't yield well corresponding to the ground truth. Otherwise, the local minimum cost is coincident with the G-T shown in **Fig.3.4**. The authors consider to the local minimum cost. Here the authors introduce a metric to improve the accuracy of IML, as described below:

(2) Curvature metric with full search method

The conventional similarity metrics only exploited the information of the matching point of the pixel being processed without considering the information of neighbour pixels. Therefore, the results of similarity metrics frequently cause to many error ratio. The authors propose a direct curvature metric method based on density gradient of the neighbour pixels on full search area as the following equations:

$$CUR_{(k,l)}{}^{4} = \begin{pmatrix} 0 & 1 & 0 \\ 1 & -4 & 1 \\ 0 & 1 & 0 \end{pmatrix} \times \begin{pmatrix} & C(k-\gamma,l) & \\ C(k,l-\beta) & C(k,l) & C(k,l+\beta) \\ & C(k+\gamma,l) & \end{pmatrix} \tag{3.5}$$

$$CUR_{(k,l)}{}^{8} = \begin{pmatrix} 1 & 1 & 1 \\ 1 & -8 & 1 \\ 1 & 1 & 1 \end{pmatrix} \times \begin{pmatrix} C(k-\beta,l-\gamma) & C(k-\beta,l) & C(k-\beta,l+\gamma) \\ C(k-\beta,l) & C(k,l) & C(k+\beta,l) \\ C(k+\beta,l-\gamma) & C(k+l,l) & C(k+\beta,l+\gamma) \end{pmatrix} \tag{3.6}$$

$$CNP_{(k,l)}{}^{4} = \frac{1}{5}\sum \begin{pmatrix} & CUR^{4}{}_{(k-1,l)} & \\ CUR^{4}{}_{(k,l-1)} & CUR^{4}{}_{(k,l)} & CUR^{4}{}_{(k,l+1)} \\ & CUR^{4}{}_{(k+1,l)} & \end{pmatrix} \tag{3.7}$$

$$CNP_{(k,l)}{}^{8} = \frac{1}{9}\sum \begin{pmatrix} CUR_{(k-1,l-1)} & CUR_{(k-1,l)} & CUR_{(k-1,l+1)} \\ CUR_{(k-1,l)} & CUR_{(k,l)} & CUR_{(k+1,l)} \\ CUR_{(k+1,l-1} & CUR(k+1,l) & CUR_{(k+1,l+\gamma)} \end{pmatrix} \tag{3.8}$$

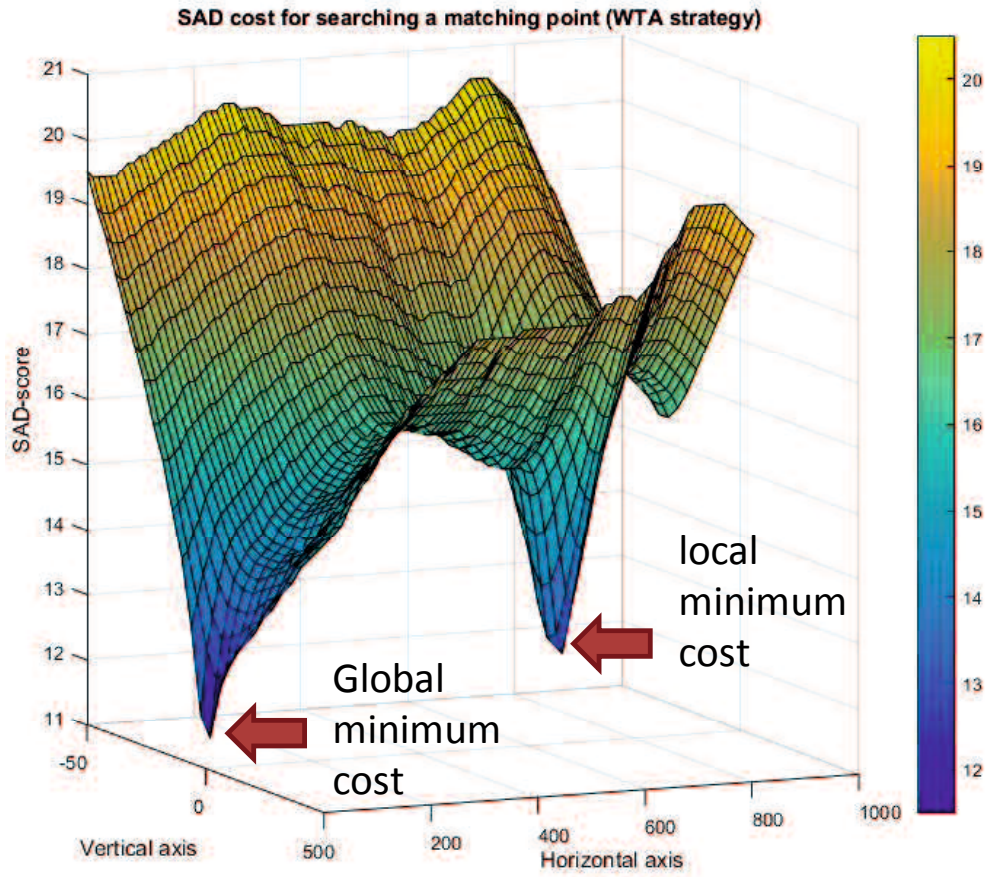

Fig.3.4 Cost space of *SAD* metric for a (31-312) pair in camera V1.

where $C_{(k,l)}$ is a cost value of the centre pixel using cost functions ; (β,γ) is the skipped pixel number or a size of search window; $CUR^{4}_{(k,l)}$ and $CUR^{8}_{(k,l)}$ are the curvature metric value refer to the 4-connected and 8-connected neighborhood pixels at the (k,l) coordinates, respectively; $CNP^{4}_{(k,l)}$ and $CNP^{8}_{(k,l)}$ are the average curvature values between the centre pixel and neighbor pixels refer to the 4-connected and 8-connected neighborhood pixels at the (k,l) coordinates, respectively. The larger *CUR* and *CNP* value mean higher matching possibility.

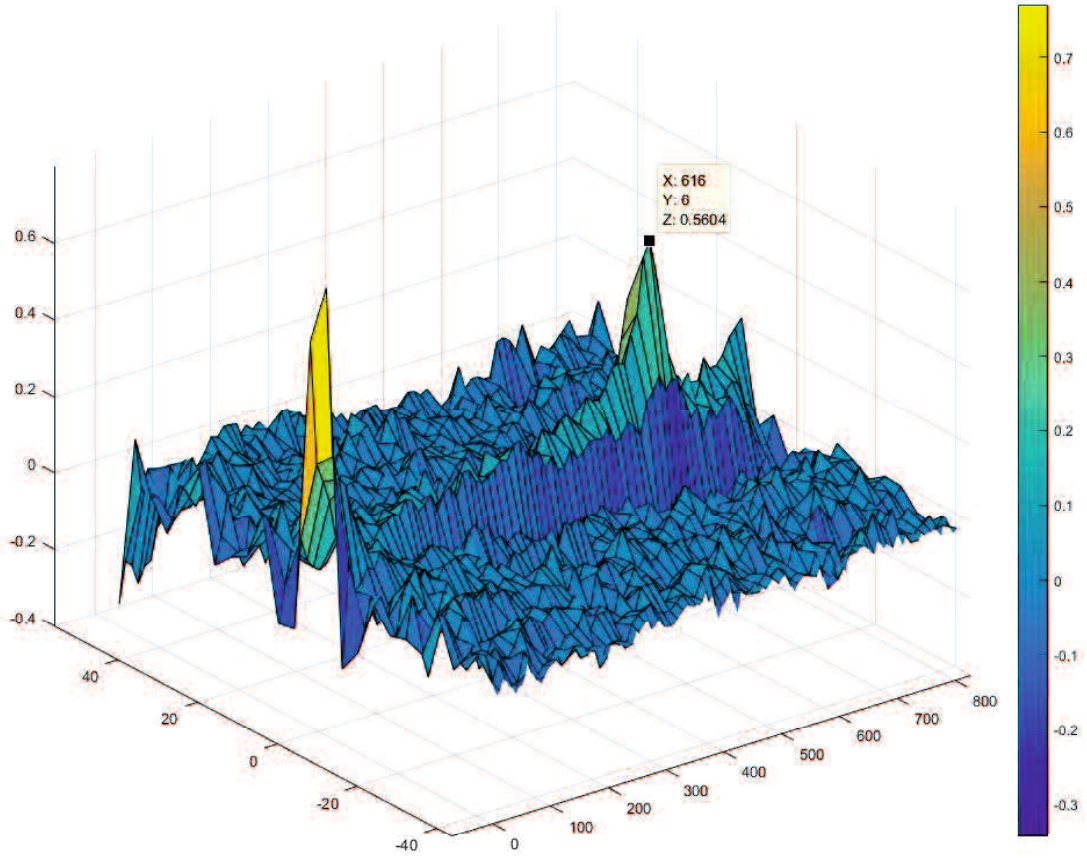

Fig.3.5 The correct matching point using direct curvature metric in the cost space.

In most of image matching cases, the curvature metric yields the correct image matching point result shown in **Fig.3.5**. However, in some special cases, the direct CUR is also affected by the outliers shown in the following **Fig.3.6**. Therefore, to eliminate the outliers, the search-strip method is adopted.

(3) Curvature metric with search strip method

To overcome these image-matching errors, the authors propose the search strip method and a metric including three steps. Firstly, candidate matching points are determined by the similarity metrics in each search strip. For uniformity with *NCC*, the cost value of the *SAD* function is converted to the negative value shown in the Eq. (3.5) because the cost values of *SAD* and *NCC* are opposite:

$$P_{(i)} = \{P_1, P_2, ..., P_N\} = Max \begin{bmatrix} -C^{SAD}{}_{(k,l)} \\ C^{NCC}{}_{(k,l)} \end{bmatrix} \tag{3.9}$$

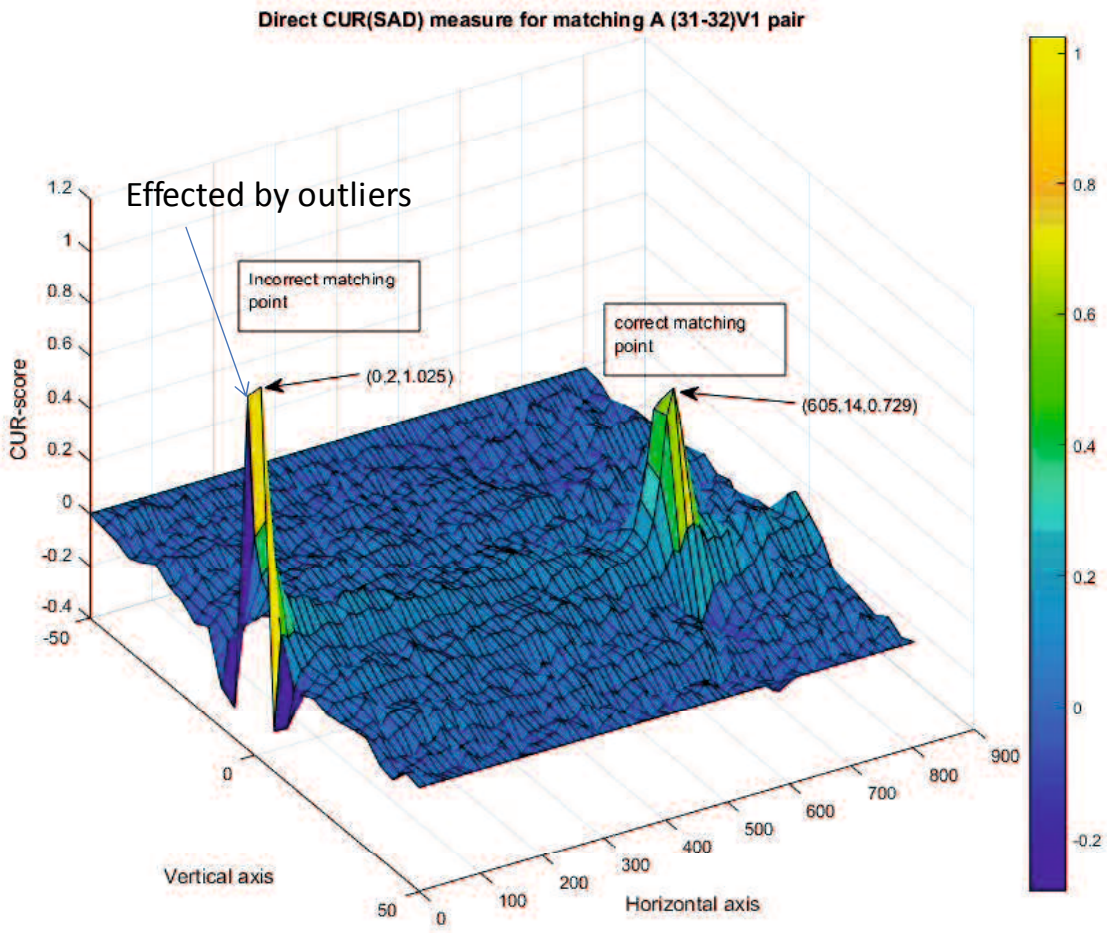

Fig.3.6 The incorrect matching point using direct curvature metric in the cost space.

where $P_{(i)}$ is the cost value of the i^{th} candidate matching point at the (k, l) coordinates in the i^{th} search strip; N is the total number of the candidate matching points in the search area; $C^{SAD}_{(k,l)}$ and $C^{NCC}_{(k,\,l)}$ are the cost value given by Eqs. (2) and (3), respectively.

The size of each search strip is (11x100) pixels, as shown in **Fig.3.7**. Each strip has a represented candidate of the image-matching location. The search point is skipped to 11 and 4 pixels via the horizontal and vertical directions, respectively, in the search strip and in the overlapped region.

Second, the set of these points $\{P_i\}$ obtained from the first step forms a cost curve. The conventional similarity metrics measure the cost value of the pixel being processed as follows:

$$MSM = \mathrm{Max}\left\{P_i\right\}, i \in [1, N] \tag{3.10}$$

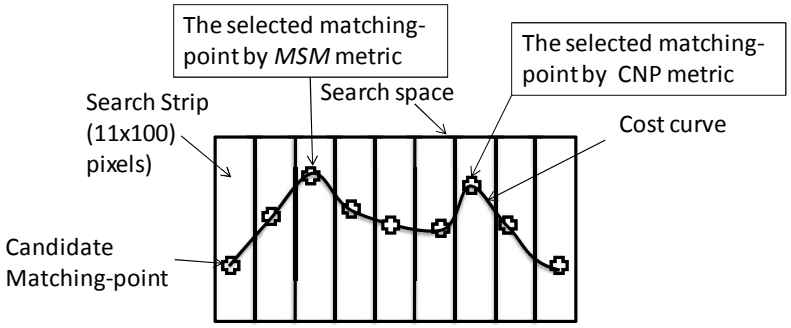

Fig.3.7 The search strip for extracting the candidate matching-points.

where *MSM* is the Maximum value of the Similarity Measurement for all of the candidate matching points in the full search space.

The curvature of the cost curve is computed, as shown in Eq. (3.11). Finally, the *CNP* metric is calculated, as shown in Eq. (3.12).

$$CUR_{(t)} = -2P_{(t)} + P_{(t-1)} + P_{(t+1)} \tag{3.11}$$

$$CNP_{ti} = \frac{CUR_{(t_i-1)} + CUR_{(t_i)} + CUR_{(t_i+1)}}{3} \tag{3.12}$$

In Eq. (3.11), $P_{(t\text{-}1)}$ and $P_{(t+1)}$ are the cost values to the left and right of the candidate matching point being processed in the t^{th} strip. If one of t-1 and t+1 positions is out of the search range, it is replaced with the nearest valid one. $CUR_{(ti)}$ is the curvature of the cost curve at the (ti,l) coordinates.

The *CUR* metric shows the confidence of a match because of the rapid cost change near the position having the maximum cost[36]. The larger *CUR* means higher confidence. If the curvature of the cost curve at the pixel being processed is small, then the image-matching location will not be reliable due to the quite similar cost of three pixels. Therefore, the *CNP* metric checks the confidence of the candidate matching point by evaluating the curvature values of its neighbor candidates.

In Eq.(3.12) , CNP_{ti} is the average curvature value at the i^{th} candidate with respect to the two adjacent candidates. The higher *CNP* score means the more reliable matching location.

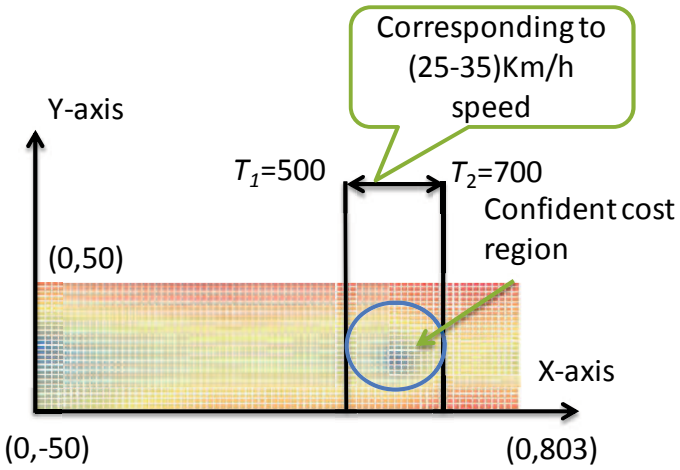

Fig.3.8 3D map of cost space in **Fig.3.4**.

3.3.2 Refinement technique

(1) Refinement technique based on dual threshold

The simple way to correct image matching errors from the results of the similarity metrics is based on the inspecting speed and the imaging device parameters. As shown in **Fig.3.8**, the vertical and horizontal axises are respect to the (k,l) of coordinates of image matching location. The smallest to highest cost value is corresponding to blue to yellow color. The matching point is chosen with respective to its *IMQ* between lower threshold (T_1) and upper threshold values (T_2) as the following equation:

$$T_{1,2} = \frac{v \mp \alpha}{u \times t} \tag{3.13}$$

In that, v is the initial setting speed of inspection car. It is equal to 30 Km/h. α is a parameter of the speed variance that is equal to 5 Km/h. Additionally, u is image resolution in unit mm/pixel, and t defined frame rate is a number of frames per second in the scanning tunnel progress. To avoid too strict for keeping constant inspection speed, authors allow the speed change of inspection vehicle to 30 ± 5km/h.

(2) Refinement technique based on median filter

After the proposed metrics are applied, some local bad matching points still remain. Further, the desired running speed of the inspection car is unchanged. Therefore, to smooth the *IMQ* graph, the median filter is adopted as the follows:

$$Q_i = \begin{cases} M_i \text{ if } |S_i - M_i| \le T \\ S_i \text{ otherwise} \end{cases} \tag{3.14}$$

Where,

$$S_i = med(M_{(i-k)},...M_i,...,M_{(i+k)})$$
$$\text{if } i<=k \text{ then } M_{(i-k)} = 0 \tag{3.15}$$

Here, Q_i is *IMQ* in unit pixels after refinement, and M_i is *IMQ* before refinement. *Si* is a median value obtained from Eq3.(11), and T_3 is a threshold value depending on the speed change of the inspection car. The size of the median filter is 2j+1 (where j is an integer).

3.4 EXPERIMENTAL WORK

3.4.1 Case study

The tunnel inspected in this experiment was an actual single-core circular tube in Yamaguchi Prefecture, Japan with length of 230 m, width of 10.25m, and height of 4.7m. The video digital cameras were SONY HDR-CX630V, with LED light 600(lm/m^2) and camera angle of view between 5^0- 6^0. The distance between the cameras and the tunnel wall was 3m. The dataset acquired by each camera consisted of 1,558 images with a resolution of 1920 × 1080 pixels for each picture. A photographic laser distance meter was used to maintain a constant distance between the tunnel lining and the inspection car to ensure a constant resolution. The speed of the inspection car was maintained at 30± 5 km/h corresponding to the desired image motion quantity from 500 to 700 pixels.

Further, a prototype software written in C++ was developed to implement the full image stitching algorithm. The search range was set to large to ensure the search result of matching point objectively as follows:

$$0 \le k \le 810$$
$$-50 \le l \le 50 \tag{3.16}$$

The search range via the horizontal axis designed from [0 810] pixels is corresponded to the inspection car speed from [0 40] km/h with the frame rate and resolution of the captured images shown in **Table.3.1**.

Table.3.1 Specifications of the camera system.

Items	Setting value
Image Resolution	1920×1080 (pixels)
Speed (x)	30 Km/h
Frame rate (y)	60fps
Number of Cameras	6
Illuminators	3
Resolution (z)	0.231 mm/pixel
Estimated *IMQ*	600 pixels

The search range in [-50 50] via the vertical axis was on account of the vibration of the inspection vehicle. The parameters of the refinement step were chosen as follows: size of the median filter was 100, and the threshold value was 50. The purpose of the median filter application was to reduce local errors when comparing neighbor *IMQ*s.

3.4.2 Image motion quantity (*IMQ*) results

Figures 3.9 shows the *IMQ* results of the imaging data in camera V2 using *MSM*. The horizontal axis is the number of consecutive images before and after matches, and the vertical axis presents the *IMQ* of two subsequent images. **Figures 3.9 (a)** presents the *IMQ* in the longitudinal direction of the tunnel called IMQ_x, and **Fig.3.9 (b)** shows the *IMQ* in the circumferential direction of the tunnel denoted IMQ_y. As can be seen in **Fig.3.9 (a)**, the IMQ_x is distributed at two critical positions on the graph. There are positions close to 0 and 600 pixels. Some local locations have IMQ_x over 700 pixels, and some other locations have IMQ_x between 0 and 500 pixels. Therefore, it is reasonable to estimate the first matching point around 600 pixels. To extend the reliable image-matching range, the authors define the accuracy of IMQ_x based on the parameters of the imaging system shown in **Table.3. 1**. As a result, the IMQ_x between the lower threshold value (500 pixels) and the upper threshold value (700 pixels) is considered as the correct-matching point.

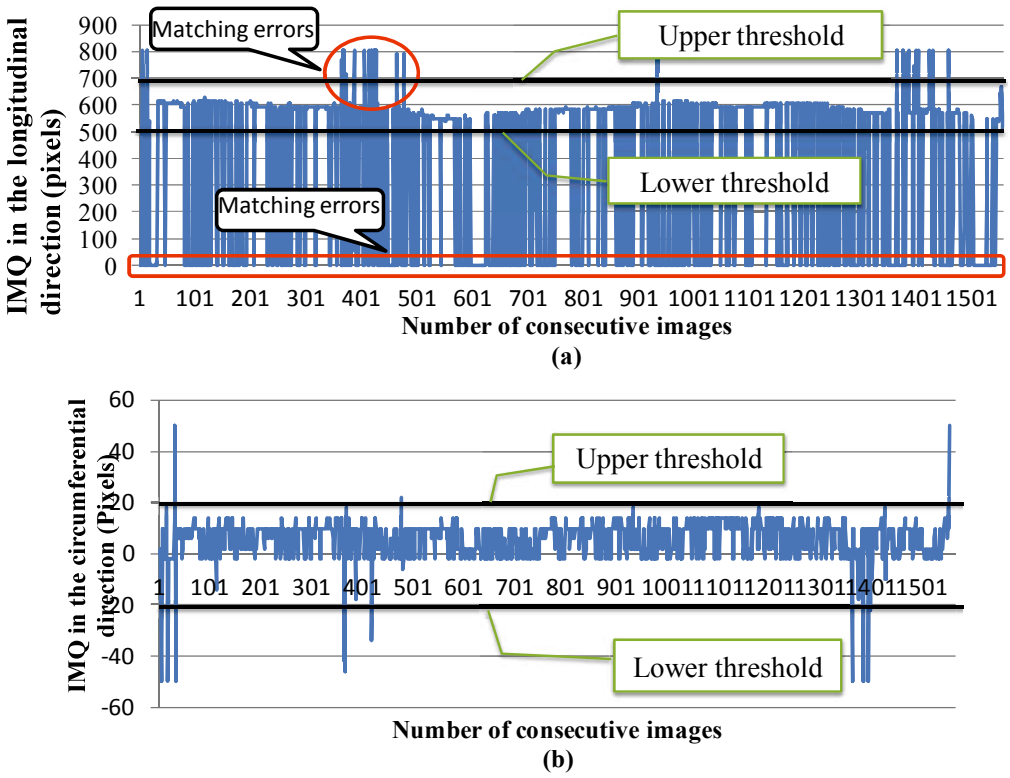

Fig.3.9 The results of the initial *IMQ* using *MSM* metric.

Accordingly the error rate is calculated by dividing the number of the image-matching errors by the total of the input images. The error rate of the IMQ_x using the *MSM* metric for all images in camera V2 is about 45.38%. In that, the error rate above the upper threshold is about 1%, and the error rate below the lower threshold is 44.38% (see **Table.3. 2**).

From results of the **Table.3.2**, the average matching errors of *SAD*, *SSD*, *NCC*, and *ZNCC* are respective around 44.2%, 62.7%, 31.6% and 29.42%. Those locations have the *IMQ* below 500 pixels and above 700 pixels. Those locations where the *IMQ* has below 500 pixels result from lacking information variance of the tunnel wall. Additionally, those locations where *IMQ* has over 700 pixels are out of search range.

Comparing among the four methods, the error ratios of *SSD*, *NCC*, and *ZNCC* are almost same. The *ZNCC* method is a little better than the others. However, its running time is the longest of the others with 130.33 minutes, around time cost double.

The *SAD* method gets the best of time cost, but the worst of accuracy image stitching in this case. The *SSD* method results in higher accuracy than *NCC* and *SAD* methods with average time cost is 65.33 minutes. This time is faster than the one of

Table.3.2 The results of *IMQ* error rate and running time of six cameras before correction technique.

Camera	*SAD*		*SSD*		*NCC*		*ZNCC*	
	error rate	running time	error rate	running time	error rate	running time	error rate	running time
V1	63.50%	62	40.99%	65	42.59%	78	39.28%	88
V2	45.38%	60	32.39%	63	29.63%	77	27.45%	139
V3	46.47%	62	37.27%	66	32.84%	82	29.97%	140
V4	33.18%	64	20.78%	68	20.85%	83	18.99%	138
V5	39.00%	64	23.48%	67	21.55%	83	19.12%	138
V6	37.66%	64	41.23%	63	41.94%	82	41.71%	139
Average	44.20%	62.67	32.69%	65.33	31.57%	80.83	29.42%	130.33

NCC matching cost function but slower than the running time of *SAD* matching cost function. *SAD* metric is too sensitive with noise or outlier than *SSD* metric. As shown in **Fig.3.10**, the result of the *SAD* metric chooses the location 1 to match. The location 1 is an example of the overlapped region of two images. In contrast, the result of the *SSD* metric chooses the location 2 to match. The subtraction values of the blocks in the overlapped region at the location 2 have a less difference than the ones at the location 1.

As shown in the IMQ_x graph in **Fig.3.11 (a)** using the *CNP* metric, most of IMQ_x distribute around 600 pixels. The error rate is only 0.26%. It is demonstrated that the use of *CNP* metric improves the accuracy of IML significantly.

Moreover, the authors define the permitted accuracy of the IMQ_y to be ± 20 pixels (± 4.6 mm). This accuracy is relatively high due to vibration of the inspection car. In effect, Meanwhile, **Fig.3.11 (b)** reflects that the IMQ_y resides in the reliable range and its fluctuation is about -5 pixels. From the results of the obtained IMQ_x and IMQ_y, it can be concluded that the *CNP* metric gains the higher accuracy than that of the MSM metric. Moreover, the fluctuation of IMQ_y shown in **Fig.s.3.9 (b)** and **3.11 (b)** does not have influence on the quality of image stitching.

To demonstrate the effectiveness of the *CNP* metric, **Fig.3.12** presents the relationship between IMQ_x and score deviation value of the *MSM* and *CNP* metrics using SAD cost function for four image-matching cases which correspond to four original pairs shown in **Fig.3.13**. **Figs.3.12 (a)**, **(b)**, and **(c)** show three cases of the inappropriate matches resulting from the *MSM* metric. However, the results of the *CNP* metric obtain all correct matching positions.

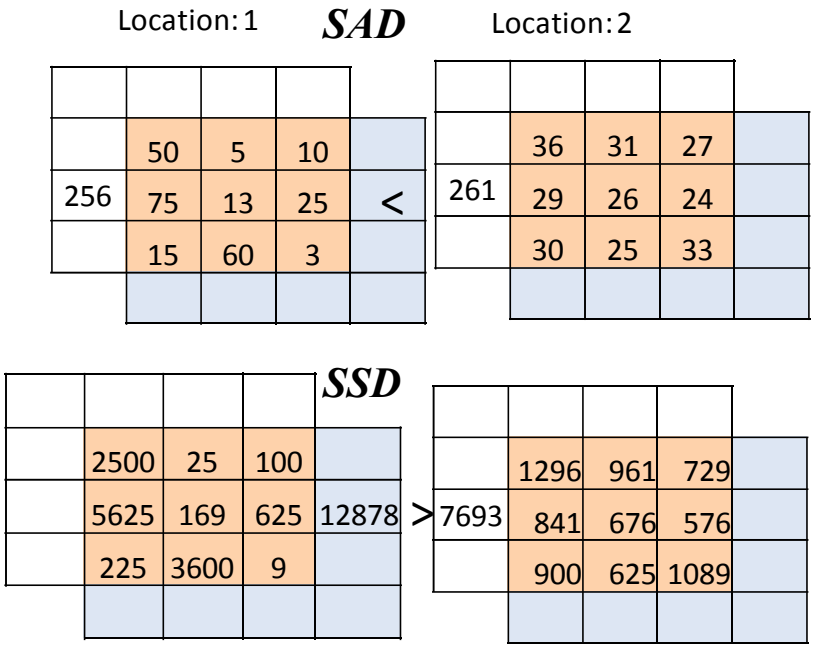

Fig.3.10 Comparison of similarity measurement between *SAD* and *SSD*.

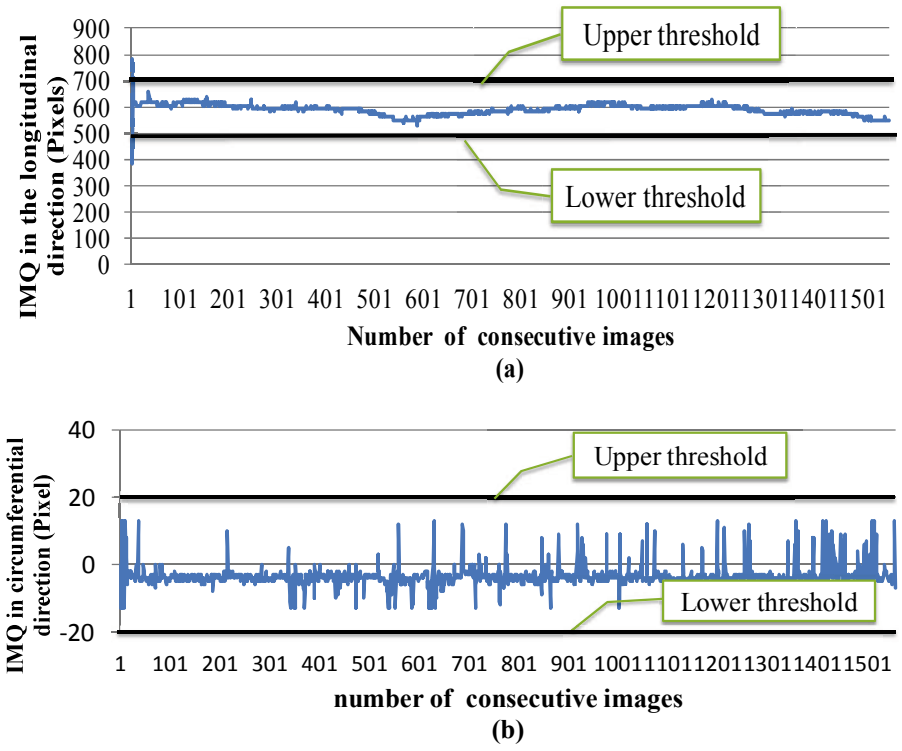

Fig.3.11 The results of *CNP* metric using *SAD*.

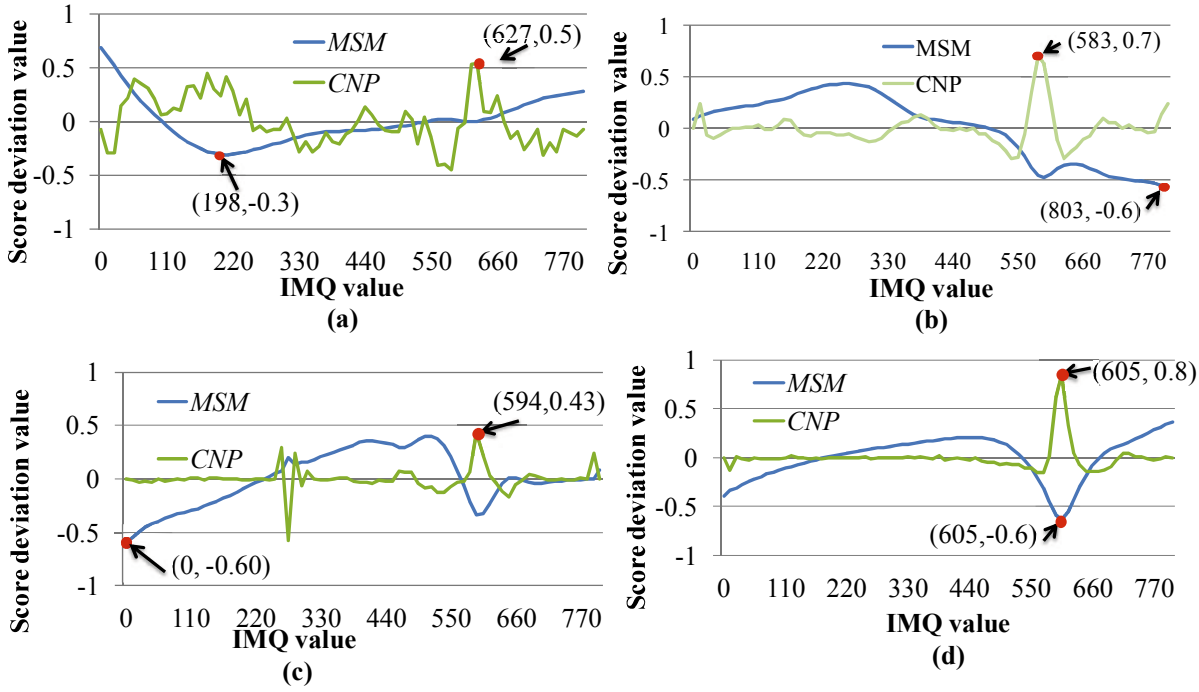

Fig.3.12 Test of matching points on the cost curve using *MSM* and *CNP* metrics.

For detailed explanations, in all of **Fig.3.12**, the horizontal axis presents the IMQ_x, and the vertical axis shows the score deviation value defined by the following equation:

$$\sigma_i = \frac{S_i - S_{avg}}{S_{\max} - S_{\min}} \tag{3.17}$$

where σ_i and S_i are the i^{th} score-deviation value and the i^{th} score for a measurement of similarity as well as curvature; and S_{avg}, $S_{\max}$, and $S_{\min}$ are average, maximum, and minimum scores of the metrics in the search range for each image pair, respectively.

In fact, **Fig.3.12 (a)** shows a case of a bad match at coordinates (198, -0.3) using the *MSM* metric. This case occurs due to featureless and non-uniform lighting contribution on frames 311 and 312 shown in **Fig.3.13 (a)**. The matching point location of *CNP* metric is at the (627, 0.5) coordinates. **Figure 3.12 (b)** shows an error of the *MSM* metric with the matching point at the (803,-0.7) coordinates. It tends to be out of the search range. This case searches matching point of a pair of frames 524 and 525 shown in **Fig.3.13 (b)**. Simultaneously, the matching point of *CNP* metric is at the (583, 0.7) coordinates. This point is a reliable matching point.

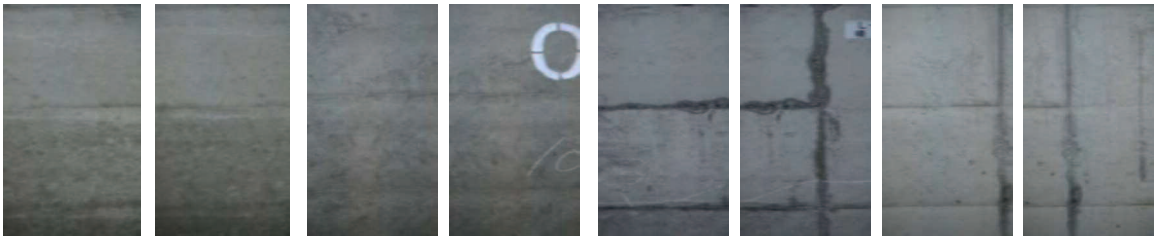

Frames 311and 312 Frames 524 and 525 Frames 216 and 217 Frames 265 and 266

(a) **(b)** **(c)** **(d)**

Fig.3.13 Some represented pairs of input frames.

In addition**, Fig.3.12 (c)** shows a common error of matching point at the (0,-0.6) coordinates using the *MSM* metric. This case occurs due to the influence of the featureless and the periodic structure in the pair of frames 216-217 shown in **Fig.3.13 (c)**. Meanwhile, the location of the matching point of the *CNP* metric is at the (594, 0.43) coordinates. In **Fig.3.12 (d),** both *MSM* and *CNP* metrics expose the desired matches of the pair of frames 265 and 266 shown in **Fig.3.13 (d)**.

Moreover, **Fig.3.14 s**hows the graphs of IMQ_x using the *CNP* metric with *SAD* and *NCC* cost functions after refinement, called *CNP*(*SAD*) and *CNP*(*NCC*), respectively. By observation, the graph of IMQ_x using *CNP*(*SAD*) metric shown in **Fig.3.14(b)** is smoother than the one of *CNP*(*NCC*) metric shown in **Fig.3.14 (a)**. For this reason, the *CNP*(*SAD*) metric gets the sharper curvature of the pixel being process compared with the neighbour pixels of *CNP*(*NCC*) metric. In effect, the error rate of *CNP*(*NCC*) and *CNP(SAD)* metrics are completely eliminated after refinement technique is applied, (see **Table.3.5**).

3.4.3 Accumulative *IMQ* results

This subsection shows the accumulative *IMQ* of six cameras in the region 1 (R1) of the video acquisition device. The accumulative *IMQ* results of R2 to R6 are not presented due to space limitation.

Figures 3.15, **3.16** and **3.17** show the accumulative *IMQ* value for each camera. In these figures, the horizontal axis is the order numbers of cameras V1 to V6. The vertical axis is the accumulative *IMQ* in the tunnel longitudinal direction.

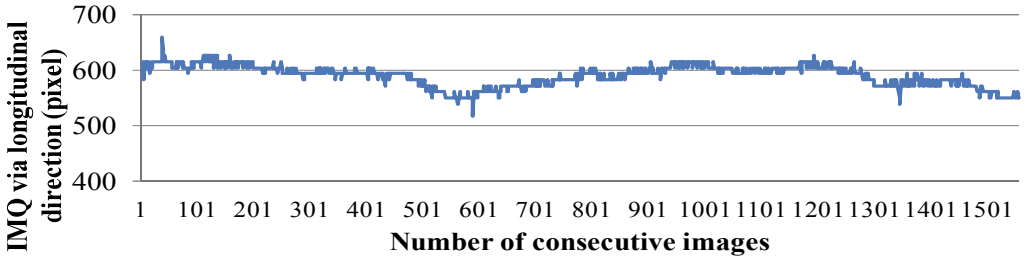

(a) The result of *IMQ* using *CNP*(*NCC*).

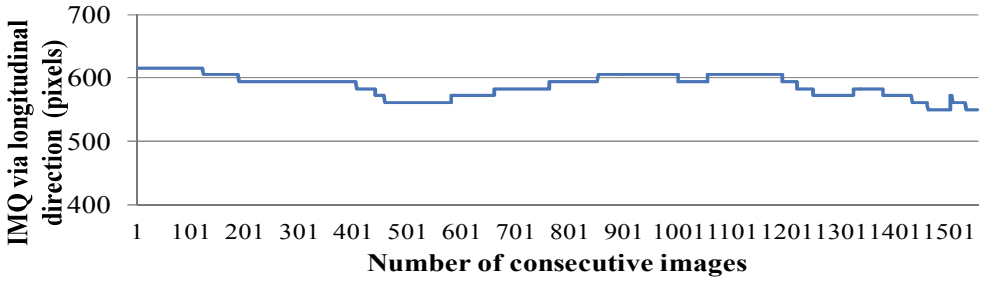

(b) The result of *IMQ* using *CNP*(*SAD*).

Fig.3.14 Comparison of *IMQ* of the *CNP* metric with two different cost functions after refinement.

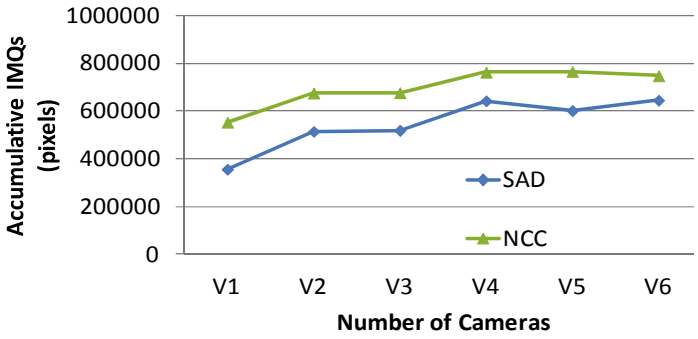

Fig.3.15 The results of accumulative *IMQ*s using *MSM*.

As shown in **Fig.3.15**, in the comparison of accumulative *IMQ* (a.*IMQ*) of the *SAD* metric and *NCC* metric, the *NCC* metric is better than the *SAD* metric for all cameras. Although the *SAD* metric is normalized by the total number of pixels in the overlapped region it is sensitive to the linear lighting change. Whereas the *NCC* metric is a normalized metric, it is invariant to the linear change of the brightness. **Figures 3.16** and **3.17** show the results of the a.*IMQ* of *CUR* and *CNP* metrics using *SAD* and *NCC* cost functions after the refinement is applied. Their a.*IMQ* difference of them is small. The maximum difference of the a.*IMQ* is 9000 pixels belonging to camera V4, as shown in **Fig.3.16**.

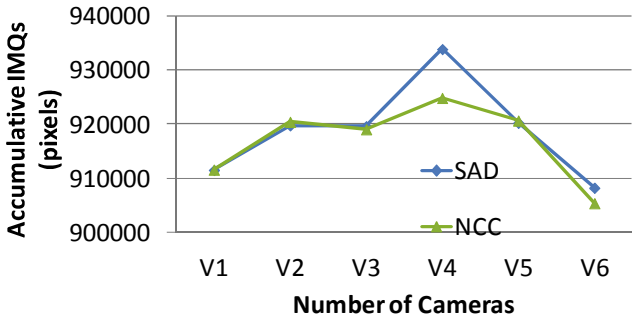

Fig.3.16 The results of accumulative *IMQ*s using *CUR*.

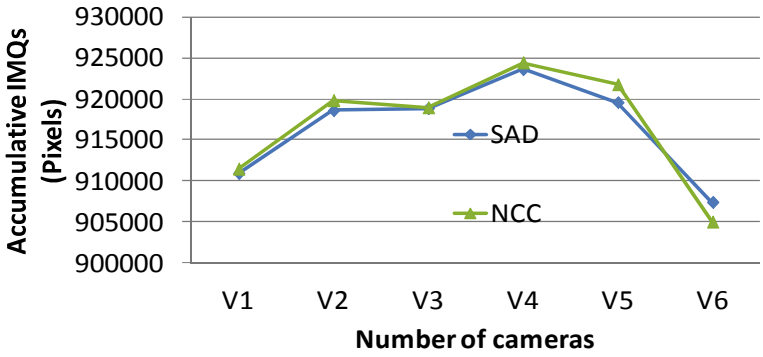

Fig.3.17 The results of accumulative *IMQ*s using *CNP*.

It is demonstrated that the effectiveness of the refinement technique leading to the stability of the a.*IMQ*.

Comparing the *MSM*, *CUR*, and *CNP* metrics, the results of a.*IMQ* using *MSM* are the lowest with the maximum a.*IMQ* of about 800.000 pixels in all cameras; whereas the maximum results of the a.*IMQ* using *CUR* and *CNP* metrics are 933861 and 923582 pixels respectively.

3.5 PERFORMANCE EVALUATION

There are two criteria to evaluate the effectiveness of the proposed method. Those are (a) target *IMQ* based on the parameters of the video acquisition system and (b) ground-truth image matching.

Table.3.3 Parameter values of the imaging system.

Parameters	Values
Speed of shooting vehicle car (u)	[25-35] km/h
Frame rate (v)	60 frames/second
Resolution (r)	0.231 mm/pixel
Estimated value of image motion quantity	[500 700] pixels

3.5.1 Evaluation of image matching error based on the parameters of the video acquisition system

The dataset used to test the image-matching error (*IME*) consists of six cameras in Region 1. The total number of images for evaluation is 9,348 images. The *IMQ* result of the *MSM* and *CNP* metrics are compared to the target *IMQ* based on the following equation:

$$E = \frac{u}{v \times r} \tag{3.18}$$

where u, v, and r are the parameters of the imaging system the values of which are given in **Table.3.3**; and E is the target *IMQ*.

The speed of the inspection car is set at about 30 km/h, with possible variation in the range 25 to 35 km/h. From the Eq 3.14, this speed variance is equivalent to the reliable range of E of [500 700] pixel. The error rate is computed using the following equation :

$$\begin{aligned} AME &= \frac{1}{N}\sum_{i=1}^{N} IME_i \times 100\% \\ IME_i &= \begin{cases} 0 \text{ if } \mathrm{IMQ}_i \in [500\ 700] \\ 1\ Otherwise \end{cases} \end{aligned} \tag{3.19}$$

where N is the number of images in each camera; IME_i is i^{th} image matching error; IMQ_i is image motion quantity at i^{th} measurement; and *AME* is the accumulative error rate for each camera. This equation indicates that an *IMQ* value is out of range [500 700] pixels considered as an *IME*.

Table.3.4 Criterion 1 based image matching error result (unit %) before refinement.

Cost function	Camera	**Proposed method**			**Previous methods** (*SSD*)	
		MSM	*CUR*	*CNP*	*FS*	*LS*
SAD	V1	63.48	0.77	0.45	41.3	1.9
	V2	45.38	0.77	0.26	32.7	2.7
	V3	46.47	1.67	0.26	37.8	7.2
	V4	33.18	1.99	0.83	21.5	2.1
	V5	39.00	1.60	0.52	23.7	3.2
	V6	37.66	5.80	0.77	40.2	3.6
NCC	V1	42.59	3.79	1.41	-	-
	V2	29.63	5.65	1.16	-	-
	V3	32.84	7.45	3.60	-	-
	V4	20.85	6.55	2.57	-	-
	V5	21.55	8.03	2.83	-	-
	V6	41.94	21.16	7.59	-	-

Table.3.5 Criterion 1 based image matching error results (unit %) after refinement.

Cost function	Camera	**Proposed method**			**Previous methods** (*SSD*)	
		MSM	*CUR*	*CNP*	*FS*	*LS*
SAD	V1	82.92	0	0	1.2	0
	V2	31.45	0	0	0.3	0
	V3	43.77	0	0	5.2	0
	V4	16.55	0	0	0.2	0
	V5	20.47	0	0	0.2	0
	V6	9.69	0	0	9.2	0
NCC	V1	24.96	0	0	-	-
	V2	5.26	0.19	0	-	-
	V3	4.30	0.39	0	-	-
	V4	1.92	0.26	0	-	-
	V5	3.08	0.19	0	-	-
	V6	3.98	0.71	0	-	-

As a result, **Table.3.4** reports the results of the *AME* based on the proposed method and our previous methods for six cameras before refinement. Among the cost functions, the *SAD* metric gets the worst accuracy with an average *AME* of 44.20%. Meanwhile, the average *AME*s of *NCC* and *SSD* metrics (in *FS* method) are 31.57 % and 32.87%, respectively.

Comparing the *CUR*, *CNP* and *LS* metrics, the average *AMEs* of six cameras using *CUR(SAD)* and *CNP*(*SAD*) metrics are 2.10% and 0.51%, respectively. The average *AME* of *CUR* and *CNP* using *NCC* cost are 8.77% and 3.19%. The average *AME* rate of

Table.3.6 Comparison results of the curvature metrics.

Camera	CUR^4	CNP^4	CUR^8	CNP^8	CUR^{strip}	CNP^{strip}
V1	1.09%	0.90%	0.96%	0.83%	0.77%	0.45%
V2	0.45%	0.39%	0.83%	0.39%	0.77%	0.26%
V3	0.71%	0.64%	2.12%	0.90%	1.67%	0.26%
V4	0.90%	0.90%	1.16%	0.96%	1.99%	0.83%
V5	0.45%	0.45%	0.77%	0.51%	1.60%	0.52%
V6	8.10%	7.52%	19.78%	4.50%	5.80%	0.77%
Average	1.95%	1.80%	4.27%	1.35%	2.10%	0.52%

the *LS* method is 3.45%. These results validated that the *CNP* metric is the best among the three. **Table.3.5** presents the *AME* results after applying the refinement. The error rates of all metrics decrease dramatically except for the result of the *MSM(SAD)* metric for camera V1. The reason is that the median values of the neighbor images of camera V1 result in the *AME* increase. Further, the *AMEs* of *CUR(SAD)*, *CNP*(*SAD),* and *CNP(NCC)* metrics eliminate the error completely while the *AME* of *CUR*(*NCC*) metric retains small errors. **Table.3.5** also shows that the *AME* of the *LS* method is eliminated completely but the *AME* in the *FS* method is still retained with an average *AME* of six cameras of 2.7%. It demonstrates that the proposed method has improved the accuracy of the image-matching locations significantly.

The **Table.3.6** shows comparison results of the proposed curvature metrics for six cameras before refinement is applied. As can be seen, all of *CUR* and *CNP* metric have error ratio very small. Comparing among the results of *CUR* metrics, CUR^4 is the highest accuracy with the average accuracy of six cameras of 1.95%. Otherwise, CNP^{strip} has the best results of the error ratio of 0.52% compared to the others.

3.5.2 Evaluation of image matching error based on the ground- truth (G-T)

To evaluate the accuracy of the proposed image matching algorithm, the authors create the G-T image matching using manual method to compare the results of the proposed method in unit pixels. Each camera contained 1,558 images, and each image

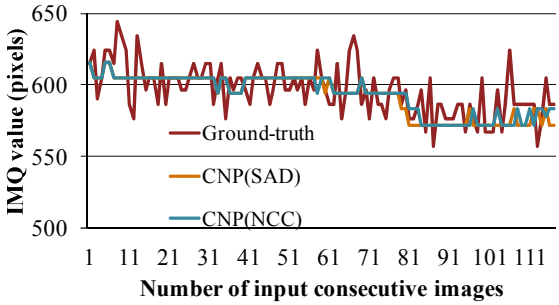

Fig.3.18 The *IMQ* results of G-T and proposed method (120 images).

Table.3.7 Criterion 2 based image matching error (unit %).

Cost function	Segments	*MSM*	*CUR* before refinement	*CNP* before refinement
SAD	V1-1	15	0	0
	V1-2	0	0	0
	V1-3	0	0	0
NCC	V1-1	8	0	0
	V1-2	0	0	0
	V1-3	0	0	0

had a resolution of 1080 × 1920 pixels. Because the six cameras provide a large number of images the authors did not test all images.

Therefore, from the original image data sets, three segmentations at the tunnel portal and in the middle of the tunnel are extracted from camera 1. The three segments of the camera V1 are denoted by V1-1, V1-2, and V1-3. Each segment has 40 images, and the total of three sections including 120 images are used as test samples.

$$AME = \frac{1}{N}\sum_{i=1}^{N} IME_i \times 100\%$$
$$IME_i = \begin{cases} 0 \text{ if } |\text{T-IMQ}|_i \le \varepsilon \\ 1 \ otherwise \end{cases} \tag{3.20}$$

where N, AME, IME, and IMQ are similar to the above-mentioned definition. T_i is a manual matching of the i^{th} G-T image in the vertical and horizontal directions; and ε is threshold value that is computed as ± 100 pixels equivalent to the permitted speed change which is ± 5 km/h (Eq.3. 18).

Table.3.7 presents the results of *AME* measurement defined in the Eq. (3.20). In the V1-1, *MSM*(*NCC*) metric has *AME* of 8%, and *MSM*(*SAD*) metric has AME of 15%. In ther segments, the *MSM* metric has zero error. Furthermore, using *CUR* and *CNP* metrics, the *AME* are eliminated completely.

The curve graphs in **Fig.3.18** show the comparison between the G-T image-matching and the image-matching results of *CNP*(*SAD*) and *CNP(NCC)* metrics. There is negligible difference between the graphs of the proposed metrics and the G-T. It can be concluded that both *CNP*(*SAD*) and *CNP*(*NCC*) metrics yield a high accuracy for the image matching process of the tunnel lining surface.

3.5.3 Evaluation of the length of tunnel based on accumulative *IMQ*

The actual tunnel length collected image data is 230 m on 0.231 mm/pixel resolution the perfect accumulative *IMQ*s will be around 1 million pixels. To evaluate the validation of the proposed method the accumulative *IMQ*s of six cameras need to be tested.

The average accumulative *IMQ* (Avg.*IMQ*) value of six cameras using the *MSM* and *CNP* metrics compared with the total number of pixels corresponded to the length of the entire tunnel. This difference is defined in the following equation:

$$\text{Diff} = \frac{|1{,}000{,}000 - \text{Avg.IMQ}|}{1{,}000{,}000} \times 100\% \tag{3.21}$$

The **Table.3.8** reflects that the largest Diff belongs to *MSM*(*SAD*) with 45.61%. However, the Diff of *CNP*(*SAD*) is 8.35%. The Diff of *MSM*(*NCC*) is 30.28% less than *MSM*(*SAD*). However, the Diff of *CNP*(*NCC*) is 8.31%. The experimental results express that *CNP* metric improves the accuracy of IMLs.

3.5.4 Evaluation of the computational time

To test the computational time for each camera with other image matching methods, the authors implement a parallel running program for six cameras in each region to get the image-matching information based on *MSM* and *CNP* metrics. **Table.3.9** reports the

Table.3.8 Comparison of the length of tunnel based on a.*IMQ*.

Cost function	*MSM*		*CNP*	
	Avg. *IMQ*	Diff	Avg. *IMQ*	Diff
SAD	543884	45.61%	916487	8.35%
NCC	697178	30.28%	916893	8.31%

Table.3.9 Average computational time for parallel running implementation for 6 cameras (unit: minute).

Proposed method			Previous methods		
Cost function	*MSM*	*CNP*	Cost function	*FS*	LS
SAD	62	2	*SSD*	90	4
NCC	83	4	-	-	-

computational time for running the image matching using the proposed method and the previous methods.

In the *MSM* method, the computational time of *SAD* cost function is shorter than the one of *NCC* cost function. The timing cost of the *CNP* metrics is 2 and 4 minutes after subtracting the time of the similarity measure of *SAD* and *NCC*, respectively. Comparing the computational time of *FS* and *LS* methods, the time of the proposed algorithm is the fastest. For this reason, the *FS* method searched all of points in the predefined area, and the *LS* method searched the matching point surrounding the initial estimated position (600 pixels). Meanwhile, the proposed search algorithm considers the curvature of cost curve at the nearest neighbour pixels and the pixel being processed, which have local maximum *MSM* value to find the best image-matching point. Therefore, the algorithm reduces the number of search points.

3.5.5 Creating panoramic images

Unfolded panoramas of tunnel lining are created by an image-stitching software based on the *IMQ* results of *CNP* metric. This software stitches consecutive images for

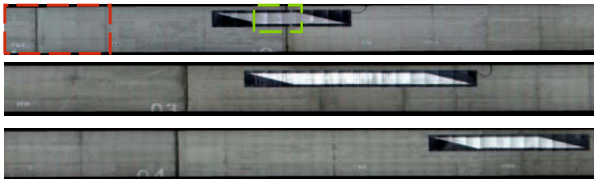

(a) The image stitching result of *MSM*(*SAD*).

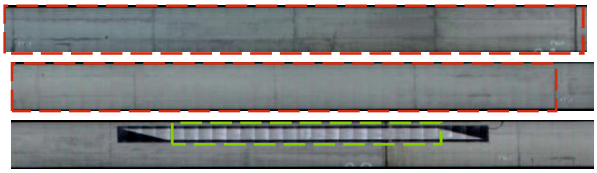

(b) The image stitching result of *CNP*(*SAD*).

Fig.3.19 The image stitching results of the first three of segments using *MSM* and *CNP* metrics with *SAD* cost for camera V2, respectively.

each camera via longitudinal direction of the tube. The panoramic pictures of each camera for the entire tunnel lining include 22 segments, and the length of each segment is 10.5 m excluding overlapped parts at the two ends of the next segment.

For visualized comparison between *MSM* and *CNP*, **Fig.3.19** shows the first three segments of the *MSM* and *CNP* metrics with *SAD* cost function. Using *MSM* metric to stitch image has many errors due to the featureless (red dash rectangle) and the periodic structures (green dash box) shown in **Fig.3.19 (a)**. These errors are rectified and respectively shown from segment 1 to 3 using the *CNP* metric shown in **Fig.3.19 (b).**

Figure 3.20 shows a representation of one part of each camera in the longitudinal direction of the tunnel. Each mosaic compressed at a scale of 1 per 32 has 45600x1920 pixels based on stitching 65 RGB (1080x1920) resolution images. **Figure 3.21** shows a represented result of the manual camera stitching via the circumferential direction. From this layout panorama with high resolution, inspectors can detect defects easily. For illustration, inspectors detect crack types (chalk lines) with predetermined maximum widths. That is an important purpose of producing the tunnel lining panorama.

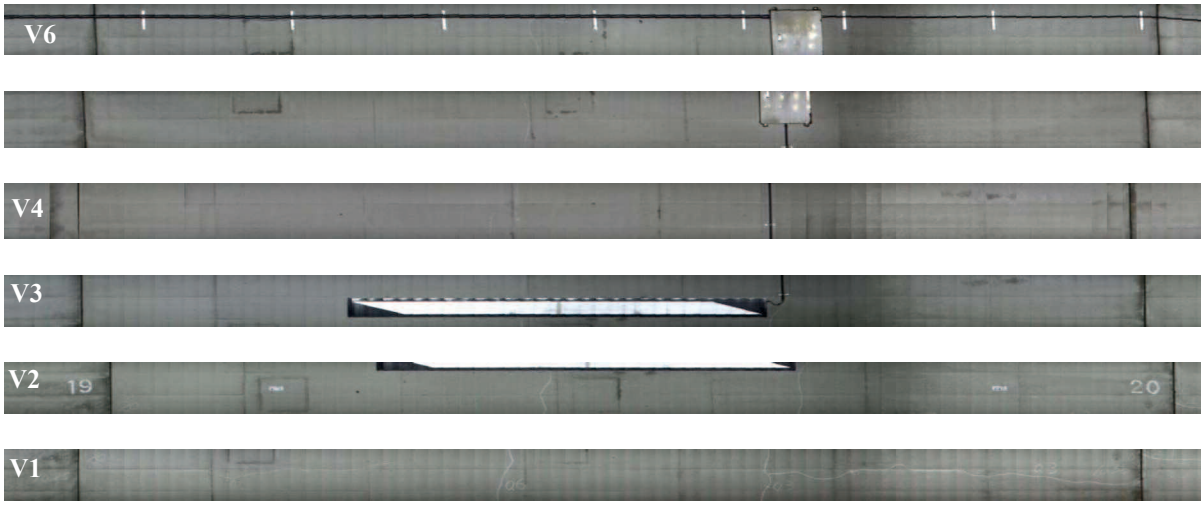

Fig.3.20 The represented results of consecutive image stitching for each camera in the longitudinal direction.

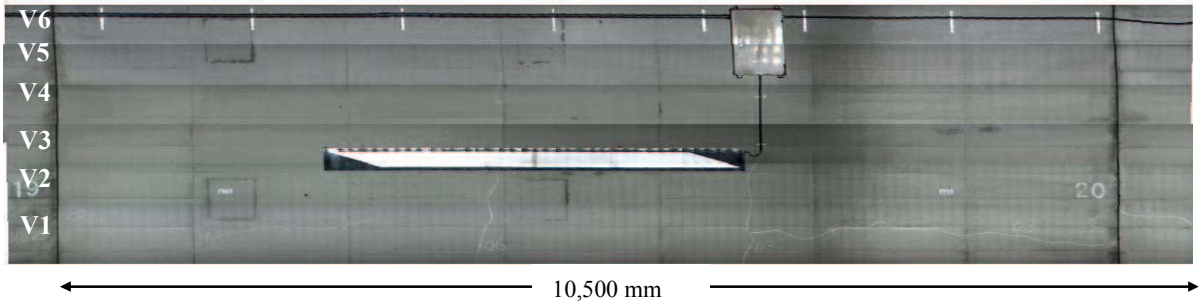

Fig.3.21 A represented result of camera stitching in the circumferential direction.

3.5.6 Evaluate of the working time for panorama generation sofware

The **Table.3.10** shows the comparison of working time for panorama generation between manual method and software. STEP1 sets up parameter environment such as the locations of input and output. STEP2 is image stitching in longitudinal direction. STEP3 determines the joint location of two consecutive segments. STEP4 creates the layout panorama.

The results demonstrated that the effectiveness of the panoramic stitching software. The working time is reduced to 93% compared to manual method while the quality of panorama generation is similar together shown in **Figs.3.22** and **3.23**.

Fig.3.22 The first segment generation by software.

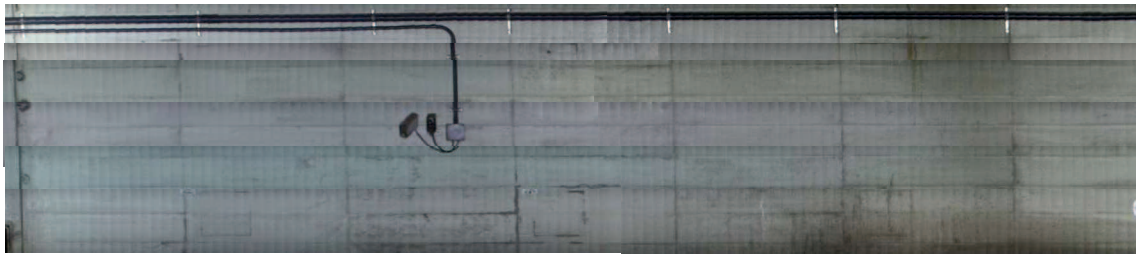

Fig.3.23 The first segment generation by manual.

3.6 CONCLUSIONS

Unlike the conventional metrics which only exploited the cost value of the pixel being processed, the proposed method extracted the candidate matching points based on the similarity metrics in each strip. Subsequently, the precise matching-point is selected based on the curvature value. The *MSM* metric considered the global maximum value of the similarity metric so that the results of the matching points had many errors due to the influence of the noises. The *CUR* metric focused on the candidates which had the local maximum values of the cost curve. So far, the *CNP* metric has tested the stability of the candidates based on the mean curvature value.

The main advantage of the proposed method was to eliminate the artifacts of the neighbor pixels surrounding the candidate matching point in each search strip before measuring the sharpness at the peaks of the cost curve. Therefore it improved the computational time and the matching accuracy compared to our previous studies. As a result of this study, a large number of the raw images of tunnel lining surface were matched automatically with high accuracy. The average accuracy of the *CNP(SAD)* metric was 99.49% before refinement without depending on the initial estimated *IMQ*,

Table.3.10 The comparison of working time for panorama generation between manual method and software.

Procedure of panorama generation	Manual (Minutes)	Soft (minutes)	Shortening rate
STEP1~STEP3	126 ※1	9	91%
STEP4 (Total : 22 segments)	22 ※2	1	95%
Total working time	148	10	93%

※1 : Estimated working time is 21 minutes for each camera
※2 : Estimated working time for each segment is 1 minute.

and the computational time of the *CNP(SAD)* was 2 minutes in order to match 1558 image pairs.

The main contributions of the paper are:

(1) Introducing an imaging equipment capable of scanning pictures of the entire tunnel. A total of six cameras, in which each camera produced 1558 images with 1290x1080-pixel resolutions, were mounted on a moving inspection car, which saved much time compared to other conventional imaging systems. (2) Proposing a new image-matching method based on the curvature of the cost curve at the matching-point candidate locations. Consequently, the application of median filter rectified the error of inappropriate *IMQ*. The parameters of the imaging system were used to estimate the error rate of the initialized image matching. The use of image stitching software enabled parallel running of six cameras, which significantly reduced computational time. The experimental results showed the high performance of the *CNP* metric compared with *MSM* and *CUR* metrics.

In addition, the image-matching results of the proposed method were improved significantly compared with those of our two previous methods and the G-T image matching. Moreover, the working time of the software for the layout panorama generation is improved significantly compared with the manual method.

In addition, this study found abnormalities in the tunnel lining surface without inspecting the shape of the tunnel. Therefore, the obtained images of the curved shape of the tunnel lining were manipulated to create a flat panorama for better visual inspection. The shaped 3D reconstruction of the tunnel-lining surface would be considered in the future research.

The paper observed several limitations. The proposed image-matching method relies exclusively on the color-pixel intensity. There is lack of feature descriptor-based methods such as SIFT and SURF. Moreover, the speed of the inspection car should be increased to eliminate disrupting traffic flow. These limitations will be addressed in future work.

CHAPTER 4

A STUDY ON SEMI-AUTOMATIC CONCRETE CRACKS DETECTION USING INTERACTIVE GENETIC ALGORITHM

Concrete surface crack detection is an important task of the inspection and diagnosis of concrete structures. This paper proposes a prototype software for semi-automatic crack detection from concrete surface images using an interactive genetic algorithm (iGA) and touch screen. The iGA is applied to optimize image processing parameters for each image with no knowledge of image processing techniques. Furthermore, the experimental results indicate that the proposed method has possibility of extracting crack with reasonable accuracy and working time.

4.1 INTRODUCTION

The number of deteriorated concrete structures has increased dramatically in many countries. Therefore, the management of existing concrete structures has become a major social concern worldwide. concrete cracks are important indicators reflecting the safety of infrastructure. To keep concrete structures at good condition under all circumstances, the inspection and maintenance are important.

Crack detection on concrete surface is the first task of the inspection and maintenance of concrete structures. The conventional methods for crack detection are generally implemented by the naked eye. Therefore inspection results are usually subjective, and it takes a long time.

Recently, there have been many researchers who have detected the cracks on concrete surface automatically[37), 38)]. Algorithms for crack detection generally involve a pre-processing step and a crack identification step[39)]. The pre-processing step applies image processing techniques to extract potential crack features, such as edges.

Miyamoto et al[11] computed the difference in intensity between each pixel and the average intensity of each row in an image matrix; a pixel that differs considerably from the average is deemed to belong to a crack. Fujita et al applied a line filter using the Hessian matrix and a threshold is applied to extract the crack regions. Ukai[14] developed a system to model cracks, which can be characterised by eight quantities, such as area and Ferets occupancy rate. Yamaguchi and Hashimoto[15] modelled cracks based on the percolation model, which is a physical model based on liquid permeation. Paar et al[16] proposed a crack detection algorithm based on the line tracing algorithm. The identification step usually applied crack modelling and/or pattern recognition techniques in order to determine if the extracted features belong to crack regions. Zhu and Brilakis[17] proposed an algorithm for detecting concrete columns based on texture using artificial neural networks. Liu et al[18] applied a Support Vector Machine classifier to classify if crack features appear in an image patch, which is pre-processed to extract potential crack features based on intensity. Abdelqader et al[19] apply a Principal Component Principles (PCA) algorithm, which can be used to reduce the dimensions of feature vectors based on eigenvalues, to extract cracks from concrete bridge decks.

The full automation of crack detection from digital images is difficult due to many factors such as the difference in the photography environment and concrete surface condition. Therefore, image processing parameters to detect the cracks on concrete surface have to be adjusted for each image. Moreover, it is hard for inspectors to adjust the parameters without knowledge of image processing techniques.

The main target of this study was to propose the prototype software for semi-automatic crack detection from concrete surface images using an interactive genetic algorithm (iGA) and touch screen. The iGA was applied to optimize image processing parameters for each image. The output of the software was a crack map that was compared to a benchmark image to verify reasonable accuracy and working time from a practical engineering point of view.

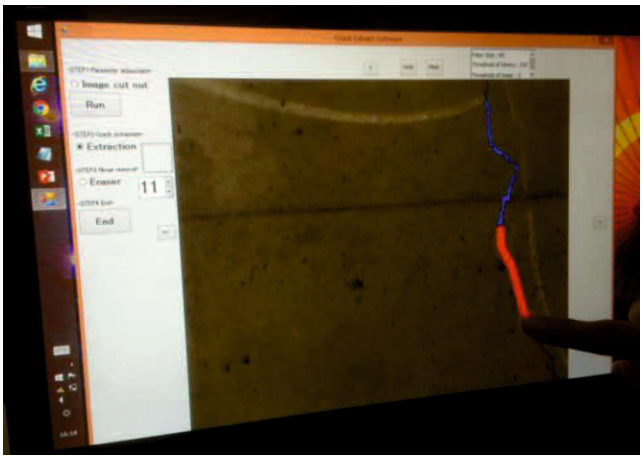

Fig.4.1 Crack extraction on the touch screen .

4.2 PROPOSED METHOD

4.2.1 Overview

Figure 4.1 shows how the cracks are extracted intuitively on the touch screen where the crack is extracted from a concrete surface image by tracing user's finger. In addition, **Fig.4.2** shows operation procedure of the proposed software. **Fig.4.3** shows sequential 7 steps of image processing technique in which three parameters are adjusted to find out optimal values. Those are size of median filter (fsize), threshold of binarization (binary), and threshold of linear degree (linear). In this paper, the prototype software was development based on image processing technique and the iGA.

4.2.2 Image processing technique

The algorithm for accurate crack detection has composed of three major process parts shown in **Fig.4.3**. The first part was image input part which included image input and grayscale image transformation. The second part was crack enhancement part which included the following preprocessing steps: median filter, subtraction, binarization. The final part was noise removal part, comprising two steps: labeling and linear degree determination. This image processing technique[40)] was presented in detail as follow:

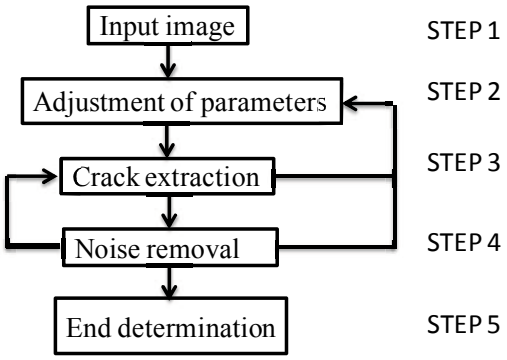

Fig.4.2 Operation procedure of the software.

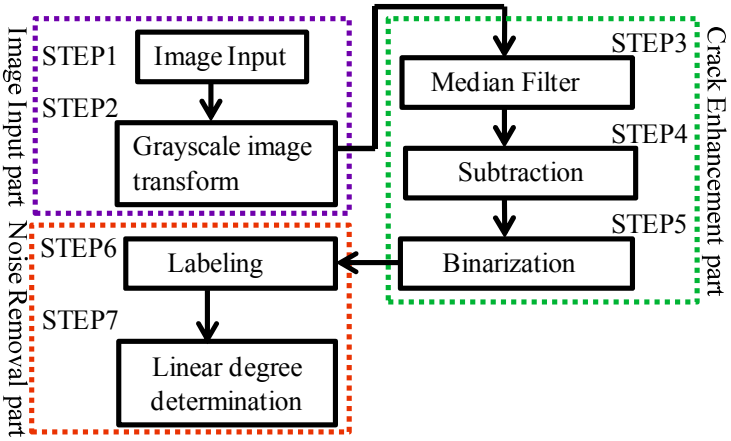

Fig.4.3 Image processing technique.

(1) Part1 (Image input part)

Inputting an actual concrete surface image which is captured by digital camera, it will be converted into a gray-scale image. The pixel values in the gray-scale image are formulated as the following equation:

$$Y = 0.2989 \times R + 0.5870 \times G + 0.1140 \times B \tag{4.1}$$

Where, Y is grayscale pixel value, R, G, and B are pixel values of the red, the green, and the blue, respectively.

(2) Part2 (Crack enhancement part)

Firstly, the above obtained gray scale image is blurred by the median filter. Secondly, it is processed with subtraction processing. The output result of this step is a

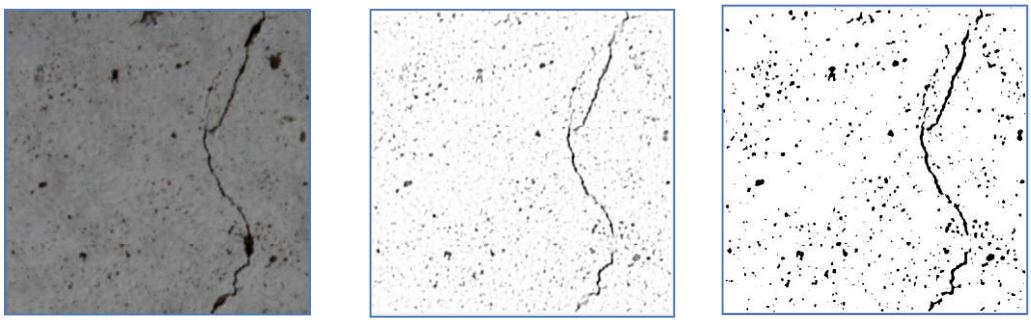

(a) **(b)** **(c)**

Fig.4.4 An example of pre-processing steps. **(a)** Original image. **(b)** Result of median filter and subtraction. **(c)** Result of binarization after median filter and subtraction.

subtracted image shown in **Fig.4.4 (b)**, as expressed in equation:

$$I(x_i) = \max \begin{cases} median_{x_j \in R_j} I(x_j) - I(x_i) \\ 0 \quad otherwise \end{cases} \tag{4.2}$$

Where, $I_{(xi)}$ means the intensity of the pixel x_i, and R_j means the neighbor pixels of the pixel xi. When the subtraction result is negative, the result is replaced by 0.

If the size of median filter is large, the cracks can be removed from the subtracted image. Otherwise, if the size of median filter is small, noises (noise is non-crack parts which is extracted with the cracks) also remain in the subtracted image. Therefore, it is necessary to optimize the size of median filter (fsize).

Finally, binarization step is implemented to reduce noises. All regions which have the value of their pixels over T are converted to 255 (white is background). In contrast, the values below T are converted to 0 (black is crack or noise), as equation:

$$P(i) = \begin{cases} 0 \ if \ I(x_i) > 255 - T(binary) \\ 255 \quad otherwise \end{cases} \tag{4.3}$$

Where, T is a threshold value of binarization, is the i^{th} pixel value of binary image after binarization step. In addition, the threshold value of binarization (binary) also necessary to find out an optimal value. Consequently, fsize and binary are considered as parameters of the iGA in this study. **Fig.4.4 (b)** and **(c)** show examples of pre-processed image in the crack enhancement part.

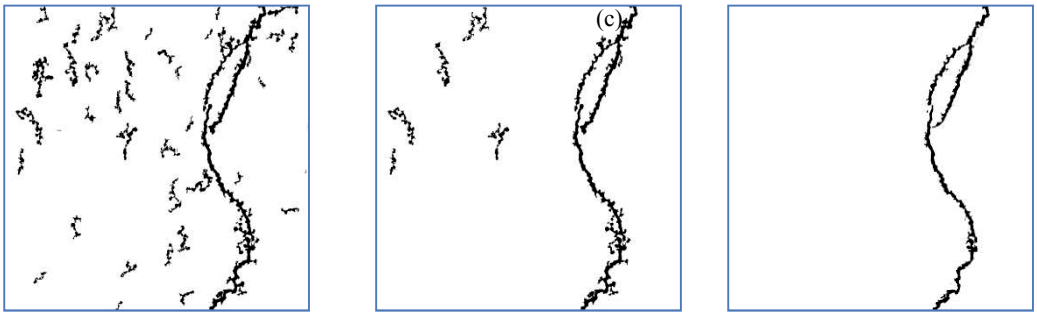

(a) **(b)** **(c)**

Fig.4.5 Result of the proposed method after parameter adjustment. **(a)** and **(b)** background images with t=1 and t=2, respectively, where t is iteration number of the parameter adjustment. **(c)** Final result image after using "Crack extraction" and "Noise removal".

(3) Part3 (Noise removal part)

After Part2, the pixel values of the image are presented by the 0s or 255s. Consequently, the labeling step is to connect neighboring components as a single object with the same number. Hence, a single object can be a crack object or a noise object. In effect, the linear degree step is performed to improve noise removal. The shape of connection component after the labeling step is classified by the following equation:

$$P'(i) = \begin{cases} 255 \ if \ \dfrac{Max\left(R_{xi},\ R_{yi}\right)^2}{S_i} < \mathrm{T}' \\ 0 \qquad otherwise \end{cases} \tag{4.4}$$

Where, T is a threshold value of the linear degree to distinguish between a crack pixel and a noise pixel. Si is the total number of pixels of the ith label. Rxi is the number of pixels of the ith label in the x-axis, and Ryi is the number of pixels of the ith label in the y-axis. is a pixel value in the ith label.

Figure 4.5 (a) and **(b)** show an example of image results of the noise removal part. With visual assessment, the noises are reduced significantly after adjusting the parameters from 1 to 2 iterations. A processed image after finding the optimal parameter values is defined as a background image. The background image still remains the noises. Therefore, this background image needs to be improved by using "Noise removal" function of the proposed software to gain the final result image (see **Fig.4.5 (c)**).

4.2.3 Application of iGA to the image processing parameters optimization

iGA, proposed in the 1980s, is one of the optimization algorithms for solving an implicit or uncertainty problem. The iGA combines the traditional genetic algorithm (GA) with human's intelligent evaluation. The difference between iGA and GA is the individual's fitness evaluation of a population in every generation. In GA, the individual's fitness is calculated by the fitness function. However, in iGA, the individual's fitness is evaluated by the user. The outline of the basic iGA is shown in **Fig.4.6**[41]. It presents sequential steps of the iGA procedure. In this study, the iGA is used for searching optimal values of the image processing parameters because it has many advantages such as the evaluation for each individual's fitness easier than the individual's fitness function of GA, small population size, less number of generations[42]. Full details of the iGA procedure are presented as following four steps:

(1) Generating initial population randomly

Firstly, the three parameters are combined to create an individual in a population. Secondly, each individual is represented by a chromosome encoded to a binary string as **Fig.4.7**. Namely, the fsize is expressed by 6 bits, the binary is expressed by 8 bits and the linear is expressed by 6 bits. The structure of genotype depends on the search range and stepping number of each parameter. For example, the search range of median filter size (Fsize) consists of 64 solutions. This value is with respect to 2^6. Therefore, it is encoded to 6 bits in the chromosome. Similarity, a number of bits of binarization and linear are encoded to the predesigned chromosome.

Finally, an initial population was generated randomly with a predetermined size. In addition, **Table.4.1** shows some parameter values. In that, the search range and step number are based on the preliminary experiments. Moreover, the decode of the above represented chromosome is implemented as the following equation:

$$\begin{aligned} &\text{(Binary)=[decode value]} \\ &\text{(Fsize, Linear)=Steps}\times\text{[decode value]}+1 \end{aligned} \tag{4.5}$$

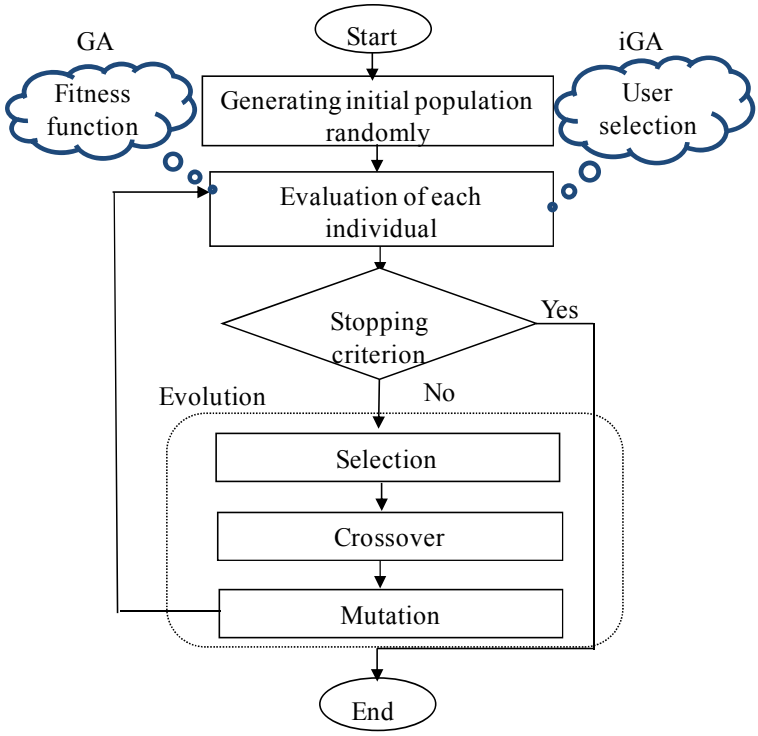

Fig.4.6 iGA procedure.

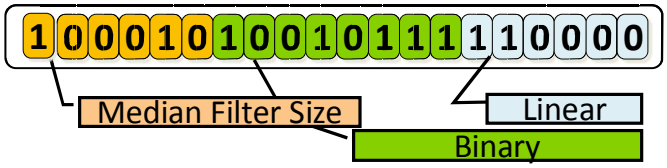

Fig.4.7 Coding presentation of a solution candidate.

Table.4.1 Properties of parameter.

Variable	Range	Steps	Bits
fsize	1≤fsize≤127	2	6
binary	0≤binary≤255	1	8
linear	1.0≤linear≤32.5	0.5	6

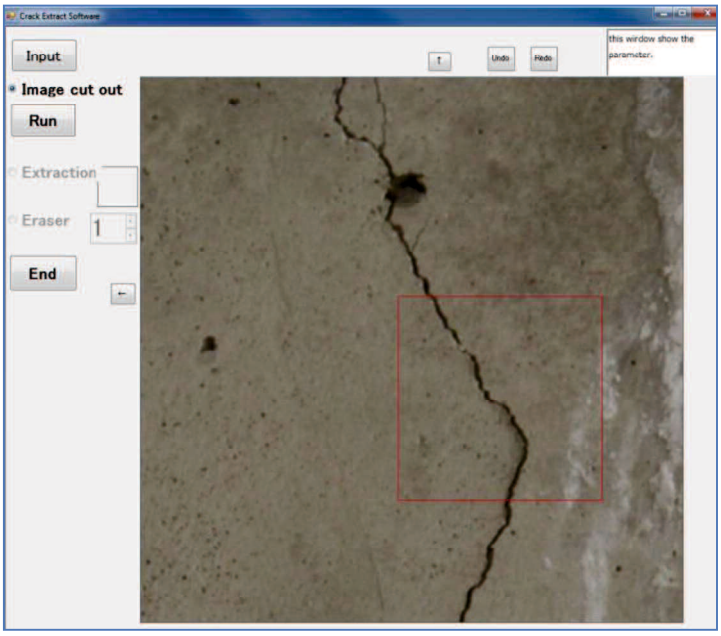

Fig.4.8 Input image window.

(2) Evaluation of each individual

The fitness of each individual (solution candidate) in a population is evaluated based on user's preference. Therefore, the evaluation result is often a relative fitness. This point was different from traditional GA.

(3) Stopping criterion

Evaluation of each individual is terminated by the user when the user chooses the best parameters.

(4) Evolution

When stopping criterion is not satisfied, evolution procedure is implemented for operating selection, crossover, and mutation until the user chooses the best parameters.

4.3 PROTOTYPE SOFTWARE DEVELOPMENT

In this study, the image processing algorithm shown in **Fig.4.3** is developed in the C program language. In addition, an interactive interface of the software for extracting crack and searching optimal parameter values are developed in C # program language (see **Fig.4.8**, **Fig.4.9**, **Fig.4.10**, **Fig.4.11**). The following describes the prototype

software that implements the flow shown in **Fig.4.2**. In addition, each STEP below corresponds to the STEP number of **Fig.4.2**.

4.3.1 STEP1 (Input image)

Firstly, the user inputs an original image by clicking “input” button. Secondly, the user selects a cut-out image to adjust the image processing parameters. Here, the size of the cut-out image is 300 x300 pixels. Finally, the user chooses an interested region of the cracks. Accordingly, a red frame appeared automatically as **Fig.4.8**. The purpose of the crack region selection is to search the optimal image processing parameter values for the cut- out image.

4.3.2 STEP2 (Adjustment of parameters)

The interactive interface is presented as **Fig.4.9** so that the user adjusts the parameters. The software generates 15 sample images (individuals) as an initial population. The user can keep elites (better individuals) to next new generation. If the user cannot keep any individuals, the user has to operate upon “Initialization” to generate a new population. In this window, the user evaluates the fitness of each individual with five buttons from 1 to 5 corresponding to the fitness from the worst to the best. These buttons are located below sample images. Subsequently, the user chooses “Evolution” button to perform gene operators (crossover, mutation). The purpose of evolution is to create a better individual in the new generation until finding out the best individual. As an illustration, **Fig.4.9** also shows that the user finds out sample image (2) with the best parameter values.

The user clicks “End” button to determine at the end of the parameter adjustment procedure. As a result, a background image is created according to the optimal image processing parameter values as **Fig.4.10 (a),** and a crack map (final result image) is shown in **Fig.4.10 (b).** However, the prototype software does not show the user’s background image which is saved automatically in a specific folder.

4.3.3 STEP3 (Crack extraction)

To extract cracks from the original image smoothly, the user traces roughly the shape of the cracks by a finger on the touch panel as **Fig.4.11**. This operation is also

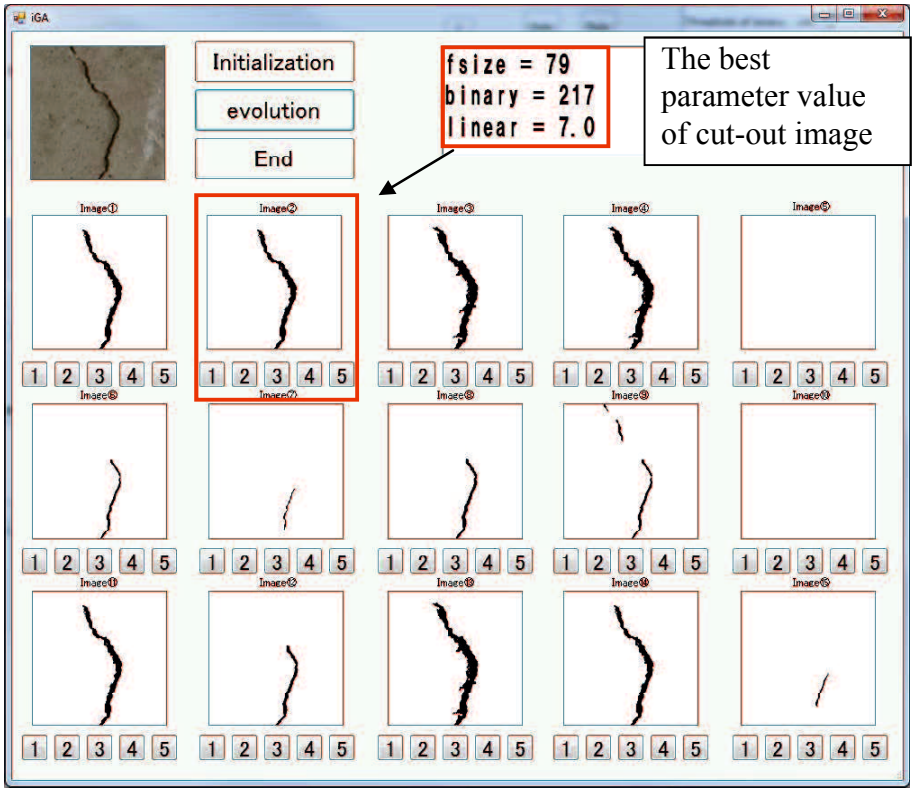

Fig.4.9 Parameter adjustment window.

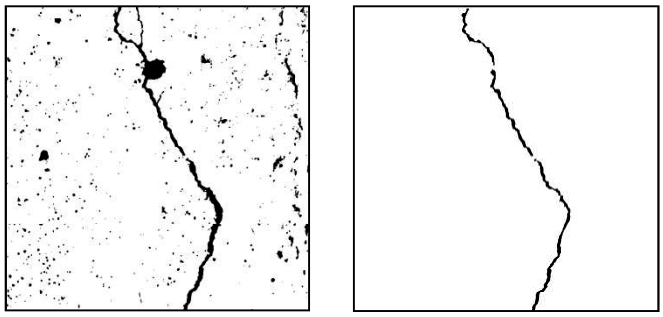

(a) **(b)**

Fig.4.10 The image result using the software.

capable of processing with a computer mouse. The place in which the user traces on the touch panel is displayed as a red line. That is an interested region of crack extraction. Additionally, the width of the extraction area can be adjusted by a size selection which is set in advance from 1pixel to 51pixel (the size increments in 5pixels). After limiting the crack region by a user's fingertip, the cracks are automatically displayed in the selected region with a blue line as **Fig.4.12**.

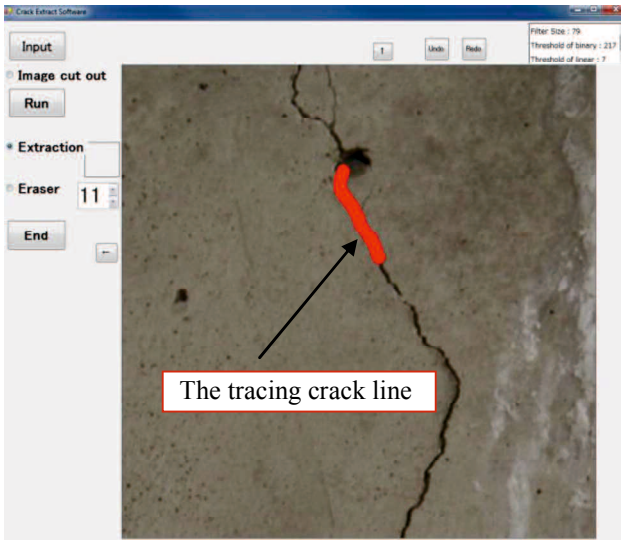

Fig.4.11 Tracing crack on background image.

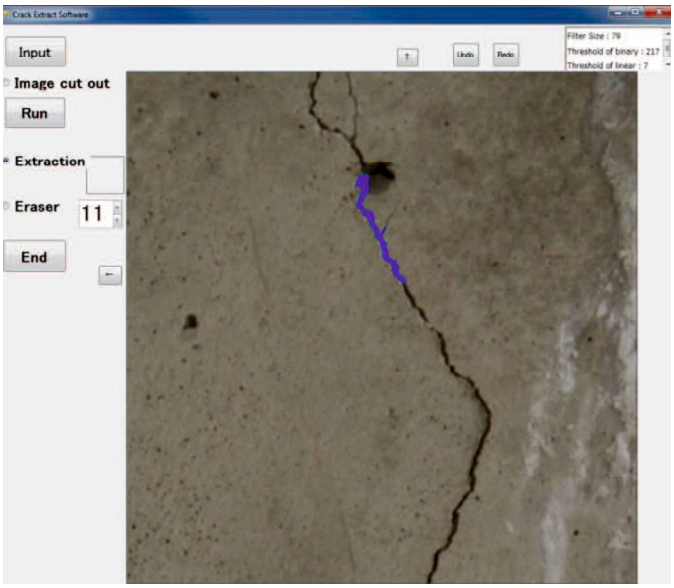

Fig.4.12 Crack extraction image.

The user has to trace region of the crack to extract it from the background image. Hence, the crack of the final result image will be extracted with reduced noises. As a matter of course, depending on the chosen parameter value, the cracks can be appeared with noise pixels or loss pixels. If some crack parts are not displayed, then the user returns STEP 2 to choose other parameter values. If many noises are also displayed as a portion of the crack, then the user moves to next step 4 for noise removal.

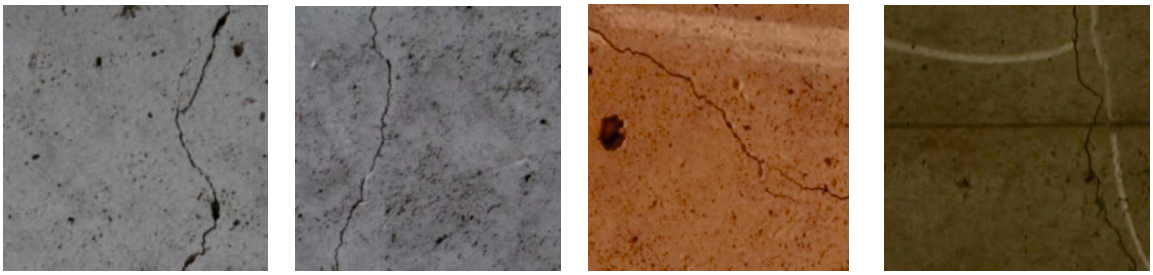

(a) Image A **(b)** Image B **(c)** Image C **(d)** Image D

Fig.4.13 Original image.

4.3.4 STEP4 (Noise removal)

When some noises appear with the cracks are extracted from STEP3, the user selects the “Eraser” button in **Fig.4.12** to carry out a process of noise removal. If the noises are not presented, the user moves to STEP5 without selecting the “Eraser” button.

4.3.5 STEP5 (End determination)

When the user completes the crack extraction process, the user presses “End” button at the bottom left of the window shown in **Fig.4.12**. On the other hand, when the user continues working crack extraction, the user returns to STEP3. If the user wants to choose the parameters again, the user returns to STEP2. Consequently, the outputs of the software have two images automatically saved in the specified folder. Those are a crack extraction image as **Fig.4.10**.

The number of iterations depends on the user’s preference. For example, in the parameter adjustment window, the interaction number will continue until the user chooses the best individual. The number of iterations of tracing crack and removing noise relies on the user skill.

4.4 EXPERIMENT

4.4.1 Sample test

The experiment is implemented with 4 original images which shown as **Fig.4.13**. Additionally, a characteristic feature of the original images is shown as **Table.4.2**. To assess the effectiveness of the software objectively, 3 users who know about image processing and know this software usage are invited to make the experiment. Each user

Fig.4.14 Benchmark image.

Table.4.2 Characteristic feature of the original images.

Image	Image size (pixel)	Resolution (mm/pixel)	Maximum crack width (mm)	Visual characteristic
A	800x800	0.06	0.4	Dirty spot
B		0.06	0.35	Rough Surface
C		0.06	0.4	Honeycombs
D		0.06	0.3	Mold mark

detected and extracted the cracks for 4 selected original images, their upside down images, and their left side right images. Thus, totally 36 test samples were available to conduct experiments. The purpose of the direction change of the original images is to test the accuracy of the crack extraction. The validity of the software is expressed by two criteria comprising working time and accuracy of the crack extraction.

To verify these criteria, a benchmark image is made from the original image by a manual tool as **Fig.4.14**. Working time, the loss and noise rate of final result images were compared to the benchmark images.

4.4.2 Working time measure

To measure working time for the benchmark image, and final result image, the Stopwatch is used during the experiment progress. Effectiveness of the software usage in regards to working time is expressed as following equation:

$$T = \frac{T_1 - T_2}{T_1} \times 100\% \tag{4.6}$$

Where T_1 is working time to make the correct image; T_2 is working time to make the final result image; T is the percent of reduced time.

Table.4.3 Average working time of 3 users.

Image	T_1(second)	User	T_2 (second)	T%
A	1120	#a	142	87
		#b	112	90
		#c	106	91
B	1161	#a	106	91
		#b	100	91
		#c	94	92
C	1492	#a	123	92
		#b	119	92
		#c	95	94
D	1368	#a	95	93
		#b	71	95
		#c	60	96

Table.4.3 shows average working time for 3 users to make the correct image and the crack extraction of 36 sample tests. Comparing the values of T_1 and T_2 of all images, it is expressed that the highest value of T is 96%, and the lowest value of T is 87%. Additionally, the average value of T for all images is 92%. It is concluded that the time is significantly shortened when applying this software to extract the cracks.

In addition, the T_1 values of image C are the highest of all images. In contrast, the T_1 value of image A is the smallest of all images. However, the average T_2 value of 3 users for extracting crack of image A is the highest of all images. It is due to that the shape of image A is more complex than the other images.

In the other hand, the T_1 value of image D is higher than T_1 value of images A and B, but the T_2 value of image D is less than T_2 value of images A and B. Finally, the **Table.4. 3** shows that the T value of image D is the highest of all images which the average value is 95%.

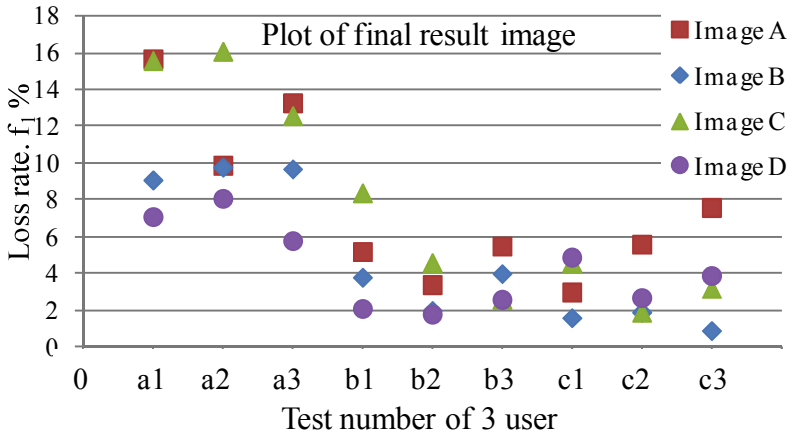

Fig.4.15 Loss rate-Test number.

4.4.3 Crack extraction accuracy measure

To assess the accuracy of the software, evaluation value is determined by following equations:

$$f_1 = \frac{m}{M}; f_2 = \frac{n}{N} \tag{4.7}$$

$$f = 1 - \sqrt{\frac{1}{2}(f_1)^2 + \frac{1}{2}(f_2)^2} \; f \in [0,1] \tag{4.8}$$

where m and n are the number of loss pixels and noise pixels, respectively; M and N are the number of background pixels and crack pixels, respectively; f_1 and f_2 are loss rate and noise rate, respectively; f is evaluation value. The higher value is calculated, the higher accuracy of the software is obtained.

Figs.4.15 and **4.16** show Loss rate and Noise rate of the four original images, their upside down images, and left side right images. The horizontal axis of the plot shows test number of the three users. Namely, user #a has test number (a1, a2, a3), user #b has test number (b1, b2, b3) and user #c has test number (c1, c2, c3).

As a result, with **Figs.4.15** and **4.16**, user #b and user #c have relatively equivalent loss rate and noise rate. The loss rate of user #a is higher than the loss rate of the others, and the noise rate of user #a is lower than the noise rate of the others.

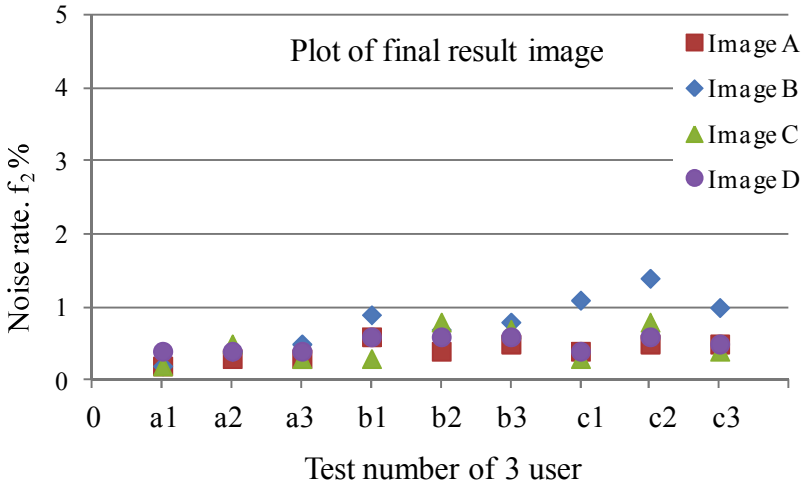

Fig.4.16 Noise rate-Test number.

User #a has loss rate tolerance. However, user #b and user #c have noise tolerance. In **Fig.4.16**, the noise rate of final result image of each original image is almost invariance for the three tests of each user. It is evident that the direction change of the original image does not make influence to the output results.

In addition, in the aspect of crack extraction, images A and C have the loss rate more than images B and D. In contrast, the noise rate of image B has the highest of the four images. The loss and noise rate values of image D have the lowest of the four images. It is concluded that the order of the crack extraction of images are from the easiest as D, following B, A, and C images.

Fig.4.17 also shows an example of crack extraction results of users #b and #c for image D. In the background image, the noise pixels are appeared. However, in the final result, the noise pixels are reduced significantly because the user used “Extraction” and “Eraser” buttons which are shown **Fig.4.12**. In the other hand, the background images of the two users are different because they refer to the different optimal parameter values. Therefore, with the same way of the crack extraction, the both of two users have similar final result images.

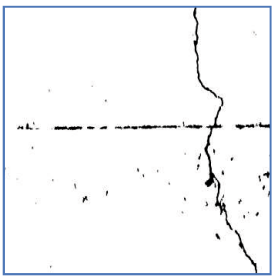

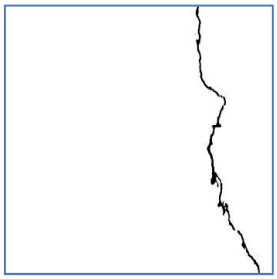

(a) B.g image D of user #b **(b)** F.result image D of user #b

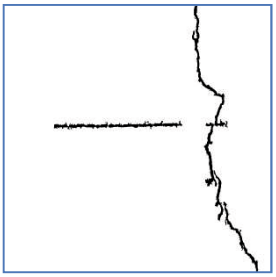

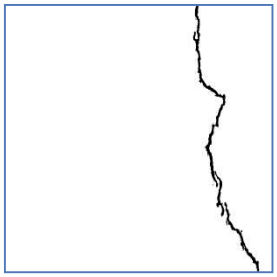

(c) B.g image D of user #c **(d)** F.result image D of user #c

Fig.4.17 Crack extraction results.

Table.4.4 Average evaluation values of three users.

User	Value Evaluation value (f)		
	Max	Min	Ave
User a	0.96	0.89	0.92
User b	0.99	0.94	0.97
User c	0.99	0.97	0.98

Furthermore, **Table.4.4** shows that all users achieve the high evaluation values. The average evaluation value of user #c is 0.98. This value is the highest evaluation value of three users. Meanwhile, the average evaluation value of user #b is 0.97 higher than the average evaluation value of user #a. The average evaluation value of user #a is 0.92. As a result, with the two criteria, it is concluded that user #c achieves the best skill of using the software, and user #b gains the skill of software usage better than user #a.

4.5 EVALUATION AND DISCUSSION

4.5.1 Evaluation method

The proposed method is compared to the Haar wavelet transform (HWT) method with GA to optimize the parameters of HWT. The HWT method is a useful tool for crack detection with many advantages as multi-resolution properties. They are compared to the benchmark image traced by human operator based on loss and noise rate values expressed as the abovementioned (4.2) & (4.3) equations.

The process of wavelet transform method is firstly the wavelet decomposition level which is considered as a parameter which needs to be found optimum value.

Secondly, hard threshold based all sub-band coefficients of HWT are adjusted. If the coefficient values are less than the hard threshold value, they are replaced by 0s (white pixels). Otherwise, they are kept unchanged values. The hard threshold also is taken account into the second parameter of solution candidates to search optimum value. Consequently, a filtering image is reconstructed by inverting wavelet transform Mukhopadhyay.S[43]. Next, the labelling is performed to connect 4-neighboring components. Finally the linear step is implemented as the part 3 of the proposed method, and it also is considered as the third parameter of solution candidate. As a result, the candidates of solution are encoded into binary string 16 bits which include the level the composition (2bits), the hard threshold (8 bits), the linear (6 bits).

In this paper, the experiments are implemented for the two methods with 2 original images as sample tests. In addition, parameters of GA involve size of population is 16, maximum number of generation is100, probability of crossing over is 0.9; probability of mutation is 0.1. The numerical and visual results of the experiments are shown in **Table. 4.5** and **Fig.4.18**, respectively.

4.5.2 Discussion

As a result, **Table.4.5** shows HWT method with GA, the proposed method with GA, and the proposed method with iGA. In this table, the accuracy of crack detection of the proposed method outperformed than HWT method. Additionally, after implementing the

Table.4.5 Result of the accuracy analysis of wavelet transform, the proposed method and the noise removal function of the crack detection software.

Image	HWT with GA	The Proposed method with GA (Computer)	Semi-Automatic crack detection (Human-Computer)
1	f_1= 4.16% f_2= 6.65% f= 94.5%	f_1=4.12% f_2= 1.67% f= 98.6%	f_1=1.38% f_2= 0.71% f= 99.0%
2	f_1= 12.97% f_2= 5% f= 90.17%	f_1= 3.02% f_2= 9.43% f= 92.9%	f_1=5.63% f_2= 0.42% f= 96.0%

crack detection software, the accuracy of crack detection was improved significantly. It is expressed that the effectiveness of the proposed software (see more **Fig.4.18**). In fact, each real image has various and complex conditions, so the results of the accuracy rate are different for each image. As can be seen, the best way for crack detection from concrete structure surface images is that the parameters of the image processing need to be adjusted for each image.

4.6 CONCLUSIONS

With the two evaluation criteria, the experiment results indicated that the proposed method has achieved reasonable accuracy and working time. Furthermore, in this experiment, the average working time for the extracting crack of each image reduced about 87%. If the crack extraction is performed by the proposed software for a thousand of images, it will save a great deal of time.

This paper proposed a robust method for crack semi-automatic detection from concrete surface images. Moreover, the prototype software is developed based on iGA with the image processing technique. Especially, using a touch monitor, the easiness and efficiency of the proposed crack detection software is remarkable. The semi-automatic method adjusts the image processing parameters for each image without benchmark images as well as the objective function.

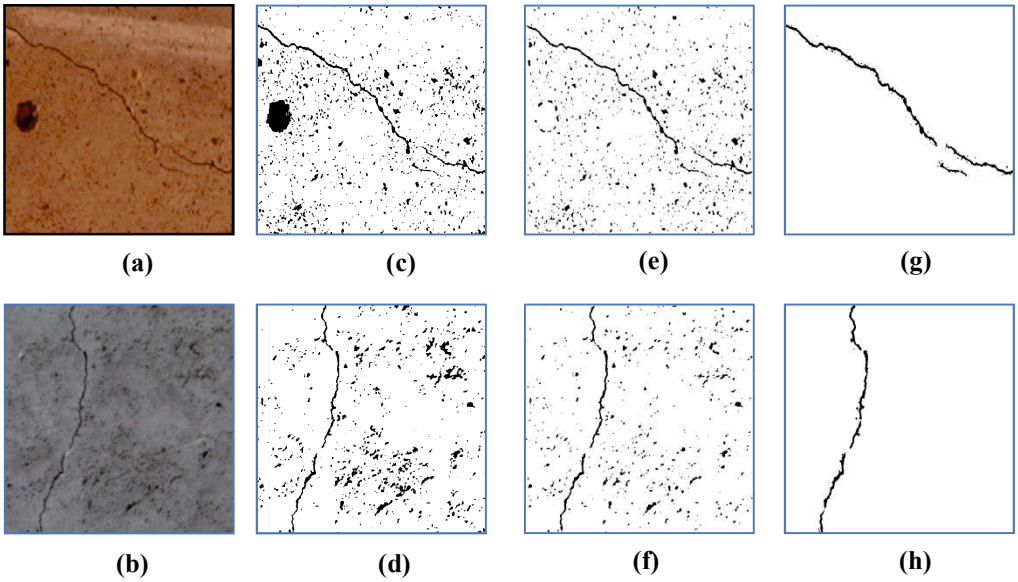

Fig.4.18 Visual comparison. **(a)**, **(b)** Original images. **(c)**, **(d)** Results by the HWT method. **(e)**,**(f)** Results by parameter adjustment of the user (background images). **(g)**, **(h)** Final result images.

The semi-automatic method yielded the higher accuracy than the other. Therefore, it can be used to make the ground-truth images for shortening time compared with the manual method. Moreover, the crack detection software is able to fast detect crack for large-size crack images. The large-size image can be divided into sub-images. An interest of region (ROI) is chosen to adjust the image processing parameters while the neighbour regions can receive the same parameter value. If the neighbour regions have texture or intensity difference they are necessary to adjust the different parameter value.

CHAPTER 5

A CRACK DETECTION METHOD FOR CONCRETE INFRASTRUCTURES BASED ON IMAGE PROCESSING TECHNIQUE AND GENETIC ALGORITHM

This chapter presents a crack detection method based on genetic algorithm to optimize the parameters of image processing technique (IPT). Morphological mathematic is applied to the pre-processing step in order to smooth the original image. Next, the global binarization and dilation-thinning operation is used for segmentation and noise removal. Moreover, the experimental results of the proposed method compared to other methods for concrete infrastructure surface images under various complex photometric conditions validate the reasonable accuracy in practical applications.

5.1 INTRODUCTION

Many concrete components of existing infrastructure systems such as bridges, and tunnels have suffered from various geologic, loading and environmental conditions cause to cracks which make influent to quality of operations. Therefore, the condition assessment of the existing infrastructures is an important task not only for warming against deterioration but also for guaranteeing soon maintenance. Concrete cracks are important indicators reflecting the safety of infrastructure. The automatic crack detection of infrastructure surface is typically usage of non-destructive testing technique. This technique can be implemented using some of different image data

captured from ultrasonic device, infrared and thermal device, laser scanning, and commonly digital cameras.

Due to availability of high accuracy, simplicity and low-cost, the digital camera image based crack detection has rapidly increased in recent years. In addition, there are main three approaches based on threshold technique Ito et al[44]; Miyamoto et al[11]; Fujita el al.[12], edge detection technique Yu et al[23], and model-based approach Zhu et al[45]. The crucial drawback of the threshold-technique approach is questionable.

It is difficult to choose a suitable threshold value for extracting crack pixels in various complex back ground images. This method typically selects a threshold based on prior knowledge. If the threshold value is too large the crack pixels is lost. The threshold value is too small to appear much noise pixels. Therefore, the threshold value has to search an optimal value based on convolution algorithms.

Abdel-Qader et al[13] compared to some of edge detection algorithms and found Haar Wavelet Transform (HWT) method to be the most reliable of them. However, comparing other methods[12, 46], HWT method didn't yield the high accuracy for automatic crack detection based on edge detection technique. According to Chaiyasarn the accuracy of model based approach is relied on user input to initialize the seed pixels[3]. Consequently, hairline cracks may not be detection because users may be unable to identify the seed pixels. To achieve the accuracy of automatic crack detection, the parameters of image processing technique have to find the optimal values based on convolution algorithms.

In recently years, Kawamura et al proposed interactive genetic algorithm is applied to adjust the image processing parameters. It is developed to extract crack pattern effectively. Nishinkawa et al[47] designed System for Automatic Construction of Image Filter (SACIF) based on a genetic program to detect cracks on concrete structures. The main aim of this paper is to combine genetic algorithms (GA) adjusted optimized parameters and IPTs which are capable of detecting the cracks of the various complex surface images of the concrete infrastructures.

Although the accuracy of the semi-automatic crack detection method is high. However, it relied on the user's preference for individual fitness assessment.

Further computational time of crack extraction for each image was faster than the manual method, but it is impossible to adjust parameters for a huge number of images

acquired from the huge and large tunnel lining .Therefore, to improve the capacity of the thin crack detection in the various complex environmental conditions, an automated crack detection method based on mathematic morphology transform is also proposed, which consists of morphological filter, binarization, dilation-thinning transformation, and linear degree. The optimum parameters of IPT are also adjusted by genetic algorithm.

5.2 PROPOSED METHOD

5.2.1 Overview

In practical applications, surface images of concrete infrastructures are captured under various conditions. Raw original images include in useless information called noises due to uneven illumination, low contrast, and other distortions. Therefore, pre-processing step is substantial to smooth the original image. Many researchers use image filters such as wavelet transform[13], Laplace Sobel transformation[23], mathematic morphology[48), 49)], and median filter[12), 46)].

In this chapter, morphological operations are applied to smooth and remove the noises of the original images. After that, histogram equalization is applied to enhance the contrast before binarization. Next, dilation-erosion transform is used to sharp the crack pixels and remove noise. Finally, length threshold is adopted to clean noise significantly. Moreover, authors use GA to search the optimized parameter values of the IPT. The proposed method compares with Nguyen et al's methods[46].

5.2.2 Image processing technique

Fig.5.1 shows the image processing procedure included in three main parts. Namely, there are filtering image part, binary image part, and crack extraction part. Therein, filter image part comprises of morphological filter transform and contrast enhancement. The second part consists of binarization, and dilation-thinning transformation. The final part comprises of labeling and length threshold. The detailed steps as follow:

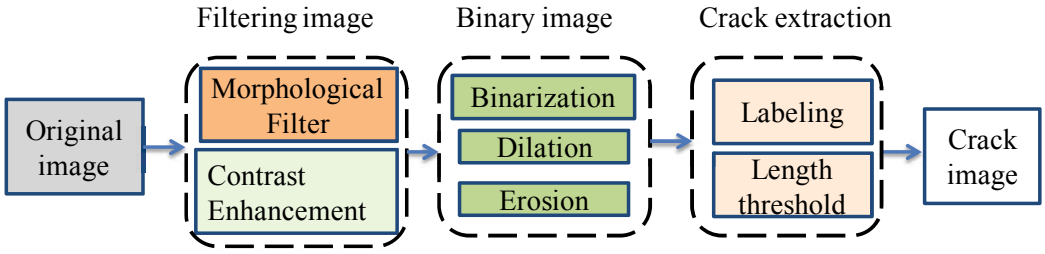

Fig.5.1 Image processing procedure.

(1) Morphological filter

The morphology filter consists of opening of closing operation on gray-scale image with a predefined structuring element as the following equation:

$$M = \max([(I \bullet S) \circ S], I) - I \tag{5.1}$$

Where M means the smooth image after morphological image processing, S is a structuring element shows in **Fig.5.2**. 'o' and '•' are the morphological opening and closing operators. I is a gray-scale image converting from the corresponded original image. Additionally Opening transform includes dilation of erosion. Closing is an inverse operator of the opening as the following Eqs. (2) and (3):

$$(F \circ S) = (F \Theta S) \oplus S \tag{5.2}$$

$$(F \bullet S) = (F \oplus S) \Theta S \tag{5.3}$$

Given grayscale image $F_{(x,y)}$ and structuring element $S_{(u,v)}$, the dilation and erosion operations are defined by:

$$(F \oplus S)_{(x,y)} = \max_{u,v}(F_{(x-u,y-v)} + S_{(u,v)}) \tag{5.4}$$

$$(F \Theta S)_{(x,y)} = \min_{u,v}(F_{(x-u,y-v)} - S_{(u,v)}) \tag{5.5}$$

The purpose of this part is firstly to smooth image as well as eliminate noises and shading and then make the sharpness of crack edge. For an example, **Fig5.3 (b)** shows the result of smooth image *M*.

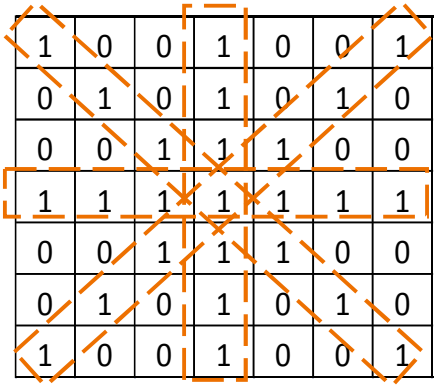

Fig.5.2 A designed structuring element with combination of four directions and (7x7) pixels size of line-type.

(2) Structuring element design

Because the shape of crack is irregular elongation, the shape of the structuring element of line-type is adopted. To retrieve fully crack information in the various directions, combination line types of four directions into the structuring element such as $\{0^0, 45^0, 90^0, 135^0\}$ or six directions $\{0^0, 30^0, 60^0, 90^0, 120^0, 150^0\}$. In this study, the former type is used to reduce computational volume.

(3) Contrast Enhancement

Surface images of civil infrastructure are the typical dark environmental condition, narrow contrast. The intensity of crack pixels and background pixels is not much difference. Therefore before binarization is applied a histogram of the raw image is equalized to sharpen crack pixel as the following equation:

$$q_k = \sum_{i=0}^{k} \frac{n_i}{n} \quad k = 0,1,2,..L-1$$
$$I_k(out) = (I_{max} - I_{min}) \times q_k(in) + I_{min} \tag{5.6}$$

Where, n_i: is number of pixels that have i^{th} gray-scale value. n: the number of pixels; k: the input gray-scale level. L: the maximum gray-scale level (255).

q_k: acquired normalized histogram. I_{max} and I_{min} are respective to the maximum and minimum intensities of the original image. $I_k(out)$ is the new gray-scale intensity of the input pixel having $q_k(in)$. As a result, **Fig.5.3 (c)** shows crack enhancement after morphology filter is applied to smooth the original image.

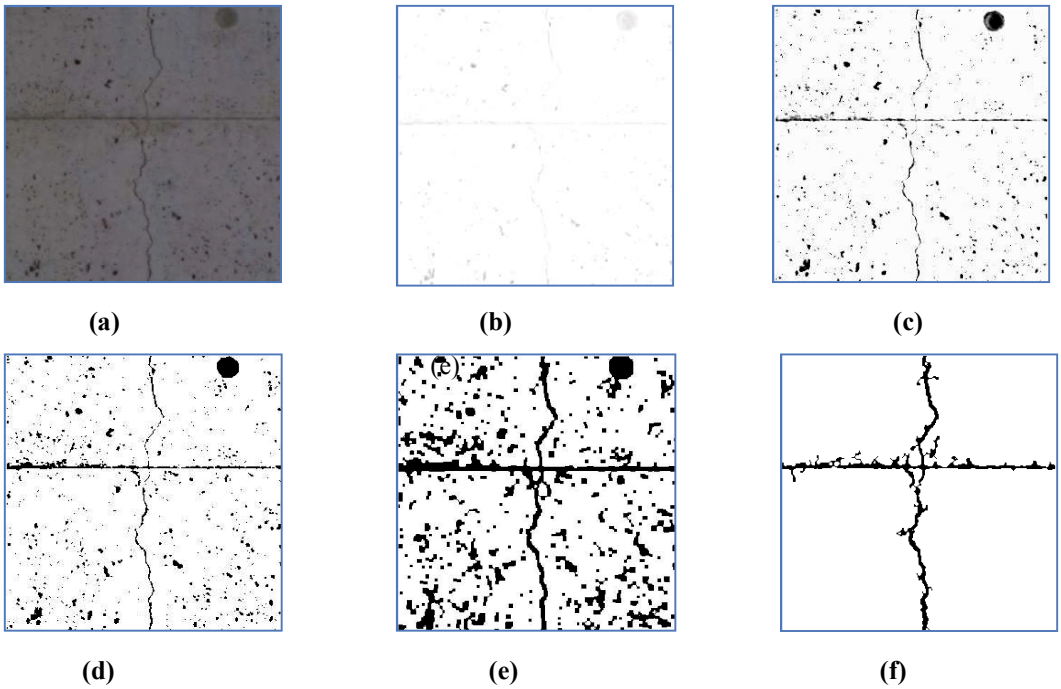

(a): Original image; **(b)**: Morphological filter; **(c)**: Contrast enhancement; **(d)**: Binarization; **(e)**: Dilation-thinning transform; **(f)**: Final crack image.

Fig.5.3 The illustrative results of image processing procedure.

(4) Binarization

The purpose of this step is to segment crack image into binary image. The output image only has two values 255 (white is background) and 0 (black is crack or noise). This step is performed same binarization in chapter 4. Furthermore, in this study, to evaluate the effectiveness of the binarization, the accuracy of crack detection used global optimized threshold compared to Otsu's threshold method.

(5) Dilation

The aim of a dilation operation is to connect crack fragment meanwhile noises are separated from the cracks. Therefore it results in loss reduction. However, widths of crack pixels increase along with crack shape. The size of structuring element of the dilation operation is considered as an adjusted parameter to optimized value by GA. Shape of structuring element is predefined as "square" type. The rule of the dilation operation is if any pixel in the input neighbourhood is "1", the output pixel is "1". Otherwise, the output pixel is "0".

(6) Erosion/Thinning

Erosion to a binary image is a morphology operator used to remove noise surrounding crack pixels. Lam et al [50]. The purpose of this step is to prune branches from the crack shape as well as reduce noises after dilation operator is performed. **Fig.5.3 (e)** shows the image processing result of dilation and erosion transform.

(7) Labeling and length threshold is presented as chapter 4. After the length threshold is implemented, the image result of the crack detection is shown in **Fig.5.3 (f).**

5.2.3 Application of GA to the optimization of image processing parameters

In this study, the GA is applied to search optimal values of the image processing parameters (IPPs) because its advantage is to avoid local optimization as other conventionally evolutional algorithms.

(1) Represented chromosome design for solution candidates

No losing generality, assumption that a solution candidate is represented by a chromosome of an individual in the population. The chromosome contains information in term of tuned parameter values which is encoded by binary strings. A population comprises of 20 individuals. Weak individual will be removed and the quality of population is improved by performing genetic operations in each generation.

Firstly, the IPPs are combined to create an individual in a population. Secondly, each individual is represented by a chromosome encoded to a binary string, as shown in **Fig.5.4**. Namely, the size of structuring element (st) is assigned by 6 bits, the threshold value of binarization (bi) is expressed by 8 bits, dilation transform parameter (di) is expressed by 4 bits, the threshold value of object area is designed by 6 bits. Finally, an initial population was generated randomly with a predetermined size. And the linear degree is expressed by 6 bits. **Table.5.1** shows some parameter values. Therein, the ranges of the shown values are based on the preliminary experiments.

(2) Genetic algorithm

Fig.5.5 shows an operated mechanism of GA including into the crucial three stages. Namely, they consist of the initial population generation, fitness evaluation of each individual in the current population, and evolution operation to create the next

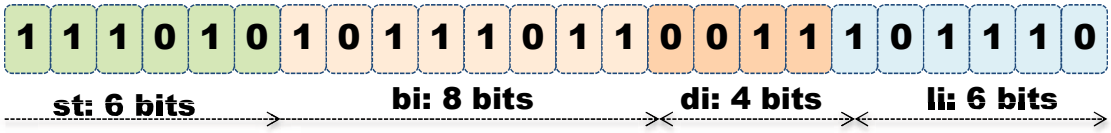

Fig.5.4 A represented chromosome for solution candidates.

Table.5.1 Properties of parameter.

Variable	Range	Steps	bits
st	[1 127]	2	6
bi	[0 255]	1	8
di	[1 31]	2	4
li	[0 32.5]	0.5	6

generation. Therein, the evolution operation comprised of selection, crossover, and mutation is repeated until finding best solution. Namely, the detailed steps are presented as the following three steps:

Step1. Generate initial population randomly:

An initial population was generated randomly with a predetermined size to start fitness evaluation. The larger number of individuals means the faster convergence. However, the running time of the program is slow. The semi-automatic and fully automatic methods select 15 and 20 individuals in a generation, respectively. To assess the fitness of the individual in the current population, an objective function to assess crack detection accuracy is defined as the Eq.(9). Loss and noise are computed based on comparison between the processed image and the target image shown in **Fig.5.6**.

As a result, the objective function (*f*) has to ensure the accuracy of extracted crack information with the minimum noises and losses as much as possible.

$$f = 1 - \sqrt{\frac{f_1^2}{2} + \frac{f_2^2}{2}}, f \in [0\ 1]$$
$$f_1 = \frac{\text{Loss}}{Crack}; f_2 = \frac{Noise}{Back} \tag{5.7}$$

Fig.5.5 Optimal parameter adjustment using the genetic algorithm.

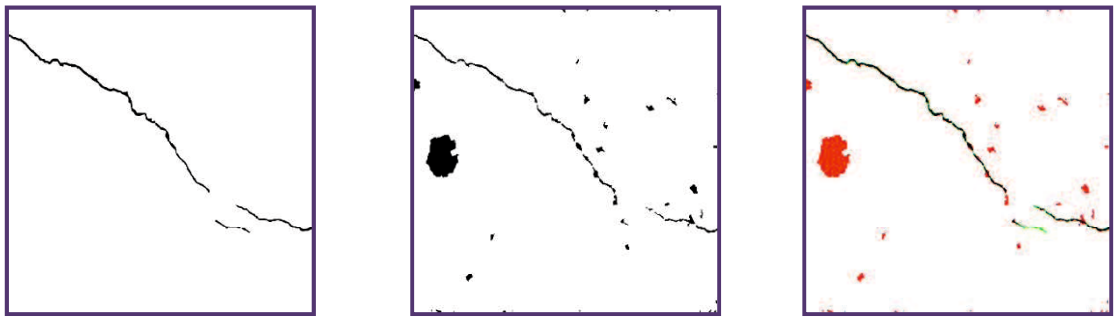

(a) Target image **(b)** Processed image **(c)** Compared image

Crack and Back are black and white pixels on the Target image, respectively. Meanwhile, Noise is a number of black pixels that appear on the processed image, but it doesn't appear on the target image. Whilst, Loss is a number of pixels that don't appear on the processed image compared to the target image.

Fig.5.6 Target image based fitness evaluation.

Where, f_1, f_2 are loss rate and noise rate, respectively. f measures the accuracy of crack detection. f is larger value, the accuracy is higher.

Step2. Evolution operation:

Selection progress is to mimic the natural survival of the creatures. Each string has a corresponded fitness value. The probability of each string to be selected is proportional to its fitness value based on the roultte wheel rotation randomly. The process is repeated for the second parent. Two elite members are kept forward to the next generation.

To improve quality of individual fitness, the crossover operation is used to create two new children from two selected parents with predefined probability. Crossover point is point laid on between 0 to the end of chromosome length. In this study, the single crossover point is selected. The part of the first parent chromosome that runs until the crossover point is spliced with the part of the second parent chromosome that includes, and runs after, the crossover point shown in **Fig.5.5**. The whole new generation is selected in this manner.

The mutation of bit strings ensue through bit flips at random positions. The purpose of the mutation operation is to create genotype diversification in the population in order to avoid local optimization leading to finding the best solution. Mutation point is chosen randomly. However, mutation rate is very small under 1% to avoid collapsing the genetic structure of the current population.

Step3. Stopping criterion:

Evaluation of each individual meets the predefined maximum generation, or the best value of the objective function is found.

5.3 EXPERIMENT

5.3.1 Sample test

The tunnel lining surface images were captured in various complex environmental conditions. Each inspection image of (3456x4608) pixels with 0.072 mm/pixel resolution was divided into 300x300 pixels to reduce computation time effectively.

This paper used the following equation (10) to estimate the detectable minimum crack width[51].

$$w \geq 0.5 \times fs \times r \tag{5.8}$$

Where w is the detectable crack width; fs is the size of the structuring element; and r is the image resolution. Therefore, the detectable minimum crack width of the proposed method would be 0.25 mm because the size of a structuring element is 7x7 pixels and the resolution of the original images in this paper is 0.072 mm/pixel. However, the formula was not verified by experiment in this paper. In the future, the authors will confirm the detectable minimum crack width.

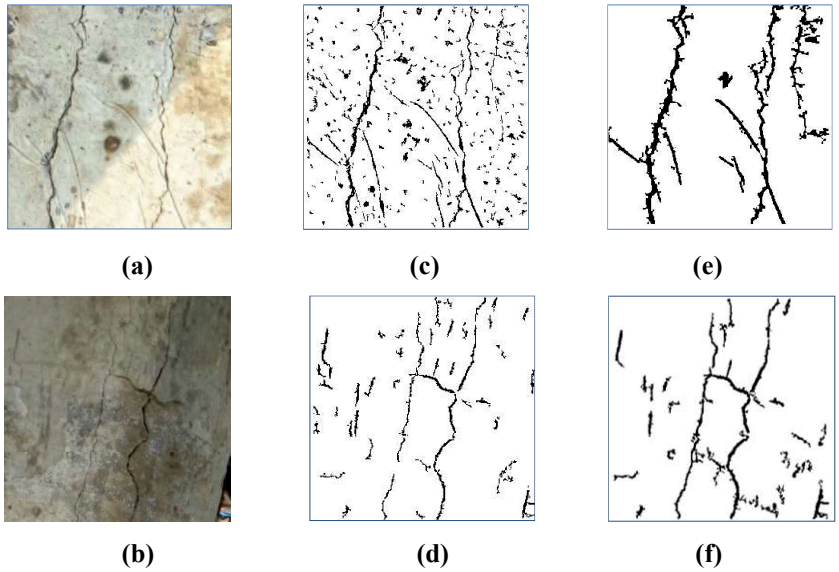

(a)&(b): Original images; **(c)&(d)**: Proposed method without dilation/erosion has the accuracy f=0.8575 & f=0.8753, respectively: **(e)** & **(f)** : Proposed method with dilation/erosion has the accuracy f=0.9542 and f=0.959.

Fig.5.7 The effectiveness of the dilation and erosion transformation.

5.3.2 The dilation and erosion transform experiment

Fig.5.7 shows the results of the experiment of the proposed method with and without dilation–thinning transform. As a result, without dilation-erosion transform, the accuracy of crack detection result decreases due to noises. Having dilation-erosion transform, the accuracy (*f)* of crack detection is improved significantly from 0.8575 to 0.9542 for **Fig.5.7 (a)**, and from 0.8753 to 0.9595 for **Fig.5.7 (b)**.

5.3.3 Performance evaluation based on loss and noise ratio

To validate the effectiveness of crack detection algorithms, the crack detection accuracy of the proposed method (denoted method 1) is compared to the one of our previous method called method 2 (Nguyen et al2016). As can be seen in **Fig.5.8**, the first column is original images. The second column is the target images. The third column is the results of proposed method. The fourth column is the results of method 2. The accuracy value of crack detection of the method 1 is higher than the one of the method 2.

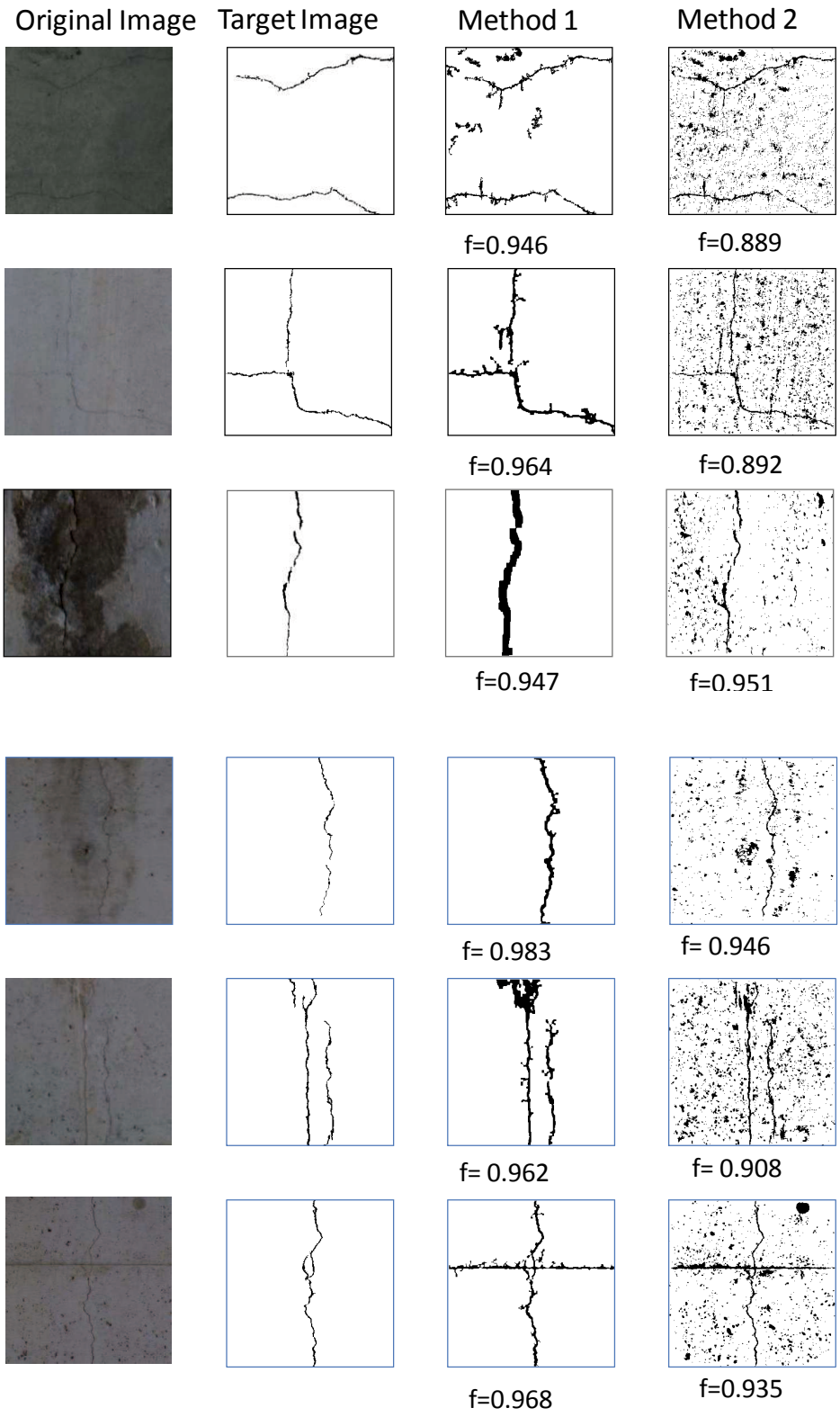

Fig.5.8 The crack detection results of proposed method and our previous method.

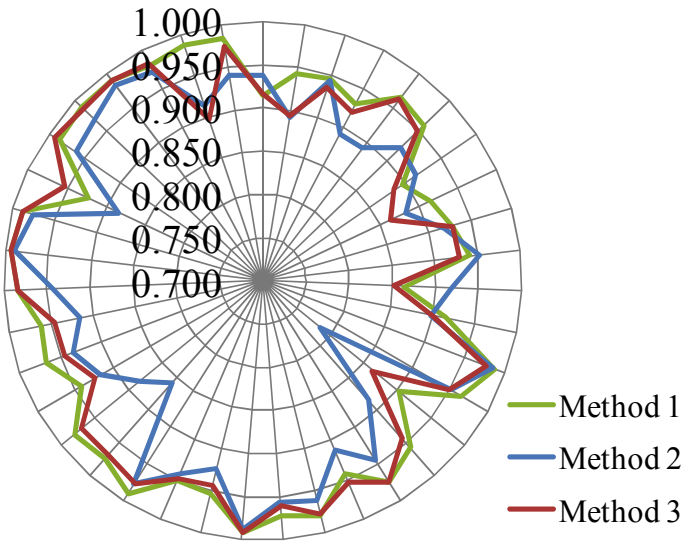

Fig.5.9 Comparison of the accuracy of crack detection methods.

However, the crack line of the method 1 is wider than the target image while the crack width of method 2 is similar to the one of the target image. This reason is that the main aim of the method 1 is to remove the noises surrounding the crack line using the dilation-thinning transform. In contrast, the method 2 prefers to reduce the noise laying the crack line. These tendencies depend on image processing techniques in the methods. So far, the average accuracy of the crack detection using methods 1 and 2 are 0.9578 and 0.9202, respectively. It is concluded that application of dilation-thinning transform with the optimal size of the structuring element based on GA improves the crack detection results extremely.

Further, **Figs.5.9, 5.10** and **5.11** show the results of comparison three methods. Therein, method 3 is the proposed method using Otsu's threshold Otsu et al[52] instead of the global optimized threshold of the binarization by GA. As can be seen in **Fig.5.9**, the vertical axis is the accuracy of crack detection method, and the horizontal axis is number of sample tests included 40 images with various environmental conditions. As a result, the best crack detection accuracy belongs to method 1. The results of method 3 are better than method 2. There are not much difference between method 1 and method 3. As shown in **Fig.5.10** the loss ratio of the crack detection results using method 2 is relative high compared to the ones of other methods.

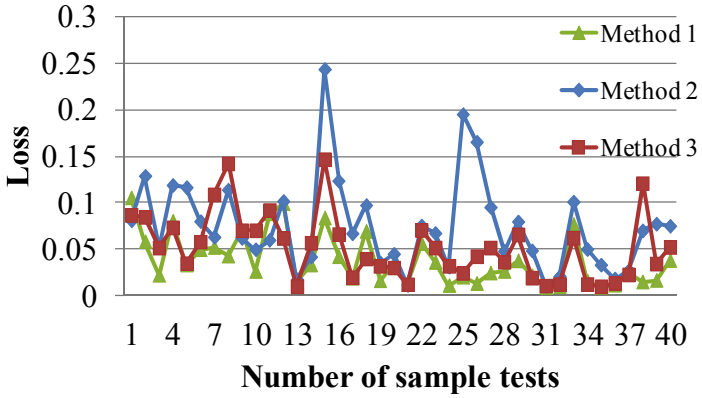

Fig.5.10 Comparison of the loss of crack detection methods.

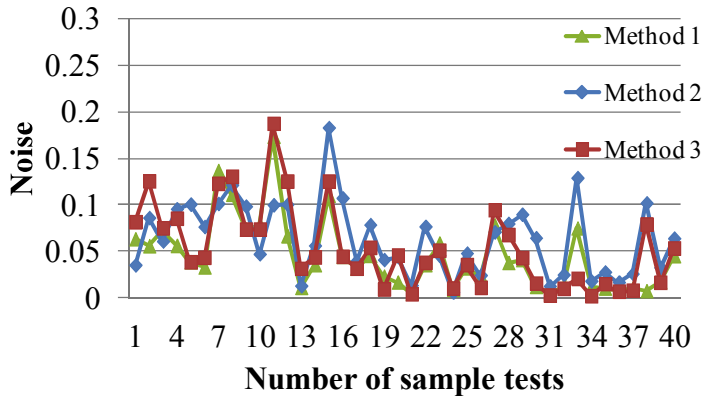

Fig.5.11 Comparison of the noise of crack detection methods.

Meanwhile, the noise ratio shown in **Fig.5.11** doesn't have much difference among three methods. To the end, **Table.5.2** shows the comparison results of three methods. The sample tests in this experiment are not complete. However, they are effective enough to supply a sense of the ideas validated this work. The average accuracies of the methods 1,2, and 3 are with respect to 95.7%, 94.6% and 92.9%.

Table.5.2 The comparison results of three methods.

Images	Method 2			Method 3			Method 1		
	f1	f2	f	f1	f2	f	f1	f2	f
1	0.081	0.035	0.938	0.087	0.081	0.916	0.105	0.063	0.913
2	0.129	0.086	0.891	0.084	0.125	0.893	0.058	0.056	0.943
3	0.052	0.061	0.944	0.051	0.075	0.936	0.022	0.072	0.947
4	0.119	0.095	0.892	0.073	0.085	0.921	0.080	0.056	0.931
5	0.116	0.100	0.892	0.035	0.038	0.964	0.033	0.038	0.964
6	0.080	0.076	0.922	0.058	0.043	0.949	0.049	0.033	0.958
7	0.063	0.101	0.916	0.109	0.123	0.884	0.052	0.136	0.897
8	0.114	0.121	0.883	0.142	0.130	0.864	0.043	0.111	0.916
9	0.062	0.098	0.918	0.070	0.073	0.928	0.070	0.073	0.928
10	0.050	0.047	0.952	0.070	0.073	0.928	0.026	0.078	0.942
11	0.060	0.100	0.918	0.092	0.187	0.853	0.088	0.173	0.863
12	0.101	0.100	0.899	0.062	0.125	0.901	0.099	0.066	0.916
13	0.017	0.013	0.985	0.010	0.031	0.977	0.014	0.011	0.987
14	0.042	0.056	0.951	0.057	0.044	0.950	0.033	0.035	0.966
15	0.243	0.183	0.785	0.146	0.125	0.864	0.084	0.110	0.902
16	0.123	0.107	0.885	0.066	0.044	0.944	0.042	0.044	0.957
17	0.067	0.039	0.945	0.019	0.031	0.974	0.019	0.031	0.974
18	0.097	0.078	0.912	0.039	0.054	0.953	0.069	0.045	0.942
19	0.035	0.041	0.962	0.032	0.009	0.977	0.016	0.023	0.980
20	0.045	0.044	0.956	0.030	0.046	0.962	0.035	0.016	0.973
21	0.011	0.013	0.988	0.012	0.004	0.991	0.012	0.005	0.991
22	0.075	0.076	0.924	0.070	0.038	0.944	0.056	0.035	0.953
23	0.067	0.045	0.943	0.051	0.051	0.949	0.036	0.058	0.952
24	0.031	0.006	0.978	0.032	0.010	0.977	0.011	0.009	0.990
25	0.195	0.048	0.858	0.024	0.035	0.970	0.020	0.032	0.974
26	0.165	0.024	0.882	0.042	0.011	0.969	0.013	0.023	0.981
27	0.095	0.070	0.916	0.051	0.094	0.924	0.025	0.078	0.942
28	0.048	0.080	0.934	0.036	0.068	0.946	0.026	0.037	0.968
29	0.079	0.089	0.916	0.065	0.043	0.945	0.037	0.041	0.962
30	0.048	0.064	0.943	0.019	0.015	0.983	0.021	0.012	0.983
31	0.010	0.012	0.989	0.011	0.002	0.992	0.009	0.005	0.993
32	0.021	0.025	0.977	0.012	0.010	0.989	0.010	0.011	0.990
33	0.101	0.129	0.884	0.062	0.021	0.954	0.077	0.075	0.924
34	0.050	0.018	0.963	0.012	0.002	0.991	0.016	0.011	0.986
35	0.033	0.027	0.970	0.010	0.015	0.988	0.009	0.010	0.990
36	0.018	0.016	0.983	0.013	0.007	0.990	0.011	0.007	0.991
37	0.027	0.026	0.974	0.022	0.008	0.983	0.025	0.010	0.981
38	0.070	0.102	0.913	0.121	0.079	0.898	0.015	0.007	0.988
39	0.077	0.032	0.941	0.034	0.016	0.973	0.017	0.017	0.983
Average	0.075	0.064	**0.929**	0.052	0.053	**0.946**	0.038	0.045	**0.957**

Table.5.3 Comparison in unit pixel between Ground-truth image (G) and processed image (P).

P G	1	0
1	TP	FP
0	FN	TN

5.3.4 Performance evaluation based on ROC curve analysis

(1) Receiver Operating Characteristic Curve (ROC) definition

ROC curve are frequently used to show in a graphical way the connection/trade-off between sensitivity or true positive ratio (TPR) and 1- specificity or false positive ratio (FPR) for every possible cut-off for a test or a combination of test[12)].

TPR and FNT are determined by the following equations:

$$\begin{aligned} TPR &= \frac{TP}{TP+FN} \\ FPR &= \frac{FP}{FP+TN} \end{aligned} \tag{5.9}$$

Where TP: true Positive, the total number of crack pixel of processed image is detected correctly as a crack pixel of G-T shown in **Table.5. 3**; FP: the total number of crack pixel of processed image is detected incorrectly as a crack pixel of G-T (noise pixels); FN: False negative is the total number of crack pixel of G-T is not detected in the processed image; FP: the total number of non-crack pixel of G-T is detected as a crack pixel of processed image; TN: the total number of non-crack pixel of G-T is not detected as a crack pixel of processed image; 1: Crack Pixel; 0: Non-crack pixel.

(2) Experiment

ROC analysis for 2000 results consists of 20 individual for each generation and the total number of generation is 100. Data of ROC curve is taken from the best results of the 5 times of program implement. As a result, **Figs.5.12** and **5.13** show the ROC curve analysis result of the original image 19 and 36 using the three methods. In ROC analysis, the closer curve is to upper left corner, the better is the performance. Therefore, the result of the proposed method (method 1) outperforms the results of methods 2&3.The difference of ROC curve between method 1 and method 2 is not significant.

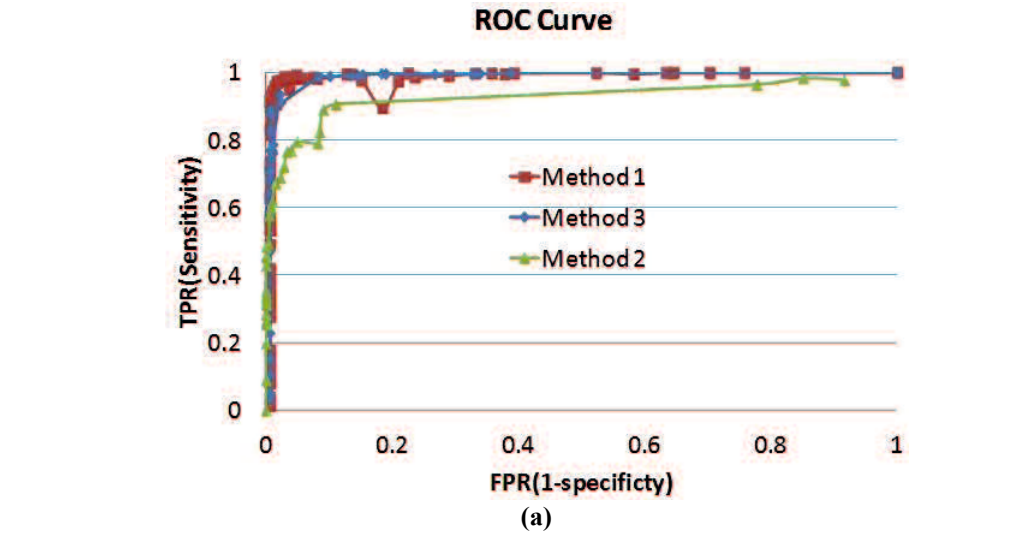

(a)

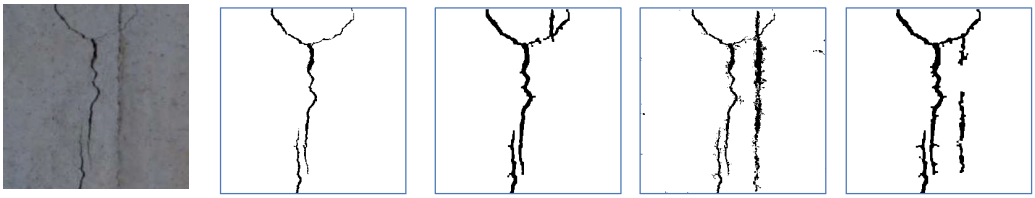

Orig.19 Target.19 Method1 f=0.981 Method2 f=0.975 Method3 f=0.977

(b)

Fig.5.12 Comparison of the ROC curve among three methods.

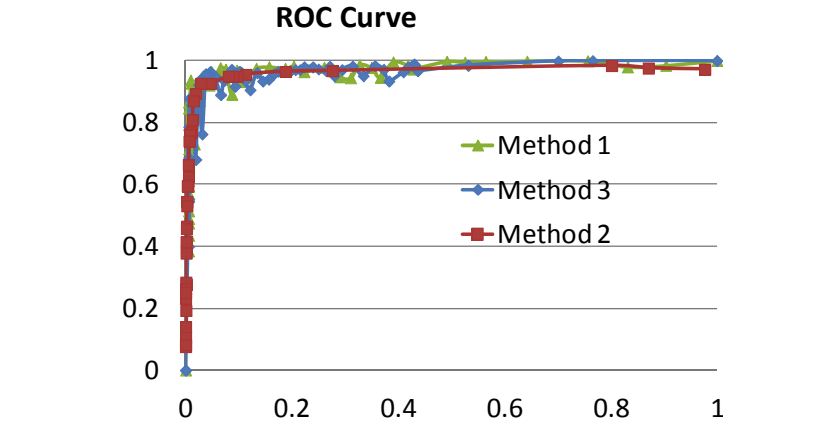

(a)

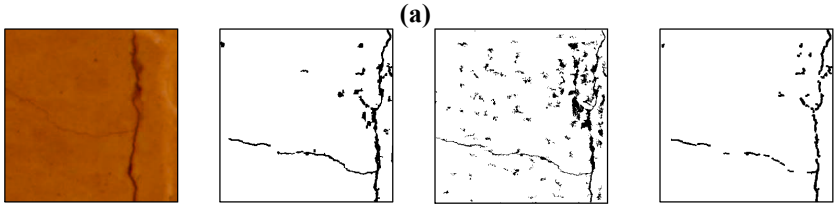

Orig. Image 36 Method 1 f=0.979 Method 2 f=0.941 Method 3 f=0.973

(b)

Fig.5.13 Comparison of the ROC curve for Orig. image36.

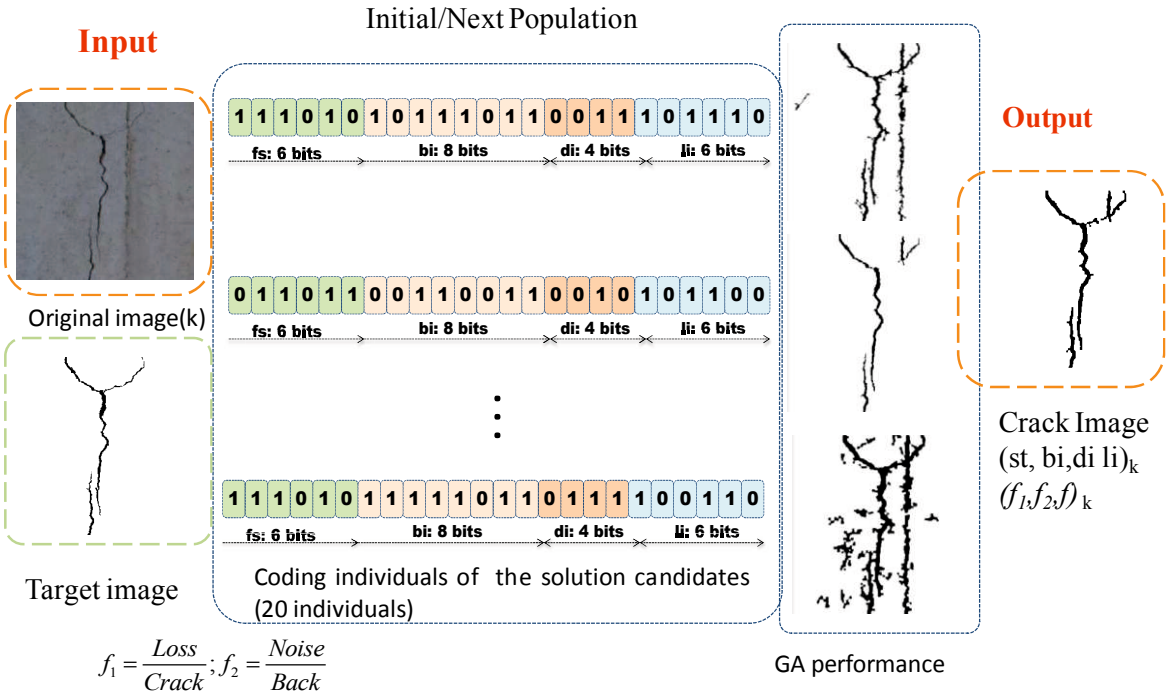

Fig.5.14 Optimum parameter adjustment for training data.

5.3.5 A chosen specific parameter set for full automatic crack detection

To guarantee automatic crack detection for any unknown images of concrete structure surface, Image data set is diverse with thin crack images in complex dark environmental. For this study a total of 50 infrastructure surface images consist of 30 thin crack images and 20 thicker crack images with noises, shading, and artifacts. These samples are selected randomly from a huge number of concrete civil infrastructure images to make sure that the image data can represent the general characteristics of cracks in various conditions for servicing automatic inspection. The testing data composes of 30 different various noise images to check the accuracy of the chosen parameter set.

Fig.5.14 show the k^{th} represented image in the training data that is adjusted to optimum parameter $(st, bi, di, li)^k$ with respect to the accuracy $(f)^k$. This parameter is found from 2000 results included 20 individuals with 100 generations based on the genetic algorithm and the objective function. This function evaluates the accuracy of individual compared to the target image.

The training data consist of 50 different images having 50 different optimum parameters. Therefore, the training progress is iterated by using each abovementioned

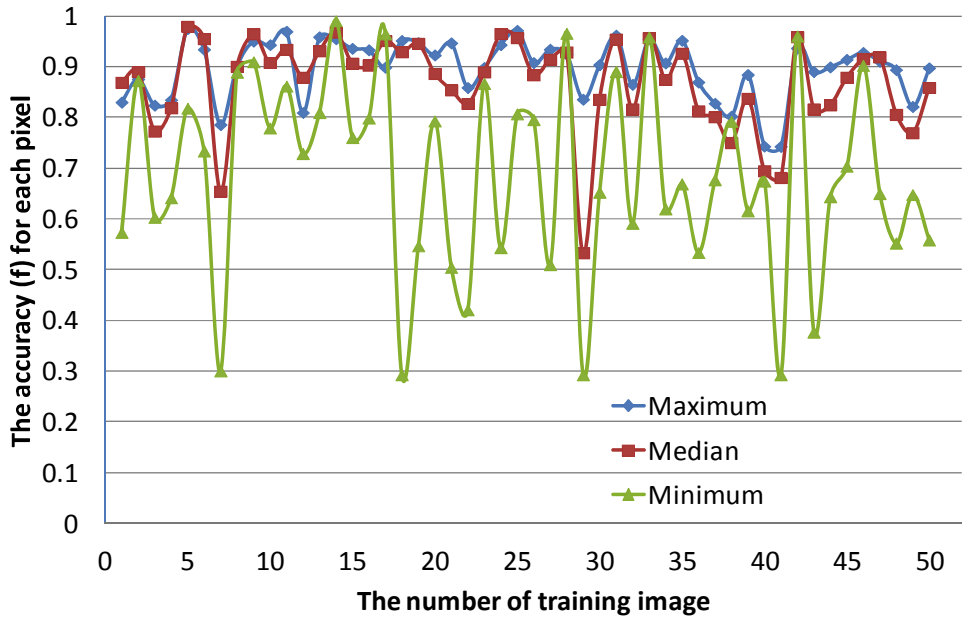

Fig.5.15 The results of the training test using the specific parameter.

optimum parameter for 50 images so that get their average accuracy as the following equation:

$$f_{(i,j)\,1\le i\le n \atop 1\le j\le m} = \begin{pmatrix} f_{11} & \cdots & f_{1n} \\ \vdots & \ddots & \vdots \\ f_{m1} & \cdots & f_{mn} \end{pmatrix}; f_j = \begin{bmatrix} \overline{f_1} \\ \vdots \\ \overline{f_m} \end{bmatrix} \tag{5.10}$$

$$[\text{st,bi,li,di}]^* = \arg\max(f_j)$$

Where, f(i,j) is the accuracy of the crack detection of the i^{th} image using the j^{th} parameter.

f_j: the average accuracy of training data using the j^{th} parameter.

n: the number of training results of the j^{th} parameter

m: the total number of the parameters are conducted. In this case, m=n= 50.

[st, bi, di, li]* : is a chosen parameter to detect crack pixels for the testing data.

As a result, **Fig.5.15** indicates the results of the training test using the specific parameter for three represented cases with respect to maximum, median and minimum lines of the average accuracies.

As can be seen, the blue line (maximum) obtains the most stability faced with the different 50 images under various complex environmental conditions. The median line have a little fluctuation. Consequently, the minimum line receives the most fluctuations.

Table.5.4 Accuracy evaluation of proposed method.

Items	Training	Testing
Average accuracy (for a pixel level)	91.24%	89.7%

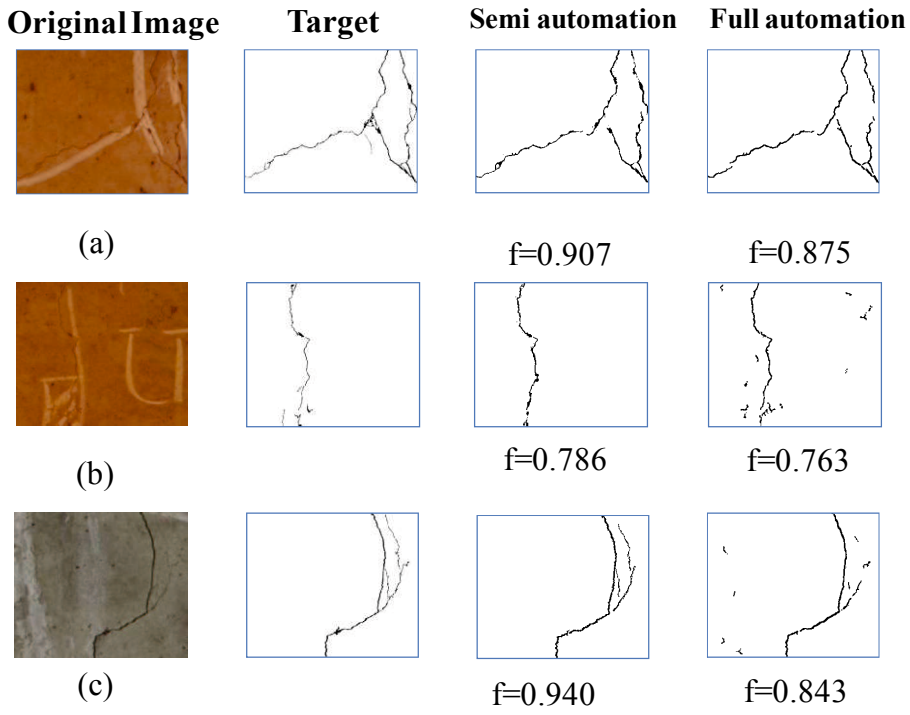

Fig.5.16 Comparison of the accuracy between Semi-automation and full automation.

5.3.6 Comparison of performance between semi-automated method and fully automated method

Corresponding to the maximum line, the optimum parameter is: st=9, bi=94, di=5 and li=19.5 achieving the maximum accuracy of f=0.912. The **Table.5.4** presents the accuracy of training, and testing progress. The result demonstrates that the parameter set is able to use to automated crack detection for a thousand of tunnel lining surface images. **Fig.5.16** presents the performance of the two approaches. The accuracy of the semi-automatic methods outperform than the one of the full automatic method. This is because the semi-automatic method adjusts the parameter for each image. In order word, the different optimum parameter adapts to the different actual concrete surface meanwhile the fully automatic method only use a specific parameter for all of sample tests.

Table.5.5 Comparison of working time between Semi-automation and full automation.

Working time	Semi-Automation (Minutes)	Full-Automation (Minutes)
Adjust parameter	30[1)]	1[2)]
Noise Removal	0.5	

1): Average working time of 3 users adjust the optimum parameter using iGA estimated 1 minute for each image.
2): Working time creates 30 crack images using a parameter set in the one time of program implement.

5.3.7 Performance comparison for working time

Table.5.5 shows the comparison of working time between semi-automated method and fully automated methods. The fully automated approach yields image processing time to be reduced significantly with 1 minute for 30 images. Meanwhile, the semi-automatic method gets the longer processing time with 30.5 minutes for 30 images.

It is concluded that the fully automated method would be applied to the inspecting regions which detect cracks/defects easily to save processing time. Otherwise, the inspecting regions in which the fully automatic method is difficult to detect crack/defects is that the semi-automated method would be applied.

5.4 Experiment of maximum crack width determination

The maximum crack width reflects the concrete structures of deteriorated status. Therefore, it is as an important index to assess the concrete structure condition. The following equation is applied to check the maximum crack width.

$$\begin{aligned} d_i &= \sqrt{(\mathrm{x}_1 - x_2)^2 + (y_1 - y_2)^2} \\ D_j &= \min\{d_i\} \\ W_{\max} &= \max\{\mathrm{D}_j)\} \end{aligned} \tag{5.11}$$

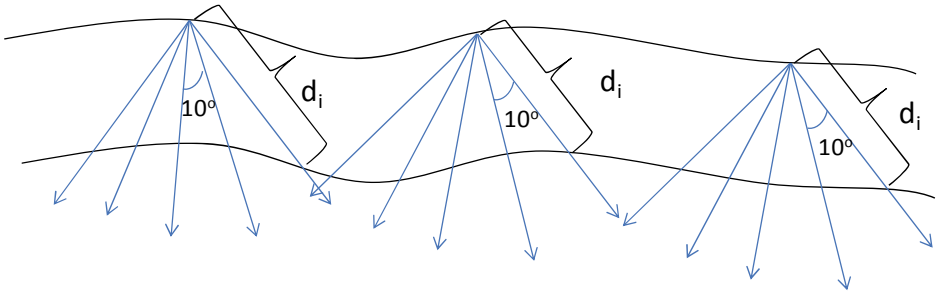

Fig.5.17 Scheme of Euclidean distance measurement.

Table.5.6 The results of the crack width measurement and calculation.

Image	Resolution (mm/pixel)	Measurement (mm)	Calculation (mm)	Deviation (mm)
A	0.06	0.4	0.36	0.04
B	0.06	0.35	0.36	0.01
C	0.06	0.4	0.36	0.04
D	0.06	0.3	0.25	0.05

(x_1,y_1) is one side coordinates, and (x_2,y_2) is the other side coordinates of the edge of the crack line. d_i is an Euclide distance of the i^{th} vector. *Dj*: the minimum distance between two sides (crack width) at the j^{th} position. From a arbitrary point of this side, a profile of vectors is created to the other side with rotation angle of 10^o from 0^o to 90^o shown in **Fig.5.17**.

Test samples use the above **Fig.4.13** to make experiment. The results are presented in the **Table.5.6**. As shown in the results of the deviation, the calculation of the crack width has the high accuracy with maximum deviation ± 0.05 mm smaller than one pixel because the resolution is 0.06 mm/pixel.

5.5 CONCLUSIONS

The experimental results of various low-contrast surface images of concrete infrastructures under complex brightness conditions demonstrated that the effectiveness

of the proposed method. However, the crack width results of the method 1 were larger than the ones of the target image. This reason was that the proposed method 1 prioritized to detect the thin cracks without losing the crack pixels. This method preferred to remove noises surrounding the crack line significantly.

Comparison between Semi-automated crack detection and full automated crack detection, each method has the own advantage.

The semi-automatic method is better performance for the difficult cases detected cracks and large-size. The fully automated method appropriates the easier cases detected cracks. The fully automated method is applied when user prefers the working time and no requirement of the high accuracy. In contrast, the semi-automated method provides the higher accuracy of the crack detection when user adjusts the parameters for each image without training data as well as the objective function.

CHAPTER 6

CONCLUSIONS

6.1 SUMMARY

Inspection plays an important role in the maintenance of infrastructure. It is an integral part of structural heath monitoring systems, designed to assess the condition of structural components and determine whether or not they are need of preparation. One of the most frequently adopted inspection techniques is visual inspection, which is carried out by inspectors. It has a number of limitations, such as the high labour costs associated with carrying out tasks, and inaccuracy due to subjectivity. A significant number of research has been carried out to develop automated inspection systems to improve on manual visual inspection. In the field of civil engineering, a number of inspection systems have been developed to utilise inexpensive technologies based on digital videos and cameras.

Examples of these systems include a calibrated image tool before mosaicking and a semi-automatic crack detection method[53]. The imaging systems allow the fast acquisition of video data[14),23)]. Technologies in image processing and pattern recognition have been applied to detect, localise and quantify damage in monitored structural components from video or image data. However, none of these systems offer complete solutions and a significant amount of work is still required to create an automated inspection system that can be adopted by the industry. The advancement of computer science and image processing techniques offers the possibility of creating an automated system for inspection. This thesis describes a system, which is based on state-of-the-art image analysis, to aid the visual inspection of tunnels. The system uses multi standard digital cameras, which is cheap compared with the other technologies,

such as MIMM-R or infrared cameras. The purpose of the system is to detect the defects on the tunnel lining surface based on two following themes.

For layout panorama generation, this research proposes an image acquisition device with a simple and effective structure that obtains sufficient image data for objective and precise quantification. Furthermore, image stitching software was developed to create large layout panorama from the tunnel lining surface images, making it easier to visualize a large and detailed section of the tunnel lining. However, a traditional inspection report is usually collection of individual images which is not easy to visualize and doesn't create a sense of where the images are captured. Moreover, this study proposed two approaches: Semi-automated method and fully automated method.

Semi-automated crack detection in principle, a fully automated crack detection method for all of inspecting regions would be desirable. In fact, it is difficult to achieve this goal with high accuracy because of irregularity of cracks and various complex conditions of noise concrete images. Therefore, this research provides a semi-automatic crack detection software to assist user how to fast detect the cracks of each large-size concrete surface image with reasonable accuracy.

An automatic crack detection method: for fully automatic crack detection, a specific parameter set of the image processing technique is chosen based on genetic algorithm and trade-off between lose and noise ratio to extract crack pixels for a thousand of images in the regions of easily detect crack detection.

Based on the above themes, this thesis makes specific contributions as follows:
The first contribution of the inspection system in this research is to create the extended panoramic images in both longitudinal and circumferential directions so as to assist inspectors who have a wider field of view or an enhanced visualisation of large area the tunnel lining. To achieve this, a mosaicing technique consisted of image matching and stitching methods is proposed. In that, image matching method is detail presented in similarity metric such as sum of square difference (*SSD*), sum of absolute difference (*SAD*), normalized-cross correlation (*NCC*), zero mean normalized-cross correlation (*ZNCC*), curvature metrics (*CUR*), and mean curvature at the nearest neighbour pixels as well as the pixel being processed (*CNP*) to find correct matching points. Moreover, in the curvature metric, median filter is used for refinement to smooth image motion quantity (*IMQ*) in the consecutive image stitching process. Accordingly, an image

stitching software is developed based on the proposed algorithm to create a layout panorama of the tunnel lining surface for assisting defect inspection. Moreover, experimental results for an actual tunnel demonstrate that the curvature measurement can match consecutive images accurately.

The second contribution of the inspection system is to propose the prototype software based on an image processing technique (IPT) and an interactive genetic algorithm (iGA) with a touch screen that helps inspector easily to detect the cracks (defects) from various concrete surface images.

The algorithm for the accurate crack detection has composed of three major process parts. The first part was image input part which included image input and gray-scale image transformation. The second part was crack enhancement part which included the following pre-processing steps: median filter, subtraction, binarization. The final part was noise removal part, comprising two steps: labeling and linear degree determination. In that, the optimized parameter problem is adjusted by iGA. Namely, the size of median filter is expressed by 6 bits, the binarization is expressed by 8 bits and the linear degree is expressed by 6 bits. Three parameters are combined to create a represented chromosome for solution candidate in a population.

Furthermore, to improve the capacity of the thin crack detection in the various complex environmental conditions, an image processing technique based on mathematic morphology is also proposed, which consists of morphological filter, binarization, dilation-thinning transformation, and linear degree. The optimum parameters of IPT are also adjusted by genetic algorithm.

The crack detection results of the proposed method are compared to the ones of other methods to demonstrate that the proposed method has possibility of extracting crack with reasonable accuracy and working time.

6.2 CONTRIBUTION OF THE RESEARCH

In this study, the useful imaging system proposed that was capable of scanning pictures of the entire tunnel through six passes (forward three times, backward three times). The total of six cameras, which each camera concluded 1558 images with

1290x1080 pixels resolutions, were taken by each moving of the inspection car saved much time than other conventional imaging systems. It collects full enough tunnel lining surface without constraint traffic to create an enlarged long panorama of tunnel lining.

The proposed image matching method in this study implements similarity metrics and error correction techniques for all points of the images in the experiment, which eliminates errors in the image stitching process. Moreover, the research contributed a novel metric that the curvature of the cost curve at the nearest neighbour pixels as well as the pixels being processed was used to find appropriate matching points for creating the layout panoramas of the tunnel lining surface image for the main purpose improved traditional similarity metrics. Moreover, the *CNP* metric yielded the effectiveness of image matching process which not depending on the parameters of the image acquisition system as well as without pre-processing for the big input image data. Consequently, application of median filter rectified the error of inappropriate *IMQ*. The parameters of the imaging system were used to estimate the error rate of the initialized image matching.

The image stitching software enabled to parallel running implementation to six cameras reduced computational time significantly. The test results showed the high performance of the *CNP*(*SAD*) metric when compared to *MSM*, *CUR* metrics. In addition, comparing with the image matching results of two our previous methods, the ones of the proposed method outperformed significantly. Further, the ground-truth panorama was implemented for 120 images to check validation of the *CNP* metric. As a result, the *CNP* metric was the reliable image matching metric for producing the layout panorama of the un-calibrated image data.

The experimental results, which consist of a large, high-resolution, high-accuracy image of the entire tunnel lining is shown in **Fig.3.21**. This image makes it easy to detect defects on the tunnel wall surface. Namely, the defect shown in **Fig.3.21** is chalk-line. This result will enable tunnel wall inspection to become more objective, accurate, and faster than the conventional inspection methods.

Consequently, in this research, the semi-automated crack detection software is proposed in chapter 4, with the two evaluation criteria about the accuracy and time of crack extraction, the experiment results indicated that the proposed method has achieved

reasonable accuracy and working time. Furthermore, in this experiment, the average working time for the extracting crack of each image reduced about 87%. If the crack extraction is performed by the proposed software for a thousand of images, it will save a great deal of time.

This study proposed a robust method for crack semi-automatic detection from concrete surface images. The prototype software is developed based on iGA with the image processing technique. Especially, using a touch monitor, the easiness and efficiency of the proposed crack detection software is remarkable.

Moreover, the proposed method, the iGA for image processing parameter optimization, is compared to the Haar wavelet transform method with GA. As a consequence, the final result image demonstrated that the proposed method has the possibility of extracting crack with reasonable accuracy. However, two sample images are limited, so it is not able to conclude a better method approach.

A fully automatic crack detection was proposed in chapter 5. Therein, a training data is selected from a huge number of civil infrastructures. The training data included 50 noise images with various complex environmental conditions represented to adjust the optimum parameters. The crack detection algorithm based on mathematic morphological processing and genetic algorithm. A specific parameter set is chosen based on the trade-off of the noise and loss ratio to detect cracks automatically for the input images. The accuracy of crack detection for training, validation and testing data was evaluated by comparing with ground-truth data in pixel unit.

6.3 DISCUSSION

Besides, the limitation of this research only proposed intensity based metrics in the predefined search area which not be compared to feature descriptors based image matching methods (SIFT, SURF). The software hadn’t implemented camera stitching via the circumferential direction of the tunnel full automatically yet. Moreover, the speed of inspection car should increase to guarantee convenient traffic flow. These problems would be solved in the future works.

In the semi-automatic crack detection, the loss pixels still remain with a high rate, this software needs to will be improved further in the future. Furthermore, the size of the extracted cracks (width, length, orientation) also would be measured automatically from this proposed software. In the full automatic crack detection method can be improved by using deep learning method in the machine learning. It is necessary to increase a number of images in the training data.

Chapter 4 and 5 applied image processing technique and iGA (GA) to semi-automatic and fully automatic crack detection methods, respectively. The semi-automatic method provided the inspectors a simple and fast way to extract crack lines intuitively on the touch screen without knowledge of image processing techniques.

Further, the semi-automatic method yielded the higher accuracy than the other. Therefore, it can be used to make the target images for shortening time compared with the manual method.

However, comparing with the fully automatic method, the semi-automatic method is so time-consuming due to crack detection for each image. It is impossible to adjust parameters for a huge number of images acquired from the huge and large civil infrastructure. Therefore it is necessary to detect crack detection automatically.

The fully-automatic crack detection method needs training data (target images) and objective function to adjust and choose an optimum parameter. This parameter is applied to extract crack pixels for the various images.

A semi-automatic crack detection method is applied to inspecting regions which are not able to detect the crack pixels automatically. Otherwise, A fully automatic crack detection method is used for the inspecting regions where crack pixels are easily detected by IPTs and genetic algorithm.

6.4 FUTURE RESEARCHES

This study detected the abnormalities of tunnel lining surface no inspecting the shape of the tunnel. Therefore, the obtained images of the curved shape of tunnel lining are unfolded to create the flat panorama for aided visual inspection. The shaped 3D reconstruction of the tunnel-lining surface would be in the future research.

The study observes several limitations. The proposed image-matching method relies exclusively on the color-pixel intensity. There lack of feature descriptors based methods such as SIFT and SURF. Moreover, the speed of the inspection car should be increased to eliminate effect on traffic flow. These limitations will be addressed in future work.

Moreover, the proposed method of fully automated crack detection would be compared with the object detection approach based on neural network convolution. This problem would be implemented in the future research.

ACKNOWLEDGEMENTS

First of all, I would like to express my deepest gratitude to my advisor, Associate. Professor Kei KAWAMURA. His constant support, continuous encouragement, and exemplariness help me follow during the research period. Without him, I would not have the chance to work and complete this research. I cannot thank him enough.

I would like to thank our laboratory members which support and give me some useful comments through the weekly meeting. I would like to sincerely thank Vietnam International Education Development (VIED), Ministry of Education and Training for its financial support through the program 911. And I wish to thank Mien Trung University of civil engineering, my office, for supporting time and working and Yamaguchi University in the MOU signed with VIED for supporting the tuition fee during three years.

My mission in Japan not only study doctoral course but also have some practical experiences to enjoy foods, Japanese language, culture, environment and person to person relationship through associations for international student (Kazenokai Yamaguchi, Ube city, Tokiwa Kogyo). I have actually admired this country. I express to thank my Mom and Dad, I always miss them whom nobody takes care in my hometown. I also thank my small family including my wife, Dao Thi Hien, and my sons, Nguyen Vy Tung, Nguyen Vy Truong who always live beside me peacefully and lovely.

I also not forget to thank some international and Vietnam friends who give me many discussions about life as well as work in Japan in the relaxing time.

NGUYEN KIM CUONG

REFERENCES

1) Stajano, F., Hoult, N., Wassell, I., Bennett, P., Middleton, C., and Soga, K. : Smart bridges, smart tunnels: Transforming wireless sensor networks from research prototypes into robust engineering infrastructure, *Ad Hoc Networks*, Vol.8, pp.872–888, 2010.
2) Asakura,T. and Kojima,Y. : Tunnel maintenance in Japan, *Tunnelling and Underground Space Technology*, Vol.18, pp.161–169, 2003.
3) Chaiyasarn. K. : Damage detection and monitoring for tunnel inspection based on computer vision, Christ's College, *University of Cambridge*, UK, Dissertation, 2011.
4) Burgess and Niple. : Creates custom device for florida cable-stay inspecion, *Columbus*, Ohio, 2015.
5) Elliott, M. E., and Heymsfield, E. : Inspection of luling bridge cable stays : case study, *Journal of construction engineering and management*, Vol.129, pp.226–230, 2003.
6) Pacific Consultants :<https://www.pacific.co.jp/service/infrastructure/tunnel/close-up/mimm-r/>, (accessed 2017.9.15).
7) Park, S. : A guideline on condition assessment of existing old railway tunnels, *Tunnel Underground Space Technol*, Vol.21, No.3, pp.329–330, 2006.
8) Blitz, J., Simpson, G. : Ultrasonic methods of non-destructive testing, *Springer*, 1996.
9) Wimsatt, A., Scullion, T., Hurlebaus, S., Zollinger, D. : High-speed non-destructive testing methods for mapping voids, debonding, delaminations, moisture, and other defects behind or within tunnel linings, *IBTTA facilities management and maintenance workshop*, Nashville, Tennessee.
10) Kocha, C., Georgieva, K. , Kasireddy, V., Akinci, B., Fieguth, P. : A review on computer vision based defect detection and condition assessment of concrete and asphalt civil infrastructure, *Advanced Engineering Informatics,* Vol.29, pp.196–210, 2015 .

11) Miyamoto, A., Konno, M., Bruhwiler, E. : Automatic crack recognition system for concrete structures using image processing approach, *Asian J. Inf. Technol*, Vol.6, No.5, pp.553–561, 2007.

12) Fujita, Y., Mitani, Y. and Hamamoto, Y. : A method for crack detection on a concrete structure, in: *Proceeding of 18th International Conference on Pattern Recognition*, pp. 901–904, 2006.

13) Abdel-Qader, I., Abudayyeh, O. and Kelly, E.-M. : Analysis of edge-detection techniques for crack identification in bridges, *Journal of Computing in Civil Engineeringg in Civil Engineering*, Vol 17, pp 255-263, 2003.

14) Ukai, M. : Development of image processing technique for detection of tunnel wall deformation using continuously scanned image, *Quart. Rep. – RTRI*, Vol.41, No.3, pp.120–126, 2000.

15) Yamaguchi,T. : A study on image processing method for crack inspection of real concrete surfaces, *Waseda Univeristy*, Japan, Doctoral Dissertation, 2008.

16) Paar, G., Kontrus, H., and Sidla, O. : Optical crack following on tunnel surfaces, *Proceedings of the SPIE International Society for Optical Engineering,*Vol.6382, 2006.

17) Zhu, Z., German, S., and Brilakis, I. : Detection of large-scale concrete columns for automated bridge inspection, *Automation in Construction*, Vol.19, No.8, pp.1047–1055, 2010.

18) Liu, Z., Azmin, S., Ohashi, T., and Ejima, T. : A tunnel crack detection and classification systems based on image processing, *Society of Photo-Optical Instrumentation Engineers (SPIE) Conference Series*, Vol. 4664, pp.145–152 , 2002.

19) Abdelqader, I., Pashaierad, S., Abudayyeh, O., and Yehia, S. : PCA-based algorithm for unsupervised bridge crack detection, *Advances in Engineering Software*, Vol.37, No.12, pp.771–778, 2006.

20) Zhang, W., Zhang, Z., Qi, D. and Liu, Y. : Automatic crack detection and classification method for subway tunnel safety monitoring, *Sensors*, Vol.14, No.10, pp.19307-19328,2014.

21) Shen, B., Zhang, W., Y., Qi, D. P. and Wu, X. Y. : Wireless multimedia, network based subway tunnel crack detection method , *Sensor*, Vol.15, 2015.

22) Ukai, M. and Nagamine, N. : A high-performance inspection system of tunnel wall deformation using continuous scan image, *9th World Congress Railway Research*, 2011.

23) Yu, S., Jang, J., and Han, C., : Auto inspection system using a mobile robot for detecting concrete cracks in a tunnel, *Automation in Construction*, Vol.16, No.3, pp.255–261, 2007.

24) Egnala, G., Mintza, M., Wildesb, R. P. : A stereo confidence metric using single view imagery with comparison to five alternative approaches, *Image and Vision Computing*, Vol. 22 , pp.943–957, 2004.

25) Gavilán, M., Sánchez, F., Ramos, J. A. and Marcos., O. : Mobile inspection system for high-resolution assessment of tunnels, *The 6th International Conference on Structural Health Monitoring of Intelligent Infrastructure Hong Kong*, 2013.

26) Stentoumis, C., Loupos, K., Doulamis, A. and Amditis, A. : A computer vision system for tunnel inspection, *ITA WTC 2015 Congress and 41st General Assembly*, 2015.

27) Zhan, D., Yu, L., Xiao, J. and Chen, T. : Multi-camera and structured-light vision system (MSVS) for dynamic high-accuracy 3d measurements of railway tunnels, *Sensors*, Vol.15, No.4, pp.8664-8684, 2015.

28) Jahanshahi, M., Masri, S. and Sukhatme, G. : Multi-image stitching and scene reconstruction for evaluating defect evolution in structures, *Structural Health Monitoring*, Vol.10, No.6, pp.643-657, 2011.

29) Zhu, Z. H., Fu, J. Y., Yang, S. J. and Zhang, X. M. : Panoramic image stitching for arbitrarily shaped tunnel lining inspection, *Journal of Computer-Aided Civil and Infrastructure Engineering*, Vol. 31, pp. 936-953, 2016.

30) Sagong, M. And Koh, T. H., Chun, B. S., Lee, B. H., and Byun, Y. S. : Application of the image and laser sensors based tunnel scanning system, *Geotechnical Aspects of Underground Construction in Soft Ground,* pp. 105-109, 2012.

31) Byrne, J., Laefer, F., D.: Maximum feature detection in aerial unmanned aerial vehicle datasets, *Journal of Applied Remote Sensing*, Vol.11, No.2, 2017.

32) Kawamura, K., Koga, M., Matsumoto, J., Shiozaki, M., and Sawamura, S. : A study on panoramic images generation of tunnel wall, *Japan Society of Civil Engineers*, Vol.71, No.2, pp.142-151, 2015.

33) Kawamura, K., Yoshizaki, M., Koga, M., Matsumoto, J., Shiozaki, M., and Sawamura, S. : Tunnel wall panoramic images generation using a local search algorithm, *Japan Society of Civil Engineers*, Vol.72, No.2, pp.73-82, 2016.

34) Bank, J., and Corke., P., : Quantitative evaluation of matching methods and validity measures for stereo vision, *The International Journal of Robotics Research*, Vol.20, No.7, pp.512-532, 2001.

35) Kumar, S., and Chatterji, N. : Two-frame stereo matching algorithm- a review, *IETE Journal of Research*, Vol 50, No. I, pp.49-61, 2004.

36) Lee, H. W., Kim, Y., and Ra, B. J. : Efficient stereo matching based on a new confidence metric, *20th European Signal Processing Conference EUSIPCO*, pp.1139-1143, 2012.

37) Ba, H., Yata, N. and Nagao, T. : Automatic finding of optimal image processing for extracting concrete image cracks using features ACTIT, *IEEJ Transactions On Electrical And Electronic Engineering*, Vol. 7, No.3, pp.308–315, 2012.

38) Nishikawa, T., Yoshida, J., Sugiyama, T. and Fujino., Y. : Concrete crack detection by multiple sequential image filtering, *computer-Aided civil and infrastructure engineering*, Vol.27, No.1, pp 29-47, 2012.

39) Guo, W., Soibelman, L., and Garrett, J. Automated defect detection for sewer pipeline inspection and condition assessment, *Automatic Construction*., Vol.18, No.5, pp. 587–596, 2009.

40) Kawamura, K. ., Yoshino, K., Tarighat, A. and Nakamura., H. : A valid parameter range identification method of a digital image processing algorithm for concrete surface cracks detection using genetic Algorithm and decision tree, *JSCE*, Vol.69, No2 p.13-23, 2013.

41) Kawamura, K., Miyamoto, A. , Nakamura, H. and Sato., R. : Proposal of a crack pattern extraction method from digital images using an interactive genetic algorithm *Proc. Japan Soc. Civ. Eng*, Vol.742, pp. 115-131, 2003.

42) Farooq, H., Siddique, M. T. : A comparative study on user interfaces of interactive genetic algorithm, *procedia computer Science*, Vol.32, pp.45-52, 2014.

43) Mukhopadhyay. S, Mandal. J K. : Wavelet-based denoising of medical images using subband adaptive thresholding through genetic algorithm, Vol.10, pp.680-689, 2013.

44) Ito, A., Aoki, Y., and Hashimoto, S. : Accurate extraction and measurement of fine cracks fiom concrete block surface image, *IECON 02 Industrial Electronics Society, IEEE 2002 28th Annual Conference of the IEEE*, Vol.3, pp.2202–2207, 2002.

45) Zhu, Z., German, S., and Brilakis, I. : Visual retrieval of concrete crack properties for automated post-earthquake structural safety evaluation, *Automation in Construction*, Vol.20, No.7, pp.874–883, 2011.

46) Nguyen, C., Kawamura, K., Tarighat, A., Matsumoto, J., and Shiozaki, M. : Development of semi-automated crack detection software for concrete structures, 11th fib International PhD Symposium in Civil Engineering, 2016.

47) Nishikawa, T., Yoshida, J., Sugiyama, T., Fujino, Y. : Concrete crack detection by multiple sequential image filtering, *computer-Aided civil and infrastructure engineering* , Vol.27, pp.29-47, 2012.

48) Shinha, K.-S. and Fieguth, P.-W. : Automated detection of cracks in buried concrete pipe images, *Automation in Construction*, Vol.15, pp.58-72, 2006.

49) Jahanshahi, M. R., Masri,S. F. : Adaptive vision-based crack detection using 3D scene reconstruction for condition assessment of structures, *Automation in Construction*, Vol.22, pp.567-576, 2012.

50) Lam, L., Seong, W. L, and Ching Y. S. : Thinning Methodologies-A Comprehensive Survey, *IEEE Transactions on Pattern Analysis and Machine Intelligence*, Vol 14, No. 9, pp.869-885, 1992.

51) Zhao, L., and Niu, L., Study on Key Technique of Image Processing and Automatic Recognition of Tunnel Cracks, *ICLEM*, pp.427-433, 2012.

52) Otsu, N. : A threshold selection method from gray-level histograms, *IEEE Trans Syst Man Cybern*, Vol.9, pp.62-66, 1979.

53) Fujita, Y., Taguchi, T., Hamamoto, Y. : Image mosaicking and semi-automatic crack evaluation for visual inspection of concrete structures, *Japan Society of Civil Engineers*, Vol.74, No.1, pp.18-32, 2018.

LIST OF AWARD, PUBLICATIONS AND SCIENCE CONFERENCES

1. AWARD

Outstanding Paper Award of 2017 (Journal of Japan Society of Civil Engineers, Ser. F3 (Civil Engineering Informatics 2018)). (The best paper of 58 papers)

Title: Study of Panoramic Images Generation for Tunnel Lining Inspection Using The Gradient of Intensity Difference Distribution Between Two Images
Authors: Kei KAWAMURA, Masatoshi YOSHIZAKI , Cuong Nguyen KIM, Masando SHIOZAKI and Hideaki NAKAMURA.

2. A PART OF THE THESIS HAS BEEN PRESENTED AT SCIENCE CONFERENCES

a, Cuong Nguyen Kim, Kei Kawamura, Amir Tarighat, Junji Matsumoto, and Masando Shiozaki. Development of Semi-Automatic Crack Detection Software for Concrete Structures. Proceedings of The 11th *fib* International PhD Symposium in Civil Engineering , Tokyo, Japan. pp. 459-466, 2016.

b, Cuong Nguyen Kim, Kei Kawamura, Amir Tarighat, and Masando Shiozaki. Development Of An Automatic Crack Inspection System For Concrete Tunnel Lining Based on Computer Vision Technologies. IOP Conf. Series: Materials Science and Engineering. Vol.371 (2018) 012015. 2018.

3. A PART OF THE THESIS HAS BEEN PRESENTED AT PUBLICATIONS

a, Cuong Nguyen Kim, Kei Kawamura, Amir Tarighat. A Study on Semi-Automatic Concrete Cracks Detection Using Interactive Genetic Algorithm. Proceedings of the Japan Concrete Institute. Vol. 38, No. 1, pp. 2061-2066. 2016.

b, Kei Kawamura, Masatoshi Yoshizaki, Cuong Nguyen Kim, Masando Shiozaki, Hideaki Nakamura. Study of Panoramic Images Generation for Tunnel Lining Inspection Using The Gradient Of Intensity Difference Distribution Between Two Images (in Japanese). Japan Society of Civil Engineers. F3,Vol 73, No. 2, pp.188-200. 2018.

c, Cuong nguyen kim, Kei kawamura, Amir tarighat, Hideaki nakamura. A Crack Detection Method for Concrete Infrastructures Based on Image Processing Technique And Genetic Algorithm. Proceedings of the Japan Concrete Institute. Vol. 40, No. 1, pp. 1785-1790. 2018.

d, Cuong Nguyen Kim, Kei Kawamura, Masando SHIOZAKI , Amir Tarighat. A Image Matching Method Based On The Curvature Of Cost Curve For Producing Tunnel Lining Panorama. Japan Society of Civil Engineers (accepted notification). 2018.